Passive Scalar Intermittency In Random Flows

by
Zhi Lin

A dissertation submitted to the faculty of the University of North Carolina at Chapel Hill in partial fulfillment of the requirements for the degree of Doctor of Philosophy in the Department of Mathematics.

Chapel Hill
2007

Approved by:

Richard M. McLaughlin, Advisor

Roberto Camassa, Co-Advisor

Jingfang Huang, Committee Member

Peter Mucha, Committee Member

Alberto Scotti, Committee Member

Abstract

ZHI LIN: Passive Scalar Intermittency In Random Flows.
(Under the direction of Richard M. McLaughlin and Roberto Camassa.)

This thesis concentrates on reconstructing the complete probability density function (PDF) for a passive scalar governed by a random advection-diffusion equation using a variety of mathematical tools, primarily from partial differential equations, perturbation theory, numerical analysis and statistics. First we present a one-dimensional model which is essentially a random translation of pure heat equation. For some deterministic initial data, the ensuing scalar PDF and its statistical moments can be explicitly calculated. We use this model as a testbed for validating a numerical reconstruction procedure for the PDF via orthogonal polynomial expansion. In this model, the Péclet number is shown to be decisive in establishing the transition in the singularity structure of the PDF which affects the effectiveness of the series expansion, from only one algebraic singularity at unit scalar values (small Péclet), to two algebraic singularities at both unit and zero scalar values (large Péclet). Next, we study the more complicated, two-dimensional model in which the underlying flow is a random linear shear in one dimension. For planar, Gaussian random initial data, we identify the scalar PDF as an integral representing a conditional mixing of Gaussian probability measures averaged over all realizations of a single random variable, namely, the renormalized L^2-norm of standard Wiener process. Rigorous asymptotic analyses and solid numerical simulation are performed to the integral formulation to study the evolution and the parametric dependence of the scalar PDF. During these analyses, we discover a transient, non-monotonic "breathing" phenomena that is related to the multiple spatial scales in the initial random field. Lastly, some preliminary analytical and numerical results are presented to explore the potential of applying the reconstruction methodology to more general, physically relevent models, such as a rotating, viscous, wind-driven shallow water equation.

Acknowledgments

I think that it is much harder, if not impossible, for me to thank all the people that have helped me here in the United States enough, than to complete this thesis. And I cannot fully describe how many things have changed me, in a positive way, ever since I came here five years ago. For me, it is such a honor and privilege to study and work in this wonderful place, with these wonderful people, during all this time that maybe passed too quickly.

I would also like to express my gratitude to the National Science Foundation for their kind financial support through the grant "Collaborations in Mathematical Geosciences" (ATM-0327906) over the last three years.

I sincerely thank ALL the students and PhD students that I met during my stay here, whether we had heated discussions about mathematics, or they were filled with passion when it came to sharing personal interests.

I would like to bring my warm thanks to all the former and present postdoctoral scholars whom I have worked with: Chung, Hayder, Long, Neil, not only for their help in mathematics, but also for their valuable advice on my personal life and career.

I would like to thank our very efficient and helpful secretaries, for being experts all along in alleviating the cultural differences with which international students usually have a hard time. I am especially grateful to Brenda, Elaine and Janet, for their extraordinary, consistent patience with my repetitious being locked out of my office.

For their utmost care, love and support, I am grateful to my parents and my girlfriend Ke.

Table of Contents

List of Figures

Chapter 1

Introduction

Often referred to as "the last unsolved problem of classical physics", turbulence is the highly unpredictable, irregular motion that is ubiquitously observed in various fluids in Nature. The modern efforts on attacking this mystery were started by Reynolds with his experiments in 1883, in which he proposed a stability criterion for the transition from laminar to turbulent flows based on the non-dimensional Reynolds number (Reynolds, 1883). Over the last century, the mainstream academic community has come to agree that for turbulent flows, the formidable number of degrees of freedom, and sensitivity to the initial and boundary conditions, warrant a statistical rather than a chaotic yet deterministic characterization. As the culmination of the early stage of turbulence research, Kolmogorov advanced the notions of "energy cascade" and self-similarity in his seminal paper (Kolmogorov, 1941), which served as the first statistical theory of turbulence. Mathematically elegant as they are, Kolmogorov's original scaling hypotheses and predictions have been shown to break down within the inertial range by recent analyses, experiments and simulations, and numerous efforts have been made to amend and improve those fundamental ideas (Falkovich and Sreenivasan, 2006). Thus, a complete description of turbulence remains a conundrum in science.

This thesis is devoted to an important subject in the study of turbulence: the study of *passive scalars*. A passive scalar is a diffusing contaminant immersed in a fluid flow whose presence has no dynamical effect on the fluid motion and its theoretical and physical significance is obvious. On one hand, the passivity leads to linear equations and consequently many rigorous, closed-form results. On the other hand, many physical observables can be reasonably modeled as passive scalars under diverse field or laboratory settings, such as temperature, moisture, salinity and dye concentration, and the dynamic distributions of such scalar fields are closely related to the transport and

mixing properties of the flow fields. Therefore, passive tracer behaviors are critical to our understanding of the key turbulent transport and mixing mechanisms governing the environment in which we live, ranging from as small as human cells, to as large as the atmosphere and the ocean.

In the case of geophysical systems, there has been considerable scientific effort in recent decades attempting to identify the major mixing mechanisms involved in the observed distributions of a variety of tracers over a broad range of temporal and spatial scales. Typically, these distributions exhibit very large and sudden fluctuations and admit non-Gaussian statistics, which is termed *"scalar intermittency"* . Such observed geophysical and laboratory examples include single point temperature measurements in high Raleigh number convection experiments (Castaing et al., 1989; Ching, 1991) and in high Reynolds number stratified turbulence (Gollub et al., 1991; Thoroddsen and van Atta, 2006), atmospheric wind data (Sreenivasan and Antonia, 1997), and aircraft measurements of stratospheric aerosols (Sparling, 2000). This is inconsistent with the omnipresent Gaussian assumptions in operational meteorology and climatology, due to their mathematical simplicity (Kalman, 1960). And these realistic, scale dependent *probability density functions* (PDFs) drastically change the prediction of the state of the environment as well as of some fundamental changes it might undergo. Therefore, one outstanding problem arises: what are the origins and basic physical mechanisms responsible for generating these non-Gaussian (heavy-tailed) distributions?

The most dominant difficulty in the solution to this problem comes from the diversity of scales and physics in the geographical systems. For example, it is has been suggested that the importance of chaotic and random advection to the stirring and mixing of the atmosphere differs considerably from one scale to another (Shepherd et al., 2000). Although there has been a great effort directed to derive phenomenological models to describe and predict passive scalar intermittency, there is no general, rigorous method that is derived from first principle, hydrodynamic equations to the author's knowledge. As the central part of this thesis, the investigation of the role that stochastic effects, random initial tracer fields, fluid flows and external sources, play in developing scalar intermittency targets at the inherited statistics of passive tracers altered by the interaction between random advection and diffusion. In particular, we want to reveal the spatio-temporal development and the scale dependence of fat tails in the probability density function for the tracer, which is initially a normal distribution. When the system is not very turbulent and there is a strong scale separation between the velocity scale and that of the passive tracer, Gaussianity often persists and parametrization and

homogenization techniques enable large scale models to provide accurate results that agree with realistic data sets (Grabowski, 2004), without expensive resolution for complete, small scale turbulence. However, the highly turbulent feature of many complex systems eliminates such separation in the sense that the active scales of the flow field and those of the tracers overlap. In such cases, traditional treatments may not offer a complete description for the dynamics of the passive tracer fields for which new models and characterizations should therefore be explored.

Subject to appropriate initial and boundary conditions, the evolution of a passive scalar field, $T(\vec{x}, t)$, is governed by the *advection-diffusion equation:*

$$\frac{\partial T}{\partial t} + \vec{V}(\vec{x}, t) \cdot \nabla T = \kappa \Delta T + f(\vec{x}, t), \qquad \vec{x} \in \mathbb{R}^3, t > 0 \tag{1.1}$$

where $\vec{V}(\vec{x}, t)$ is an incompressible velocity field, κ is the molecular diffusivity of the scalar and $f(\vec{x}, t)$ is the external forcing. Such dynamics are linear, but involve random coefficients since the initial condition, the velocity field and the external forcing are all prescribed combinations of deterministic and stochastic components. Consequently, a fundamental question is to predict the inherited statistics (probability measure) of the scalar field which is a complicated interaction between different sources of stochasticity. Nonetheless, this is the simplest scenario to understand the observations of intermittency via partial differential equations with random coefficients (Castaing et al., 1989; Chertkov et al., 1995; Chertkov et al., 1997; Chertkov et al., 1998; Kraichnan, 1968; McLaughlin and Majda, 1996; Pierrehumbert, 2000; She and Orszag, 1991; Pumir et al., 1991; Plasting and Young, 2006; Shraiman and Siggia, 1994), which are infinite dimensional systems in finite dimensional spaces. In the case of random passive scalars, such systems have been recognized by the closed evolution equations of the statistical moments in higher dimensional spaces. The linearity of Eq. (1.1) makes such problems tractable, but nonetheless extremely difficult and it is often necessary to appeal to Monte Carlo simulation to gain insight. There are extremely few mathematical analyses on which to base the validity of such simulations.

The Chicago convection experiments (Castaing et al., 1989) in fact motivated an enormous theoretical effort to understand this scalar intermittency (heavy-tailed scalar distributions) in the context of the linear evolution of a passive scalar diffusing in the presence of random advection, for extensive summary, see the review article by Majda and Kramer (Majda and Kramer, 1999). The general picture which has emerged is that rare, long lived, infinitesimal fluctuations in a random velocity are responsible

for establishing the heavy tail in diffusing passive scalars. This picture is borne out through exact calculations involving the high moment asymptotics for statistical moments of the scalar fields (Bronski and McLaughlin, 2000b; Majda, 1993b), through stochastic analysis (Vanden-Eijnden, 2001), through instanton type field theoretic calculations (Chertkov et al., 1998), and through numerical simulation (Holzer and Siggia, 1994; Pierrehumbert, 2000). All of the theoretical calculations have involved highly idealized random flow geometries inspired by Batchelor and Kraichnan's proposition that the turbulent dynamics of small spatial scale passive tracers can be approximated by random but linear straining (Batchelor, 1959; Kraichnan, 1968). In other words, we can *locally* write the turbulent flow field as $\vec{V}(\vec{x},t) = \mathbf{A}\cdot\vec{x}$ where $\mathbf{A}$, a random, rank-2 tensor representing the principal-rate-of-strain directions and strain parameters subject to incompressibility, can be assumed to be constant over the small scales of interest. Then a class of *simple shear models* (Avellaneda and Majda, 1991; Majda and Kramer, 1999) can be developed, whose simplicity allows rigorous analysis with nontrivial physical relevance. Even in those simplified geometries, only asymptotic information about the PDF tail was available. For these fluid flows which are random shear layers, the scalar is fluctuating either in the presence of a large scale, mean gradient (Bourlioux and Majda, 2002), or in the freely decaying case (Bronski and McLaughlin, 1997; Bronski and McLaughlin, 2000b; Bronski and McLaughlin, 2000a; Bronski, 2003; Majda, 1993a; Majda, 1993b; Majda and Kramer, 1999; McLaughlin and Majda, 1996; Vanden-Eijnden, 2001). We focus upon the freely decaying scalar case in this thesis.

To understand what is involved with calculating the PDF or the solution of a random PDE, path integrals are generally unavoidable. To see this, consider the evolution of a diffusing passive tracer advected by a general stochastic velocity field $\vec{V}_\omega(\vec{x},t)$. Given a fixed realization of $\vec{V}_\omega(\vec{x},t)$, the scalar T is uniquely determined by the *Feynman-Kac's formula*:

$$T(\vec{x},t) = E_{\mathbf{B}}[T_0(\vec{X}_{\mathbf{B},\omega}(t))] \tag{1.2}$$

where $E_{\mathbf{B}}$ is the statistical average over all the paths $\vec{X}_{\mathbf{B},\omega}(s), 0 \le s \le t$ which satisfies the *stochastic differential equation*:

$$d\vec{X}_{\mathbf{B},\omega}(s) = -\vec{V}_\omega(\vec{X}_{\mathbf{B},\omega}(s), t-s)ds + \sqrt{2\kappa}\, d\mathbf{B}(t), \qquad \vec{X}_{\mathbf{B},\omega}(0) = \vec{x} \tag{1.3}$$

with $\mathbf{B}(t)$ as the standard Brownian Motion and κ is the molecular diffusivity of the scalar. Therefore, the PDF for the scalar T conditioned on $\vec{V}_\omega$ is a Dirac measure $\delta(T - E_{\mathbf{B}}[T_0(\vec{X}_{\mathbf{B},\omega}(t))])$. However, the unconditioned PDF for T is simply not tractable

in general, since one has to integrate over all realizations of V_ω, namely,

$$P(T) = \int_\Omega p(T|\vec{V}_\omega) p(\vec{V}_\omega) d\mu(\vec{V}_\omega) = \int_\Omega \delta\Big(T - E_{\mathbf{B}}[T_0(\vec{X}_{\mathbf{B},\omega}(t))]\Big) p(\vec{V}_\omega) d\mu(\vec{V}_\omega) \qquad (1.4)$$

where Ω is the space of all realizations of the random velocity field $\vec{V}_\omega$ and $d\mu(\vec{V}_\omega)$ is the measure associated to the particular path. When the velocity field admits randomness in both space and time, only very few analyses exist. For example, Kraichnan derived closed evolution equations for statistical moments in rapidly fluctuating fluid flows (white noise limit) (Kraichnan, 1968), and Majda rigorously established, using path integral methods, the general evolution equation governing the N-point correlation function for stationary (in space and time) random shear layers (Majda, 1993b). Also, for scalar fields evolving in an imposed mean scalar gradient (a maintained, large-scale spatially linear scalar profile), Bourlioux and Majda have presented the long time PDF analysis for shear layers with a transverse, temporally varying wind field (Bourlioux and Majda, 2002). For some special cases in which the fluid flows are functionally dependent upon a finite number of stochastic processes $w_j(t)$ (Bronski and McLaughlin, 2000a; Bronski and McLaughlin, 2000b; Chertkov et al., 1998; Balkovsky et al., 2001; Majda, 1993b; McLaughlin and Majda, 1996), progress can be made. For example, for fluid flows admitting a linear spatial structure (such as the Majda model which is a linear shear multiplied by temporally varying, Gaussian white noise), an explicit solution to the conditional Feynman-Kac solution in (1.1) is available by the method of characteristics. Even with this explicit, random Green's function, obtaining the complete probability measure for the random, advected scalar is not possible in general, and requires consideration of the second functional integral in (1.4). Currently, for random, spatially linear fluid flow, existing general results have succeeded in calculating, in closed form, the statistical moments and the PDF tail (Bronski and McLaughlin, 2000a; Bronski and McLaughlin, 2000b; Majda, 1993b; McLaughlin and Majda, 1996; Balkovsky et al., 2001; Vanden-Eijnden, 2001), but not the full measure.

The scope of this thesis is as follows: In Chapter 2, we study a simplified model for which the entire spatio-temporal PDF may be explicitly calculated by reducing the problem to one-dimensional with deterministic initial data (imagine that you have absolutely accurate control on the amount and location of the dye being injected into the fluid) and the flow field is simply a space independent, temporal white noise. Our purpose is to use this model as a testbed to develop numerical techniques for reconstructing a PDF from its statistical moments. By focusing on this uni-directional,

constant in space, rapidly fluctuating (white in time), Gaussian random advection, we establish here a family of models for which the statistical moments are explicit simple algebraic expressions for any moment number, and for which the complete, explicit, spatio-temporal probability density function is available for specialized initial data. In turn, for more complex initial data, we present a reconstruction procedure based upon orthogonal polynomial expansion, which can approximate the exact PDF very well with a relative error of less than 1% when the first 4 moments are used for the summation, along with high moment number moments asymptotically equal to true moments. Then we use these tools to benchmark Monte-Carlo simulations showing the spatio-temporal evolution of more general PDFs. These calculations give a rigorous and complete demonstration of the role which the Péclet number, a nondimensional number which measures the relative importance of advection versus diffusion, plays in adjusting the spatial structure of the PDF. Surprisingly, even in this simple flow, the interaction of advection with diffusion is very complicated, and the dynamics smooth in a precise way the initially Dirac scalar distributions for the deterministic initial data. The Péclet number, the non-dimensional parameter characterizing the relative importance of random advection to molecular diffusion, is shown to move these algebraic singularities from the diffusion dominated regime, with probability focused at the highest scalar values, to the advective dominated regime, with probability collecting at the zero scalar value. For general models where only moment information is available, the reconstruction procedure is also applicable, provided that the scalar can be renormalized onto a bounded interval.

In Chapter 3, we will discuss the new developments of the simple shear model introduced by Majda in 1993 (Majda, 1993b), which assumed that the velocity field has a simple spatial structure which is a linear shear layer multiplied by a Gaussian white noise process. In this model, the N^{th} statistical moment of the tracer may be expressed as an explicit N-dimensional integral and this information was used to predict the emergence of heavy-tailed PDFs in previous works. Here, we present new, dynamical behavior for the PDF which occurs within this model by re-formulating the scalar PDF as a conditional mixing of Gaussian probability measures via the law of total probability, whose direct numerical evaluation is non-trivial, since both the conditional variance and the measure of the rescaled L^2-norm of Wiener Process involved take integral forms. Using a combination of simulation and rigorous analysis, we find that for random initial data whose two-point spatial correlation possesses multiple peaks, we document that the PDF admits an interesting "breathing" phenomena. This non-monotonic behavior

is characterized by an initial growth of the probability density in the core beyond those set by the long time, limiting invariant measure. Simultaneously, the concavity of the PDF is anomalously larger than the invariant measure over several standard deviations. Subsequently, the PDF core in turn decays to the invariant measure. Alternatively, for initial data not possessing a multiply-peaked correlation function, the evolution to the invariant measure is monotonic in the core, and the concavity in the core region is lower than the invariant measure. This behavior we first observed in Monte Carlo simulations, is carefully documented through a more accurate numerical evaluation of an integral representation of the PDF we present. In turn, we identify a new invariant measure which captures this breathing behavior through a distinguished, diffusionless limit. Additionally, we establish that the invariant measure always has a Gaussian core for a wide range of initial cut-off functions, and compute the explicit time scales for the PDF tail to approach the invariant measure. Further, a rigorous analytical prediction of the breathing phenomena is presented for a special class of initial data. Lastly, the partial ergodicity of the model is discussed, where we find that the tracer PDF is semi-ergodic in the sense that the ensemble average over the initial random field can be replaced by its empirical, spatial average.

In Chapter 4, we consider several flows and initial conditions that give rise to explicit random Green's functions and potentially closed formulas for the scalar statistical moments or even a simple (integral) representation of the full scalar PDF as in the models discussed in Chapter 2 and 3. We seek to extend the methodology to more realistic scenarios and explain the scalar intermittency observed in various experiments.

To explore the possibilities of applying the aforementioned analytical methods to geophysical flows, we numerically simulate the evolution of a random passive scalar field in a large scale, mid-latitude, wind driven, shallow water model in Chapter 5. Many important problems in geosciences maybe formulated in terms of distinguished limits and weak nonlinear analysis (Majda, 2003) and the full simulation of these nonlinear problems is critical to identify that the features that these simplified models are capable to capture. With this in mind, viscous, rotational and random effects are incoporated into the numerical package CLAWPACK (Leveque, 2002), for its proclaimed accuracy and versatility to solve for PDE systems governed by different conservation laws. Here, the viscous and coriolis terms are added as sources to the inviscid, hyperbolic system and an operator-splitting scheme is used. In this chapter, some preliminary results are shown to illustrate the emergence of scalar intermittency in the double-gyre, shallow water model. This numerical study in such a complex system will undoubtedly inspire

and illuminate subsequent analytical efforts.

At the end of this thesis, some non-trivial calculations are shown in details in the appendices.

Chapter 2

An Elementary Example

In this chapter, we simplified the general governing equation (1.1) by consider the evolution of a decaying passive scalar with a random uni-directional, spatially constant wind, for ease in exposition, restricted to one spatial dimension. Then governing stochastic PDE is reduced to

$$\begin{aligned} \frac{\partial T}{\partial t} + \gamma(t)\frac{\partial T}{\partial x} &= \kappa \frac{\partial^2 T}{\partial x^2}, \qquad -\infty < x < \infty, \quad t > 0 \\ T|_{\,t=0} &= T_0(x) \end{aligned} \tag{2.1}$$

where $\gamma(t)$ is a Gaussian white noise satisfying

$$\langle \gamma(t) \rangle_\gamma = 0, \qquad \langle \gamma(t)\gamma(t') \rangle_\gamma = \sigma^2 \delta(t - t') \tag{2.2}$$

where $\langle \cdot \rangle_\gamma$ denotes the ensemble average over the statistics of γ.

Suppose that the initial data $T_0(x)$ has a typical length scale L. Then we have three dimensional parameters, σ^2, κ and L, from which we can only form one non-dimensional parameter for Eq.(3.1), the Péclet number $\mathrm{Pe} = \sigma^2/\kappa$, that characterizes the intensity of the random advection relative to molecular diffusion. If we let $x' = x/L$, $\tau = t\sigma^2/L^2$ and $\gamma'(\tau) = \gamma(t)L/\sigma^2$, the evolution of the tracer is governed by the non-dimensionalized equation

$$\begin{aligned} \frac{\partial T}{\partial \tau} + \gamma'(\tau)\frac{\partial T}{\partial x'} &= \frac{1}{\mathrm{Pe}} \frac{\partial^2 T}{\partial x'^2} \\ T|_{\,\tau=0} &= T_0'(x') \end{aligned} \tag{2.3}$$

where $\gamma'(\tau)$ is the non-dimensionalized white noise and $\langle \gamma'(\tau)\gamma'(\tau') \rangle_{\gamma'} = \delta(\tau - \tau')$. Notice that the length scale L does not appear in the Eq.(2.3). The initial length scale

is irrelevant here since if we have a different length scale $\tilde{L}$ in the data, then letting $\tilde{x} = x'\tilde{L}/L$ and $\tilde{\tau} = \tau\tilde{L}^2/L^2$ will recover exactly the same equation (2.3) but in the variables $(\tilde{x}, \tilde{\tau})$. This feature is essentially introduced by the vanishing autocorrelation time of the white noise.

This particular time varying fluid flow, while trivial in spatial structure, gives rise to an interesting family of scalar probability measures. These measures give a connection between the respective limits of high and low Péclet number. At zero Péclet (no advection), the solution is trivial, and the ensuing probability measure for the values of the scalar field normalized by the spatial maximum is simply a Dirac mass (delta function) with support set by heat solution (see Result 1, and weak convergence calculations below in Section 2.1.5). At the alternative limit, we will see that in the limit of vanishing diffusion the probability measure for renormalized tracer values is also a Dirac mass (delta function) at large times, only with different support set. For finite, non-zero Péclet numbers, the probability measure is a smoother distribution, set by a competition between random advection and diffusion, which we can explicitly compute in this special case to see the connection between these two distributional limits.

The main results for this model are the following:

1. For initial data $T_0(x) = e^{-x^2}$, at any fixed location x and time t, the random scalar $T(x,t)$ can be renormalized by a deterministic function $T_{max}(t) = 1/\sqrt{4\kappa t + 1}$, so that the ensuing *probability density function* (PDF) for $\xi := T(x,t)/T_{max}(t)$ has compact support, namely,

$$\text{Prob}(\xi \notin [0,1]) = 0 \tag{2.4}$$

Moreover,

(a) The exact spatio-temporal PDF of the renormalized random scalar ξ is

$$P_{x,t}(\xi) = \sqrt{\frac{1}{\beta\pi}}\, \frac{e^{-\frac{x^2}{a}}\ \xi^{\frac{1}{\beta}-1}\ \cosh\sqrt{-\frac{4b'x^2}{a^2}\ln\xi}}{\sqrt{-\ln\xi}} \tag{2.5}$$

for any $\xi \in (0,1)$, where

$$a = 2\sigma^2 t, \qquad b' = 4\kappa t + 1, \qquad \beta = a/b' \to \frac{\text{Pe}}{2}\ (t \to \infty) \tag{2.6}$$

This measure has a singular structure at $\xi = 1$ and if $\beta > 1, x \neq 0$, it is also singular at $\xi = 0$. It converges weakly to the Dirac delta measure $\delta(\xi)$ when $\beta \to \infty$ (high Péclet number limit for pure random advection) and to $\delta(\xi - e^{-x^2/b'})$ when $\beta \to 0$ (low Péclet number limit for pure diffusion).

(b) The N^{th} statistical moment of the random tracer $T(x,t)$ can be computed analytically as:

$$\langle T^N(x,t)\rangle_\gamma = \frac{e^{-\frac{Nx^2}{Na+b'}}}{\sqrt{Nab'^{N-1}+b'^N}} \tag{2.7}$$

for $N = 0, 1, 2, \cdots$

(c) We formally expand the PDF of the renormalized random tracer by orthogonal polynomials as

$$P_{x,t}(\xi) = \frac{\sum_{n=0}^{\infty} C_n\, Q_n(\xi)}{r(\xi)} \tag{2.8}$$

where $\{Q_n(\xi)\}_{n=0}^{\infty}$ is a family of orthogonal polynomials defined on $[-1,1]$ or $[0,1]$, $r(\xi)$ is a regularization function and the coefficients C_n are obtained from the statistical moments of the tracer (2.7). For a specific choice of the polynomial family and $r(\xi)$, the pointwise convergence of these reconstructions depends on the values of x and β. Given the convergence, the fact that $P(\xi)$ is compactly supported by $[0,1]$ guarantees the uniqueness of the expansion. Moreover, with the shifted Chebyshev polynomials, the reconstructed PDF has a relative error of less than 1% when the first 4 moments are used for the summation (2.8).

2. For the bimodal initial data $T_0(x) = \frac{\partial(e^{-x^2})}{\partial x} = 2xe^{-x^2}$, $T(x,t)$ can also be renormalized by $T_{max}(t) = \sqrt{2e^{-1}}/(4\kappa t+1)$, such that $\text{Prob}(\xi \notin [-1,1]) = 0$. So again the probability measure is compactly supported. In this case, the exact, closed-form PDF for the renormalized tracer is available only in a long time limit and it is related to the two branches of the *Lambert W-functions*(Corless et al., 1997). However, the exact statistical moments of the random tracer $T(x,t)$ are still available at all times in analogy to (2.7). Thus we are able to reconstruct the PDF with orthogonal polynomials as described in Result 1.2.

3. Monte-Carlo (MC) simulations, benchmarked on Result 1, present a detailed picture for the spatio-temporal evolution of the PDF when the exact solution to the moment problem is unknown. The simulation results also illustrate how different values of Péclet number change the spatial structure of the PDF. Further, simulations are preformed for initial data $T_0(x) = 2xe^{-x^2}$ and $T_0(x) = e^{-(x-A)^2} + e^{-(x+A)^2}$ respectively, for which exact PDF's at all times are not available.

2.1 Derivation of the Exact PDF and Moments

2.1.1 Exact PDF for $T_0(x) = e^{-x^2}$

For the unimodal, Gaussian initial data $T_0(x) = e^{-x^2}$, the exact PDF for the evolving random scalar field $T(x,t)$ can be computed analytically via direct statistical inversion, since

$$T(x,t) = \frac{1}{\sqrt{1+4\kappa t}} \exp\Big(- \frac{(x - W(t))^2}{1+4\kappa t}\Big) \tag{2.9}$$

which is a random translation of the pure heat solution, where $W(t) = \int_0^t \gamma(s)ds$ is a *Wiener Process*(Gardiner, 1985). For example, when $x = 0$

$$\begin{aligned} \text{Prob}(\sqrt{1+4\kappa t}\, T(0,t) \le \xi) &= \text{Prob}(e^{-\frac{(W(t))^2}{1+4\kappa t}} \le \xi) \\ &= 1 - \text{Erf}\Big(\sqrt{-\frac{1+4\kappa t}{2\sigma^2 t}\ \ln \xi}\,\Big) \end{aligned} \tag{2.10}$$

where $\text{Erf}(\cdot)$ is the error function. Thus, the ensuing probability density function is

$$P_{0,t}(\xi) := \frac{\partial}{\partial \xi}\Big[1 - \text{Erf}\Big(\sqrt{-\frac{1+4\kappa t}{2\sigma^2 t}\ \ln \xi}\,\Big)\Big] = \frac{\xi^{\frac{1}{\beta}-1}}{\sqrt{-\beta\pi \ln \xi}}. \tag{2.11}$$

with $\beta = \frac{2\sigma^2 t}{1+4\kappa t}$. To recover the general case (2.5) for $x \neq 0$, similar but more complicated algebra as in Eq.(2.10) is needed. Instead, we follow an alternative derivation using Laplace inversion in Section 2.1.4.

2.1.2 Exact Statistical Moments for General Initial Data

For general initial data, the direct statistical inversion technique shown in Eq.(2.10) is not always applicable, even when an analytic solution similar to Eq.(2.9) is available. However, the exact statistical moments of the random scalar are often accessible. The solution to Eq. (3.1) can be written via Fourier transform as

$$T(x,t) = \int_{-\infty}^{\infty} e^{2\pi i k[x - W(t)] - 4\pi^2 \kappa k^2 t}\ \hat{T}_0(k)\ dk \tag{2.12}$$

where $\hat{T}_0(k)$ is the Fourier transform of $T_0(x)$. In fact, this is just a "drifted" version of the fundamental heat solution, spatially shifted by $-W(t)$. Consequently, we have the following formula for arbitrary moments of the tracer field, T, satisfying Eq. (3.1):

$$\begin{aligned}\langle T^N(x,t)\rangle_\gamma &= \langle\prod_{j=1}^{N} T(x_j,t)\rangle_\gamma \\ &= \int_{R^N} e^{2\pi i\mathbf{k}\cdot\mathbf{x}-4\pi^2\kappa|\mathbf{k}|^2 t}\left\langle e^{-2\pi i\sum_{j=1}^N k_j W(t)}\right\rangle_\gamma \prod_{j=1}^{N}\hat{T}_0(k_j)d\mathbf{k}\end{aligned} \tag{2.13}$$

with $\mathbf{x}=(x_1,x_2,...,x_N)=(x,x,...,x)$ and $\mathbf{k}=(k_1,k_2,...,k_N)$.

Since $-2\pi i\sum_{j=1}^N k_j\, W(t)$ is a mean-zero, Gaussian random variable, we have

$$\langle e^{-2\pi i\sum_{j=1}^N k_j\, W(t)}\rangle_\gamma = e^{-2\pi^2\sigma^2 t(\sum_{j=1}^N k_j)^2}. \tag{2.14}$$

and Eq. (2.13) reduces to

$$\langle T^N\rangle_\gamma = \int_{R^N} e^{2\pi i\mathbf{k}\cdot\mathbf{x}-\mathbf{k}^T A_N\mathbf{k}}\prod_{j=1}^{N}\hat{T}_0(k_j)d\mathbf{k} \tag{2.15}$$

where

$$A_N = \pi^2\begin{pmatrix} a+b & a & \cdots & a \\ a & a+b & \cdots & a \\ \cdots & \cdots & \cdots & \cdots \\ a & a & \cdots & a+b \end{pmatrix} \tag{2.16}$$

with

$$a = 2\sigma^2 t \qquad \text{and} \qquad b = 4\kappa t \tag{2.17}$$

Since A_N is *symmetric positive definite*, computing the exact moments is equivalent to diagonalizing a quadratic form. We start with the special case

$$T_0(x) = \delta(x) \tag{2.18}$$

such that $\prod_{j=1}^N \hat{T}_0(k_j)=1$. The familiar result for a N-dimensional Gaussian integral reads:

$$\langle T^N(0,t)\rangle \quad = \quad \int_{R^N} e^{-\mathbf{k}^T A_N\mathbf{k}}d\mathbf{k} \quad = \quad \frac{\pi^{\frac{N}{2}}}{\sqrt{\det A_N}} \tag{2.19}$$

The determinant in the denominator does not vanish provided $b\neq 0$ in Eq. (2.17) and it can be easily shown by induction that $\det A_N = \pi^{2N}(Nab^{N-1}+b^N)$. For $x\neq 0$, we need to diagonalize A_N as $A_N = V'\Lambda V$ where $V=\{\vec{v}_i\}_{i=1}^N=\{v_{ij}\}_{i,j=1}^N$ is the orthogonal

matrix composed of A_N's eigenvectors and Λ is the diagonal matrix of its eigenvalues

$$\Lambda = \pi^2 \begin{pmatrix} b & 0 & \cdots & 0 & 0 \\ 0 & b & \cdots & 0 & 0 \\ \cdots & \cdots & \cdots & \cdots & \cdots \\ 0 & 0 & \cdots & b & 0 \\ 0 & 0 & \cdots & 0 & Na+b \end{pmatrix} \tag{2.20}$$

Changing variables by $\bar{\mathbf{k}} = V\mathbf{k}$, Eq. (2.15) becomes:

$$\begin{aligned} \langle T^N(x,t)\rangle_\gamma &= \int_{R^N} e^{2\pi i x \sum_{m,n=1}^{N} \bar{k}_m v_{mn} - \pi^2 b \sum_{m=1}^{N-1} \bar{k}_m^2 - \pi^2 (Na+b)\bar{k}_N^2} d\bar{\mathbf{k}} \\ &= \int_{-\infty}^{\infty} e^{2\pi i V_N x \bar{k}_N - \pi^2 (Na+b)\bar{k}_N^2} d\bar{k}_N \prod_{m=1}^{N-1} \int_{-\infty}^{\infty} e^{2\pi i V_m x \bar{k}_m - \pi^2 b \bar{k}_m^2} d\bar{k}_m \\ &= \frac{\pi^{\frac{N}{2}}}{\sqrt{\det A_N}}\, e^{-x^2(\frac{\sum_{m=1}^{N-1} V_m^2}{b} + \frac{V_N^2}{Na+b})} \\ &= \frac{\pi^{-\frac{N}{2}}}{\sqrt{Nab^{N-1}+b^N}}\, e^{-\frac{Nx^2}{Na+b}} \end{aligned} \tag{2.21}$$

where $V_m = \sum_{n=1}^{N} v_{mn}, m = 1, 2, \cdots, N$. We will prove Eq.(2.21) by showing $V_m = 0$ for $m < N$, $V_N = \sqrt{N}$ in Appendix. In particular, when $x = 0$, we retrieve formula (2.19).

To generalize Eq.(2.21) for arbitrary $T_0(x)$, we just apply the Convolution Theorem to Eq.(2.13) and read

$$\langle T^N\rangle_\gamma = \frac{\pi^{\frac{N}{2}}}{\sqrt{\det A_N}} \int_{\mathbb{R}^N} \exp\Big(-\frac{1}{b}[|\mathbf{y}|^2 - \frac{a(\sum_{j=1}^{N} y_j)^2}{aN+b}]\Big) \prod_{j=1}^{N} T_0(x-y_j)\, d\mathbf{y} \tag{2.22}$$

In particular, for $T_0(x) = e^{-x^2}$, Eq.(2.7) is recovered by computing the above integral, which is the same as in the case of $T_0(x) = \delta(x)$ except that b is replaced by $b' = b+1$.

Next we introduce the random variable $\xi := \frac{T(x,t)}{T_{max}(t)}$ and its N^{th}-order statistical moment $M_N := \langle \xi^N \rangle_\gamma$ and we denote its PDF by $P_{x,t}(\xi)$. Since

$$M_N = \int_{-\infty}^{\infty} \xi^N P_{x,t}(\xi)\, d\xi \geq \int_1^{\infty} \xi^N P_{x,t}(\xi)\, d\xi \geq \int_1^{\infty} P_{x,t}(\xi)\, d\xi = \text{Prob}(\xi > 1) \tag{2.23}$$

and from Eq.(2.7)

$$M_N = \frac{\langle T^N(x,t)\rangle_\gamma}{T^N_{max}(t)} = \frac{e^{-\frac{Nx^2}{aN+b'}}}{\sqrt{1+\beta N}} \to 0 \tag{2.24}$$

as $N \to \infty$, we conclude that

$$\text{Prob}(\xi > 1) = 0 \tag{2.25}$$

which ultimately leads to Eq.(2.4). This seems redundant here by the simple definition of ξ, while an analogous argument is useful to infer a compactly-supported measure when only the moment information of ξ is available.

2.1.3 Long Time Asymptotics of the Moments

In the long-time limit, we can apply Eq. (2.19) to study the asymptotic behavior of the moments for more general initial conditions and at locations away from the origin. Without loss of generality, we use some of the results from Eq. (2.19) through (2.21) and consider

$$\langle T^N\rangle_\gamma = \int_{-\infty}^{\infty} e^{2\pi i\sqrt{N}x\bar{k}_N - \pi^2(Na+b)\bar{k}_N^2 - \pi^2 b\sum_{n=1}^{N-1}\bar{k}_n^2} \prod_{n=1}^{N} \hat{T}_0(\bar{k}_n)d\bar{\mathbf{k}} \tag{2.26}$$

for an unknown, general $T_0(x)$. For a large time t, if we rescale $\bar{\mathbf{k}}$ as $\bar{\mathbf{k}} = \frac{\mathbf{k}}{\sqrt{t}}$, when $t \to \infty$,

$$\begin{aligned}
\langle T^N\rangle_\gamma &= \frac{1}{\sqrt{t}}\int_{-\infty}^{\infty} e^{2\pi i\sqrt{N}x\bar{k}_N - \pi^2(Na+b)\bar{k}_N^2 - \pi^2 b\sum_{n=1}^{N-1}\bar{k}_n^2} \prod_{n=1}^{N} \hat{T}(\bar{k}_n)d\bar{\mathbf{k}} \\
&= \frac{1}{\sqrt{t}}\int_{-\infty}^{\infty} e^{2\pi i\sqrt{N}x\frac{k_N}{\sqrt{t}} - \pi^2\frac{Na+b}{t}k_N^2 - \pi^2\frac{b}{t}\sum_{n=1}^{N-1}k_n^2} \prod_{n=1}^{N} \hat{T}(\frac{k_n}{\sqrt{t}})d\mathbf{k} \\
&\sim \frac{1}{\sqrt{t}}\hat{T}(0)^N \int e^{-\pi^2\frac{Na+b}{t}k_N^2 - \pi^2\frac{b}{t}\sum_{n=1}^{N-1}k_n^2} d\mathbf{k} \\
&= \hat{T}(0)^N \int e^{-\pi^2(Na+b)\bar{k}_N^2 - \pi^2 b\sum_{n=1}^{N-1}\bar{k}_n^2} d\bar{\mathbf{k}} \\
&= \hat{T}(0)^N \frac{\pi^{\frac{N}{2}}}{\sqrt{\det A_N}}
\end{aligned} \tag{2.27}$$

provided $\hat{T}_0(0) \neq 0$ and the quantities $\frac{a}{t}$ and $\frac{b}{t}$ have finite limits as $t \to \infty$, which is guaranteed by definition (2.17) given finite σ^2 and κ. Therefore, in the long time

limit, the statistical moments of T are independent of x. To see this, observe that the last two factors in the exponent of the exponential are time-independent constants through Eq. (2.17). Consequently the complex part of the exponential is subdominant at long time. Notice that this asymptotic convergence should be uniform only over compact sets, which will be illustrated in Section 2.4 without a rigorous proof. More importantly, from Eq.(2.27), the tracer field can be renormalized such that the moments of the renormalized tracer ξ, $\langle \xi^N \rangle$, are asymptotically *self-similar*, namely, independent of *both* x and t for large times.

2.1.4 Exact PDF and the Inverse Laplace Transform of the Moment Function

The problem of determining a compactly-supported measure $P(\xi)\, d\xi$ from its moments is known as the *Hausdorff Moment Problem*. Once the exact moment of arbitrary order is determined, the problem has a unique solution(Shohat and Tamarkin, 1943). Define the *moment function* of $P(\xi)$ as

$$\mu(s) = \int_0^1 \xi^s P(\xi) d\xi = \int_0^\infty e^{-st} e^{-t} P(e^{-t}) dt = \mathcal{L}[e^{-t} P(e^{-t})](s) \tag{2.28}$$

whose values evaluated at $s = 0, 1, 2, \cdots$ are exactly the statistical moments of P. Then

$$P(\xi) = \frac{\mathcal{L}^{-1}[\mu(s)](-\ln \xi)}{\xi} \tag{2.29}$$

For the particular initial data $T_0(x) = e^{-x^2}$, we know from Eq.(2.4) that the PDF of the renormalized tracer ξ is compactly supported by $[0, 1]$. Now define

$$\mu^*(s) := \frac{e^{-\frac{sx^2}{as+b'}}}{\sqrt{1+\beta s}}. \tag{2.30}$$

It follows from Eq.(2.24) that $\mu^*(N) = \langle \xi^N \rangle_\gamma$ for $N = 0, 1, 2, \cdots$. If $\mu(t) \equiv \mu^*(t)$, the exact PDF (2.5) for the renormalized random tracer can also be derived via the inverse Laplace Transform of $\mu^*(t)$ through Eq.(2.29). The necessary and sufficient conditions for $\mu(t) \equiv \mu^*(t)$ may be found in the literature(Shohat and Tamarkin, 1943). However, these conditions appear difficult to verify analytically. Alternatively, we perform the Laplace Transform for $\mu^*(t)$ and compare *a posteriori* the result with Eq.(2.5). First

notice that

$$\mu^*(s) = \frac{\sqrt{a}}{x}\, e^{-\frac{x^2}{a}} \frac{e^{\frac{1}{s'}}}{\sqrt{s'}} = \frac{\sqrt{a}}{x}\, e^{-\frac{x^2}{a}} \bar{\mu}(s') \tag{2.31}$$

with $s' = \frac{a^2 s}{x^2 b'} + \frac{a}{x^2}$ and we assume $a, b', x \neq 0$ without loss of generality. We can show that(Abramowitz and Stegun, 1965)

$$\begin{aligned} \mathcal{L}^{-1}[\mu^*(s)](t) &= \frac{\sqrt{a}}{x}\, e^{-\frac{x^2}{a}} \mathcal{L}^{-1}[\bar{\mu}\Big(\frac{a^2 s}{x^2 b'} + \frac{a}{x^2}\Big)](t) \\ &= \frac{b'\sqrt{a}}{a^2 x} e^{-\frac{x^2}{a} - \frac{b'}{a} t} \mathcal{L}^{-1}[\bar{\mu}(s)]\Big(\frac{b' x^2 t}{a^2}\Big) \\ &= \sqrt{\frac{1}{\beta\pi}}\, \frac{e^{-\frac{t}{\beta} - \frac{x^2}{a}}\, \cosh\sqrt{\frac{4b' x^2 t}{a^2}}}{\sqrt{t}}. \end{aligned} \tag{2.32}$$

Assuming $\mu(t) \equiv \mu^*(t)$, then Eq.(2.29) and Eq.(2.32) yield the explicit formula for $P_{x,t}(\xi)$ which is identical to Eq.(2.5).

2.1.5 Distinguished Péclet Limits for $T_0(x) = e^{-x^2}$

If we consider the special case $x = 0$ for the exact moments Eq.(2.24) for the renormalized tracer ξ, two special cases emerge:

1. $0 < \beta \ll 1$. In the limit $\beta \to 0$ evidently $\langle \xi^N \rangle_\gamma \to 1$ for any N.

2. $\beta \gg 1$. In the limit $\beta \to \infty$ $\langle \xi^N \rangle_\gamma \to 0$ for any $N > 0$ except $N = 0$.

These two cases can be interpreted as the weak convergence of the PDF

$$P_{x,t}(\xi) = \sqrt{\frac{1}{\beta\pi}}\, \frac{\xi^{\frac{1}{\beta}-1}}{\sqrt{-\ln\xi}} \tag{2.33}$$

to Dirac delta measures when $\beta \to 0/\infty$. An important fact is that for fixed σ and κ, β is an increasing function of t and

$$\lim_{t\to\infty} \beta \;=\; \lim_{t\to\infty} \frac{2\sigma^2 t}{1 + 4\kappa t} \;=\; \frac{\sigma^2}{2\kappa} \;=\; \frac{\mathrm{Pe}}{2}. \tag{2.34}$$

It is not hard to generalize this result for $x \neq 0$ in the long time limit, from Eq.(2.27), since $P_{x,t}(\xi)$ is independent of x and it is only controlled by the Péclet number. Consequently, the distinguished limits of $P_{x,t}(\xi)$ at large times as $\mathrm{Pe} \to 0/\infty$ are equivalent to the singular limits as $\beta \to 0/\infty$. For any test function $\phi(\xi)$ defined on $[0, 1]$, we have

$$\begin{aligned}
\int_0^1 P_{x,t}(\xi)\phi(\xi)d\xi &= \frac{1}{\sqrt{\pi}}\int_0^1 \sqrt{\frac{1}{\beta}}\frac{e^{-\frac{x^2}{a}}\xi^{\frac{1}{\beta}-1}\cosh\left(2\sqrt{-\frac{b'x^2}{a^2}\ln\xi}\,\right)\phi(\xi)}{\sqrt{-\ln\xi}}\,d\xi \\
&= \frac{1}{\sqrt{\pi}}\int_0^\infty \sqrt{\frac{1}{\beta}}\frac{e^{-\frac{x^2}{a}-\frac{z}{\beta}}\cosh\left(2\sqrt{\frac{b'x^2}{a^2}z}\,\right)\phi(e^{-z})}{\sqrt{z}}\,dz \qquad (2.35)\\
&\approx \frac{2}{\sqrt{\pi}}\int_0^\infty e^{-y^2}\phi(e^{-(\sqrt{\beta}\,t+\frac{x}{\sqrt{b'}})^2})\,dy
\end{aligned}$$

after the change of variable $y = \sqrt{\frac{-\ln\xi}{\beta}} + \frac{x}{\sqrt{a}}$. Thus formally

$$\begin{aligned}
\int_0^1 P_{0,t}(\xi)\phi(\xi)d\xi &= \frac{1}{\sqrt{\pi}}\int_0^\infty \frac{e^{-y}\phi(e^{-\beta y})}{\sqrt{y}}\,dy \\
&\to \begin{cases} \frac{2}{\sqrt{\pi}}\phi(e^{-\frac{x^2}{b'}})\int_0^\infty e^{-y^2}\,dy, & \beta\to 0 \\ \\ \frac{2}{\sqrt{\pi}}\phi(0)\int_0^\infty e^{-y^2}\,dy, & \beta\to\infty \end{cases} \qquad (2.36)\\
&= \begin{cases} \phi(e^{-\frac{x^2}{b'}}), & \beta\to 0 \\ \\ \phi(0), & \beta\to\infty \end{cases}
\end{aligned}$$

Therefore $P_{x,t}(\xi)$ converges to $\delta(\xi - e^{-\frac{x^2}{b'}})$, which is exactly a Dirac delta measure at the pure heat solution, as $\beta \to 0$ and to $\delta(\xi)$ as $\beta \to \infty$, in a distributional sense. When β goes to 0, the random effects becomes negligible and the original equation (3.1) "degenerates" to a simple, deterministic heat equation. Thus the tracer will always be the pure heat solution with probability 1. In contrast, when $\beta \to \infty$, at any fixed spatial location x, the deterministic pure solution at that location is shifted by the random drift so far away, that $T(x,t)$ will almost certainly assume the infinitesimal values in the tails of the flattening Gaussian profile, namely, $T(x,t) = 0$ with probability 1.

For intermediate values of β, as we will see in the next section, the large moment asymptotics provide valuable information for the reconstruction of the PDF via orthogonal polynomials, when the exact PDF is unknown. Further, the values of β and x determine the convergence of the series reconstruction.

2.2 PDF Reconstruction from Moments Using Orthogonal Polynomial Approximants

As we mentioned before, the exact PDF for a tracer undergoing random advection and diffusion is generally unavailable while the exact moments are often accessible. Eq.(2.10) and (2.24) showed that renormalizing the moments of $T(x,t)$ by the maximum of the heat solution for $T_0(x) = e^{-x^2}$ leads to a measure compactly-supported by the interval $[0,1]$. Techniques to reconstruct the *distribution function* $D(\xi) = \int_a^\xi P(s)ds$ via Legendre polynomials using the moments exist in literature(Shohat and Tamarkin, 1943), when the density function $P(\xi)$ is compactly supported. However, the resulting distribution function will always be of bounded variations, while the PDF's we derived above have singularities and thus do not have a convergent, canonical Legendre expansion. Therefore in this paper, we seek for a direct polynomial reconstruction for the PDF, with coefficients also determined by the exact statistical moments. As a test problem, we implement this idea to the case $T_0(x) = e^{-x^2}$, for which the exact PDF (2.5) benchmarks the procedure and in turn we use the reconstructions to infer the behavior of more complicated measures.

2.2.1 Choice of Orthogonal Polynomials

To reconstruct the PDF as a series expansion, first we have to make a choice on the family of orthogonal polynomials defined on a bounded domain. Two canonical choices of such polynomials are Legendre polynomials and Chebyshev polynomials. We elect to use the Chebyshev polynomials of the first kind because, as we now show, the large moment asymptotics of our unknown PDF have the same scalings as those induced by any linear combination of orthonormal Chebyshev polynomials. The key to verify this assertion lies in the particular weight function,$(\sqrt{1-\xi^2})^{-1}$, for Chebyshev polynomials. Observe that if the measure is approximated as the zeroth order Chebyshev polynomial divided by the weight function and multiplied by a normalization constant

$$P_{0,t}(\xi) \approx \frac{2\,T_0(\xi)}{\pi\sqrt{1-\xi^2}} = \frac{2}{\pi\sqrt{1-\xi^2}},$$

then the large moment asymptotics are given by the following sequence of calculations:

$$\frac{\pi}{2}\langle \xi^N \rangle_\gamma \approx \int_0^1 \frac{\xi^N}{\sqrt{1-\xi^2}} d\xi = \int_0^\infty \frac{e^{-(N+1)u}}{\sqrt{1-e^{-2u}}}\, du \sim \sqrt{\frac{\pi}{2}}\frac{1}{\sqrt{N+1}} \tag{2.37}$$

when N is large. This has the same large N asymptotic scalings as the moments given in Eq.(2.24) when $\beta = 1$ and $x = 0$. Moreover, it is natural to anticipate a singularity in the PDF at $\xi = 1$, introduced by $\sqrt{1-\xi^2}$ in the denominator, since the initial PDF at $x = 0$ is a Dirac delta function $\delta(\xi - 1)$.

We next assume that $P_{x,t}(\xi)$ has the following formal series representation:

$$P_{x,t}(\xi) = \frac{\sum_{m=0}^{\infty} C_m T_m(\xi)}{\sqrt{1-\xi^2}} \tag{2.38}$$

where $T_m(x), m = 0, 1, \cdots$ is the m^{th} order Chebyshev polynomial of the first kind. As we will next see, this ansatz will lead to great simplification for the construction of the PDF. Again, Eq. (2.38) assumes a singularity at $\xi = 1$. In fact, in the absence of random advection ($\beta = \frac{a}{b'} = 0$), $P_{0,t}$ is nothing more than a Dirac delta function $\delta(\xi - 1)$, which is singular at 1. As β increases, the random drift causes non-vanishing probability for $\xi \neq 1$. But when a is "not too big", it is reasonable to assume that the singularity at $\xi = 1$ persists. For $x \neq 0$, this is still physically plausible because of the diffusive property of the equation. Indeed, with the exact PDF known in this case, the singularity is obvious from Eq.(2.5).

2.2.2 Obtaining the Expansion Coefficients via Extensions of the PDF

The Chebyshev polynomials are defined on $[-1, 1]$ whereas $P_{x,t}$ is on $[0, 1]$. We may easily extend $P_{x,t}$, evenly or oddly, to $[-1, 1]$, to make use of standard Chebyshev identities. Denote the extended PDF as $\widetilde{P}_{x,t}$. The coefficients C_n may then be computed directly in terms of the moments

$$M_n = \langle \xi^N \rangle_\gamma, \tag{2.39}$$

through the orthogonality of the Chebyshev polynomials, to wit:

$$\int_{-1}^{1} T_n(\xi) \widetilde{P}_{x,t}(\xi) d\xi = \int_{-1}^{1} \frac{\sum_{m=0}^{\infty} C_m T_m(\xi) T_n(\xi)}{\sqrt{1-\xi^2}} \, d\xi = C_n \, w_n \tag{2.40}$$

where w_n, the norm of $T_n(\xi)$ squared with weighting function $\frac{1}{\sqrt{1-\xi^2}}$, is π when $n=0$ and $\frac{\pi}{2}$ otherwise; at the same time

$$\begin{aligned}\int_{-1}^{1} T_n(\xi)\widetilde{P}_{x,t}(\xi)d\xi &= \int_{-1}^{1}\sum_{m=0}^{n} b_{nm}\xi^n \widetilde{P}_{x,t}(\xi)d\xi \\ &= \sum_{m=0}^{n} b_{nm}\int_{-1}^{1}\xi^n\widetilde{P}_{x,t}(\xi)d\xi \\ &= \sum_{m=0}^{n} b_{nm}\widetilde{M}_m\end{aligned} \tag{2.41}$$

where

- $B=\{b_{nm}\}_{n,m=0}^{\infty}$ is the transfer matrix from the monomial basis $\{\xi^n\}_{n=0}^{\infty}$ to the Chebyshev basis $\{T_n(\xi)\}_{n=0}^{\infty}$;
- $\widetilde{M}_m$ is the m^{th} moments of $\widetilde{P}_{x,t}$, namely, for even extension $\widetilde{M}_n = 2M_n$ if n is even and $\widetilde{M}_n = 0$ otherwise, and *vice versa* for odd extension.

Therefore, equating the right-hand-sides of Eq. (2.40) and (2.41), for even extension we have only the even-ordered terms survived in the series expansion (2.38), namely, $C_{2n-1}=0,\ n=1,2,\cdots$. Plugging in explicit formulas for b_{nm}(Abramowitz and Stegun, 1965) and $\widetilde{M}_m$, we have $C_0=\frac{2}{\pi}$ and

$$C_{2n} = \frac{\sum_{m=0}^{2n} b_{2n,m}\widetilde{M}_m}{w_{2n}} = \frac{(-1)^n n}{\pi}\sum_{m=0}^{n}\frac{(-1)^m\ 2^{2m+2}\ (n+m-1)!}{(n-m)!\ (2m)!}\frac{e^{-\frac{2mx^2}{2ma+b'}}}{\sqrt{1+2\beta m}} \tag{2.42}$$

for $n=1,2,\cdots$. Alternatively, we can invert the above formula (see Appendix for details) to get

$$M_{2n} = \frac{4^{n-1}\Gamma^2(n)}{\pi\Gamma(2n)}\sum_{m=0}^{n} C_{2m}\ \bar{w}_{2m}, \quad n=1,2,\cdots \tag{2.43}$$

with $\bar{w}_m=1$ if $m=0$ and $\bar{w}_m=2$ otherwise. This is a finite sum and it suggests that for any fixed $N>0$, the $2N$-term truncation of the series (2.38) with coefficients $C_m, m=0,1,\cdots,2N-1$ defined above will generate the first N even moments identical to those of the true PDF. Furthermore, utilizing (2.24) and the asymptotic property of Gamma functions(Abramowitz and Stegun, 1965), if we define $C_{2N}=\sqrt{\pi/(2\beta)}e^{-\frac{x^2}{a}} - \sum_{m=1}^{N-1} C_{2m} - \frac{1}{2}C_0$, the resulting $(2N+1)$-term truncation will have large even moments

M_{2n}^a asymptotically equal to the true moments M_{2n} as $n \to \infty$, since

$$M_{2n}^a = \frac{4^{n-1}\Gamma^2(n)}{\pi\Gamma(2n)} \sum_{m=0}^{N} C_{2m}\, \bar{w}_{2m} = \frac{2^{2n-1}\Gamma^2(n)}{\Gamma(2n)\sqrt{2\pi\beta}}\, e^{-\frac{x^2}{a}} \sim \frac{e^{-\frac{x^2}{a}}}{\sqrt{2\beta n}} \sim M_{2n}, \quad n \to \infty. \tag{2.44}$$

It may seem unusual that we are able to reconstruct the measure using only half of the moments, namely, even or odd. However, this is justified through the *Müntz-Szasz Theorem*(Rudin, 1987), which guarantees us that the expansion of $P_{x,t}(\xi)$ using only the Chebyshev polynomials with even powers in Eq. (2.38) is unique and it assumes pointwise convergence on $[0,1]$, if $\sqrt{1-\xi^2}P_{x,t}(\xi) \in \mathcal{C}[0,1]$. Essentially, it is because the expansion can be re-written as a linear combination of $\{x^{\lambda_i}\}_{i=0}^{\infty}$, where $\lambda_i = 2i$ which satisfies

$$\sum_{i=0}^{\infty} \frac{1}{\lambda_i} = \infty. \tag{2.45}$$

Thus, these polynomials are dense in $\mathcal{C}[0,1]$ and can be extended to $\mathcal{C}[-1,1]$ without any complication. This is also true for the odd extension case, except that we have to assume $P_{x,t}(0) = 0$ such that $\sqrt{1-\xi^2}\ P_{x,t}(\xi)$ is continuous at $\xi = 0$ to apply the result. However, this assumption may be false for some values of x and β. Recall the exact PDF (2.5) and the fact $P_{x,t}(0) := \lim_{\xi \to 0^+} P_{x,t}(\xi)$, Table 2.1 summarizes the values of $P_{x,t}(0)$ for different x's and β's and whenever $P_{x,t}(0) = \infty$, the expansion is not convergent at $\xi = 0$, since in such cases $\sqrt{1-\xi^2}P_{x,t}(\xi) \notin \mathcal{C}[0,1]$. This leads to the next discussion on the role $\sqrt{1-\xi^2}$ is playing.

$P_{x,t}(0)$	$x = 0$	$x \neq 0$
$\beta < 1$	0	0
$\beta = 1$	0	∞
$\beta > 1$	∞	∞

Table 2.1: $P_{x,t}(0)$ for Different x's and β's

2.2.3 Regularization Function

It is known that any continuous function on $[-1,1]$ can be expanded as a pointwise convergent series with Chebyshev polynomials(Mason and Weitz, 1995). And from Eq.(2.38) and (2.40), it is clear that we are essentially expanding the function $f(\xi) = \sqrt{1-\xi^2}P_{x,t}(\xi)$. However, Table 2.1 suggests that the series does not always converge pointwise, since $f(0)$ may diverge. This is not surprising from the exact formula of

the PDF (2.5) because $f(\xi)$ can be discontinuous at $\xi = 0$ when $\beta > 1$ or $x \neq 0$. As we will see in the next section, this will lead to the failure of the numerical series reconstruction, as the sum of polynomials diverges at the singularities.

Now we see that, if we can find a proper *regularization function* $r(\xi)$ such that $f(\xi) = r(\xi)\widetilde{P}_{x,t}(\xi)$ belongs to, or can be extended continuously to $\mathcal{C}[-1, 1]$, its series expansion will assume pointwise convergence in $[-1, 1]$, whose coefficients should still be computed from the statistical moments, namely,

$$f_n w_n = \int_{-1}^{1} f\ Q_n\ w\ d\xi = \int_{-1}^{1} r\ \widetilde{P}\ Q_n\ w\ d\xi = \int_{-1}^{1} \xi^k\ \widetilde{P}\ Q_n\ d\xi = \sum_{m=0}^{n} b_{nm}\widetilde{M}_{m+k} \quad (2.46)$$

in which k is a non-negative integer and $f,\ Q_n,\ w,\ r$ and $\widetilde{P}$ are all functions of ξ. For example, in the previous discussion, $r(\xi)$ was taken to be $1/w(\xi) = \sqrt{1-\xi^2}$. Consequently, $k = 0$ in Eq.(2.46) and we recover the formula for $f_n = C_n$ shown in Eq.(2.41). It can be verified that this leads to $f(0) = \infty$; while for $r(\xi) = \xi\sqrt{1-\xi^2}$, $f(0) = 0$ for any x and β, yet it still allows us to compute the coefficients in the series using statistical moments by making $r(\xi)w(\xi) = \xi$ and thus $k = 1$ in Eq.(2.46).

Moreover, the extensions for the PDF can be avoided by using alternative families of orthogonal polynomials for different $r(\xi)$, then the interval $[-1, 1]$ can be replaced with $[0, 1]$. One of these families is the *shifted Chebyshev polynomials* of the first kind

$$T_n^*(\xi) = T_{2n}(\sqrt{\xi}), \quad n = 0, 1, 2, \cdots \quad (2.47)$$

for any $\xi \in [0, 1]$, and the corresponding weight function is

$$w^*(\xi) = 1/\sqrt{\xi(1-\xi)}. \quad (2.48)$$

The motivation of choosing this family is to capture the singularity at $\xi = 0$, which is smoothed out by extension if standard Chebyshev polynomials are used. A similar calculation as in Eq.(2.37) shows that they also yield the same large n asymptotic scaling for the moments. Further, if we re-define $r(\xi) = \sqrt{\xi^3(1-\xi)}$, Eq.(2.46) is then modified as

$$f_n w_n = \int_0^1 r(\xi)\ P(\xi)\ T_n^*(\xi)\ w^*(\xi)\ d\xi = \int_0^1 \xi\ P(\xi)\ Q_n(\xi)\ d\xi = \sum_{m=0}^{n} b_{nm} M_{m+1}. \quad (2.49)$$

It is not hard to show that $f(\xi) = \sqrt{\xi^3(1-\xi)}\ P(\xi)$ for any probability measure P

singular at 0 can be extended continuously to $\mathcal{C}[0,1]$ and the series expansion converges pointwise for any x and β, from the integrability of P. Consequently the coefficients in the ansatz (2.8) with $Q_n(\xi) = T_n^*(\xi)$ is obtained by similar calculations as in Eq.(2.40) through (2.42) which read

$$C_n w_n = \sum\nolimits_{m=0}^{n} b_{nm} M_{m+1} \tag{2.50}$$

where again, M is the statistical moment, $\{b_{nm}\}_{n,m=0}^{\infty}$ is the transfer matrix and w_n is the normalization constant. Notice that $M_0 = 1$ is not present in the computation. In the next section, some examples show how this orthogonal basis improves the reconstruction.

Further, this idea can potentially be generalized to any PDF without *a priori* knowledge of its singular structure other than the locations of the singularities, since one can always choose the regularization function to be the product between the weight function of the orthogonal basis, $w(\xi)$, and $\prod_{i=1}^{N}(\xi - \xi_i^*)$, in which $\xi_i^*, i = 1, \cdots, N$ are the points where $P(s_i)$ diverges, to meet the requirements of 1) the convergence of the series expansion and 2) the computability of the coefficients from the moments. However, one does need to identify ξ_i^* before the expansion, either from physical or mathematical considerations, which we have mentioned in Section 2.2.1 and we will revisit this in Section 2.4.4. Notice that even if $P(\xi^*) < \infty$ for some ξ^*, it is clear that the series expansion still converges and we can still extract the correct PDF. Thus, we can remove all the possible singularities for series expansion to guarantee the convergence.

2.2.4 Large-n Asymptotics of the Coefficients C_n

Of course, the choice of polynomial family is not restricted to Chebyshev polynomials. For example, we can also re-define $r(\xi) = \xi(1-\xi)$ and use Legendre polynomials for reconstruction. Nonetheless, a Chebyshev basis does allow us to have a rigorous estimate of the remainder of the series, by applying the *method of steepest descent* to study the asymptotic behavior of the coefficients C_n for n large. For $Q_n(\xi) = T_n(\xi)$, we can explicitly compute

$$C_{2n} = 2Re[\int_0^{\frac{\pi}{2}} e^{i2n\theta} \sin\theta \, \frac{e^{-\frac{x^2}{a}} \, (\cos\theta)^{\frac{1}{\beta}-1} \, \cosh\sqrt{-\frac{4b'x^2}{a^2}\ln(\cos\theta)}}{\sqrt{-\beta\pi\ln(\cos\theta)}} \, d\theta] \tag{2.51}$$

and $C_{2n+1} = 0$ for $n = 0, 1, 2, \cdots$, utilizing the fundamental property of Chebyshev polynomials, $T_n(\xi) = \cos(n\theta)$ where $\theta = \cos^{-1}(\xi)$. And the large n asymptotics of C_{2n} is revealed through evaluating the integral of the complex function

$$I(z) = e^{i2nz} \sin z \, \frac{e^{-\frac{x^2}{a}} \, (\cos z)^{\frac{1}{\beta}-1} \, \cosh \sqrt{-\frac{4b'x^2}{a^2} \ln(\cos z)}}{\sqrt{-\beta\pi \ln(\cos z)}} \tag{2.52}$$

on the contour $\mathcal{C}_1 \bigcup \mathcal{C}_2 \bigcup \mathcal{C}_3$ in the complex $z-$plane where

$$\begin{aligned} \mathcal{C}_1 &= \{z = iy, 0 \le y \le T\}, \\ \mathcal{C}_2 &= \{z = x + iT, 0 \le x \le \frac{\pi}{2}\}, \\ \mathcal{C}_3 &= \{z = \frac{\pi}{2} + iy, T \ge y \ge 0\} \end{aligned} \tag{2.53}$$

and sending T to infinity. This contour is the steepest-decent curve that connects $z = 0$ and $z = \frac{\pi}{2}$. The detailed analysis for $I(z)$ will be shown in Appendix, which suggests that for large n, $|C_{2n}|$ is asymptotically proportional to

$$\cosh\left(\frac{2x\sqrt{b'}}{a}\sqrt{\ln n}\right) \, n^{-\frac{1}{\beta}} (\ln n)^{-\alpha} \tag{2.54}$$

where $\alpha = \frac{1}{2}, 1$ or $\frac{3}{2}$ depending on different values of x and β, which is shown in the Appendix. As a result, $\sum_{n=0}^{\infty} |C_n|$ converges for $\beta < 1$ for $x \neq 0$ and for $\beta \le 1$ when $x = 0$. And this serves as the criterion for the pointwise, uniform convergence of the series expansion for $f(\xi) = \sqrt{1-\xi^2} P_{x,t}(\xi) = \sum_{n=0}^{\infty} C_{2n} T_{2n}$ in $[0, 1]$, due to the boundedness of Chebyshev polynomials in this interval. For $x = 0$ and $\beta = 1$, Figure 2.1 shows that when $n > 500$, C_{2n} is almost identical to its asymptotic approximation.

It is also worth looking at the asymptotic behavior of C_{2n} in the cases where $\beta > 1$. Figure 2.2 shows such behavior for a series of β values approaching 1 from above, compared to the curve n^{-1}. It is known that for the series $\sum_{n=1}^{\infty} n^{-s}$, $s > 1$ will lead to convergence. Thus, if $|C_{2n}|$ decays faster than n^{-1} up to a scaling factor, we will see below that the series expansion assumes pointwise convergence for $\xi \in [0, 1)$. For the case where $\beta = 1$ as shown in Figure 2.1, it can be computed numerically that $|C_{2n}| \approx D \, n^{-1.14}$ for n large where D is a constant.

The figure indicates that for $\beta = 1.2,\ 1.1,$ and 1.075, $|C_{2n}|$ decays faster than $D_\beta n^{-1}$ for $n < N_\beta$ where D_β and N_β are constants determined by β. But eventually, $|C_{2n}|$ decays slower than $D_\beta n^{-1}$ (the curve of $|C_{2n}|$ will intersects with that of $n^{(} - 1)$),

meaning that $\sum_0^\infty |C_{2n}|$ diverges. For $\beta = 1.05$, we only compute $|C_{2n}|$ for $n \leq 5000$ due to numerical considerations, but the asymptotic analysis above implies that it will ultimately exhibit the same divergent behavior of $\sum_0^\infty |C_{2n}|$.

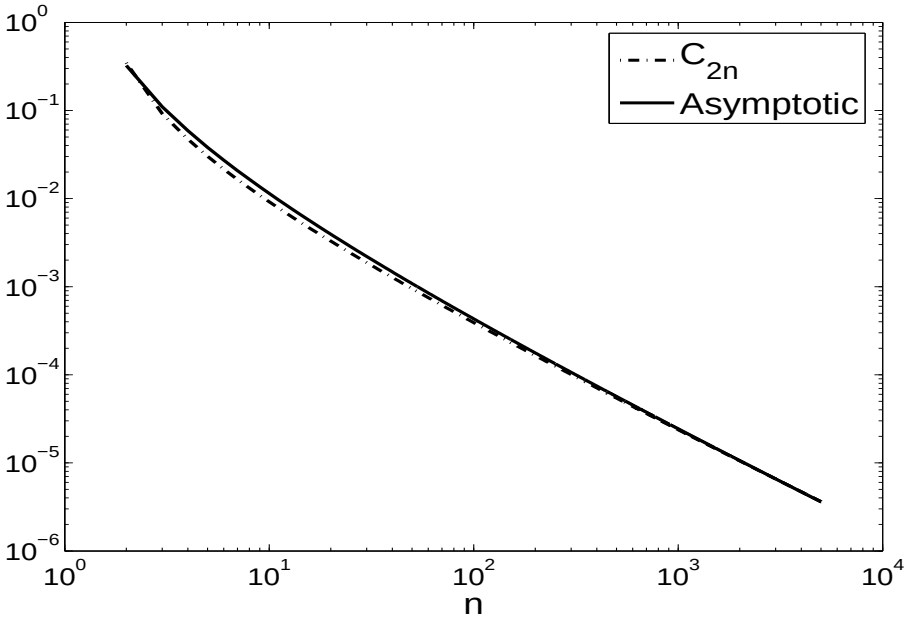

Figure 2.1: C_{2n} and Its Asymptotic Approximation for $x = 0$ and $\beta = 1$.

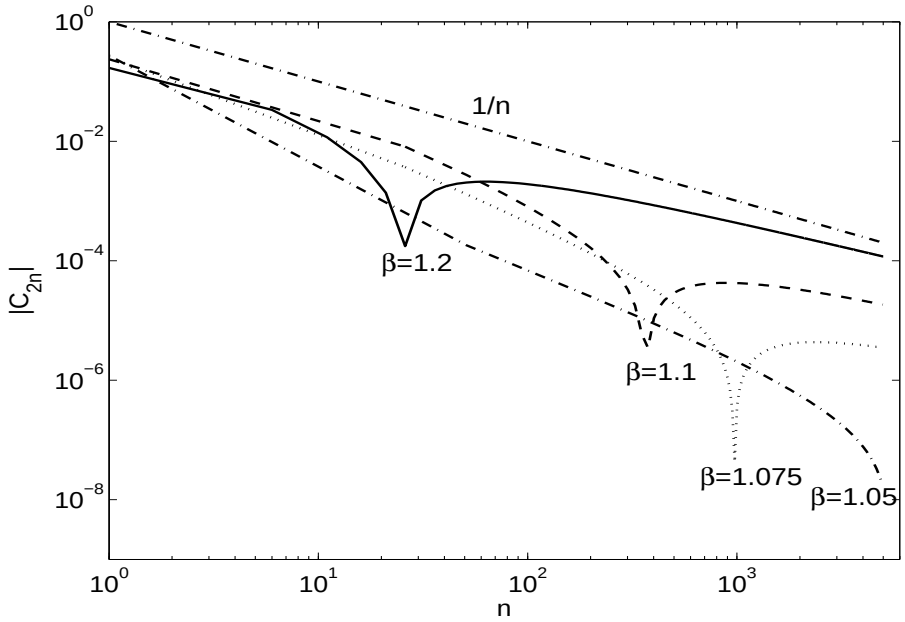

Figure 2.2: Asymptotic Behavior of $|C_{2n}|$ When $\beta > 1$

Consequently, the results (2.54) serves as a sufficient condition for the pointwise convergence of the series reconstruction. For example, when $Q_n(\xi) = T_n(\xi)$,

$$\begin{aligned}
\Big|\widetilde{P}(\xi) - \frac{\sum_{n=0}^{N-1} C_n\, T_n(\xi)}{\sqrt{1-\xi^2}}\Big| &= \Big|\int_{-1}^{1} \frac{\sum_{n=0}^{\infty} T_n(y)\, T_n(\xi)}{\sqrt{1-\xi^2}}\, \widetilde{P}(y)dy \\
&\quad - \int_{-1}^{1} \frac{\sum_{n=0}^{N-1} T_n(y)\, T_n(\xi)}{\sqrt{1-\xi^2}}\, \widetilde{P}(y)dy\Big| \\
&= \Big|\int_{-1}^{1} \frac{\sum_{n=N}^{\infty} T_n(y)\, T_n(\xi)}{\sqrt{1-\xi^2}}\, \widetilde{P}(y)dy\Big| \\
&= \lim_{P\to\infty}\left|\frac{\sum_{n=N}^{N+P} C_n w_n T_n(\xi)}{\sqrt{1-\xi^2}}\right| \\
&\le M\sum_{n=N}^{\infty}|C_n|
\end{aligned} \tag{2.55}$$

for any $\xi \in [0,1)$ noticing the fact that $\frac{\sum_{n=0}^{\infty} T_n(y)\, T_n(\xi)}{\sqrt{1-\xi^2}} = \delta(y)$.

Since we have established the condition for the convergence of $\sum_{n=0}^{\infty}|C_n|$ in the formula (2.54), the same condition will imply

$$\frac{\sum_{n=0}^{N-1} C_n\, Q_n(\xi)}{r(\xi)} \to P(\xi) \tag{2.56}$$

as $N \to \infty$, for any $\xi \in [0,1)$.

Furthermore, from the relationship (2.34) between the Péclet number $\mathrm{Pe} = \frac{\sigma^2}{\kappa}$ and β, and the fact that β is an increasing function of time for fixed σ and κ, we conclude that $\mathrm{Pe} = 2$ is the critical value that distinguishes the pointwise convergence of the series reconstruction via the standard Chebyshev polynomials at all times. However, it can be easily verified that with the shifted Chebyshev polynomials, the series expansion converges for arbitrary (x,t) and Pe, by simply replacing $\frac{1}{\beta}$ with $\frac{1}{\beta}+1$ in (2.54).

2.3 Numerical Results of Series Reconstruction

2.3.1 Reconstruction via Extension to $[-1, 1]$ for $T_0(x) = e^{-x^2}$

First we carried out the reconstruction for the PDF (2.5) using series approximants

$$P_{x,t}(\xi) \approx \frac{\sum_{n=0}^{N-1} C_{2n} T_{2n}(\xi)}{\sqrt{1-\xi^2}} \tag{2.57}$$

by evenly extending it to $[-1, 1]$. The numerical results are illustrated in Figure 2.3, which compares the exact PDF (solid line) with its series reconstruction (dashed line) obtained by setting $N = 4$ in (2.57) (first 4 even moments are used). Four reconstructions are done at $t = 1$ for different x and Pe values. We note that the similar case with an odd extension yields a nearly identical comparison.

The reconstructions in the upper two panels, in which $x = 0$ and $\mathrm{Pe} \leq 2$, agree with the exact PDF with error near the singularity $\xi = 1$, respectively; while the two in the lower panels, in which $x \neq 0, \mathrm{Pe} = 2$ or $x = 0, \mathrm{Pe} > 2$, fail to recover the true distributions almost everywhere. Recall that the series reconstruction is expected to fail whenever $P_{x,t}(0) = \infty$, since the truncated series (2.57) is always smooth at $\xi = 0$.

Does an increasing N help reducing the error? The answer is no. In the left panel of Figure 2.4, we increase N to 40 and compare the series reconstruction using the standard Chebyshev polynomials to the exact PDF for $x = 2$, $t = 1$ and $\mathrm{Pe} = 4$. We can see the rapid oscillations near $\xi = 0$, which is a characteristic of high order polynomials in a finite interval, let alone the fact that to obtain the coefficients about 40 significant digits are required for accurate summation of Eq.(2.42). But an alternative polynomial family can improve the reconstruction. In the right panel, we reconstruct the PDF via shifted Chebyshev polynomials and re-define $r(\xi) = \sqrt{\xi^3(1-\xi)}$. Now only 4 terms are needed to approximate $P_{x,t}(\xi)$ with negligible error. We will discuss how and why alternative choices of $r(\xi)$ and the polynomial family improve the reconstruction later in this section.

Figure 2.5 further shows the slow convergence rate of the reconstructions with increasing N, the number of terms used in the series (2.57), although when $x = 0$, $\beta \leq 1$, the relative errors are much smaller (less than 1% when $N = 4$). Here the relative error

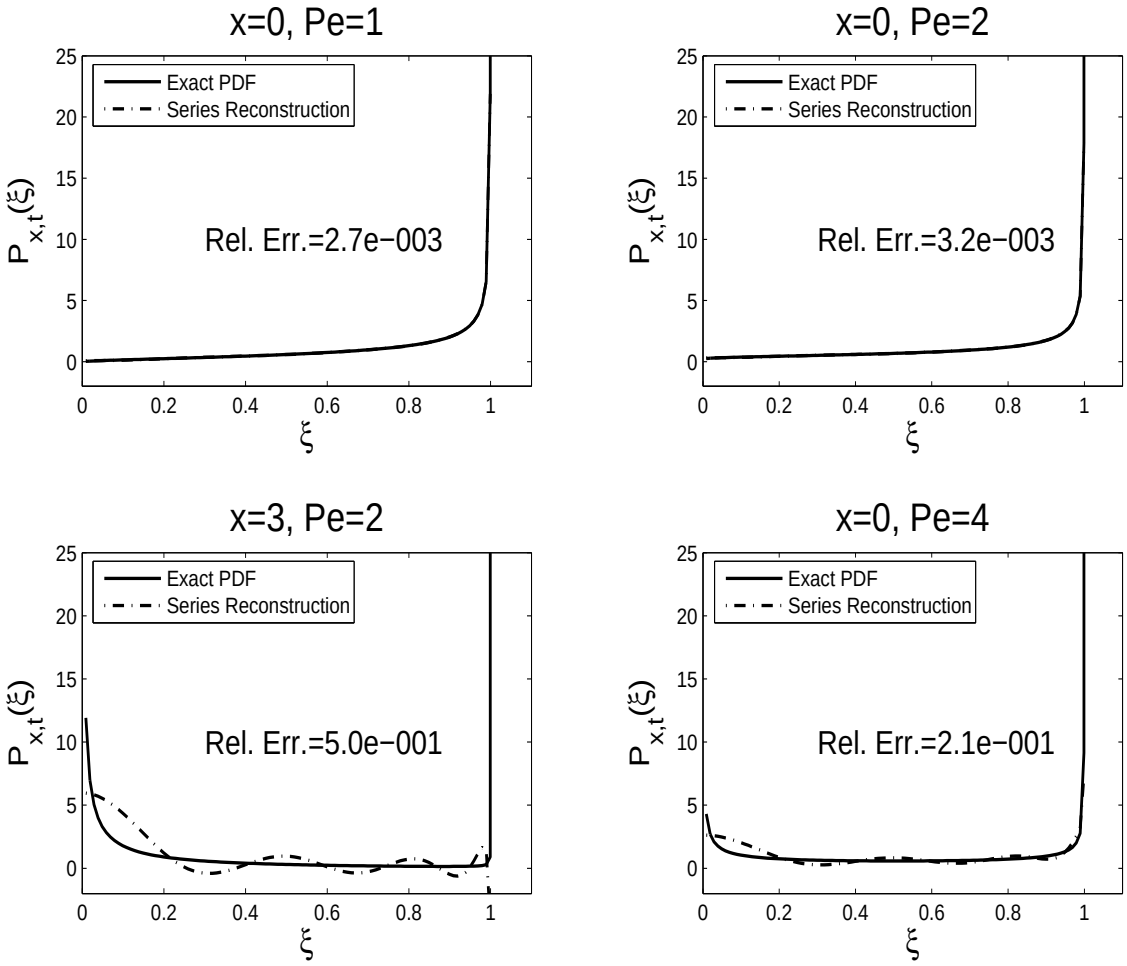

Figure 2.3: 4-Term Chebyshev Reconstructions of the PDF at $t = 1$

is defined by

$$\varepsilon_N = \frac{\| P_{x,t}(\xi) - \frac{\sum_{n=0}^{N-1} C_{2n} T_{2n}(\xi)}{\sqrt{1-\xi^2}} \|_2}{\| P_{x,t}(\xi) \|_2}. \tag{2.58}$$

2.3.2 Improving Series Reconstruction

Let us see how alternative choices of $r(\xi)$ and the polynomial family improve the reconstruction. Letting $r(\xi) = \sqrt{\xi^3(1-\xi)}$ and $Q_n(\xi) = T_n^*(\xi)$ as discussed in Section 2.2.3, we can reconstruct the PDF with only 4 terms (first 4 moments are used), to achieve a relative error less than 1%, which is shown in Figure 2.6, in contrast to the lower two panels in Figure 2.3. The negligible errors suggest that the performance of

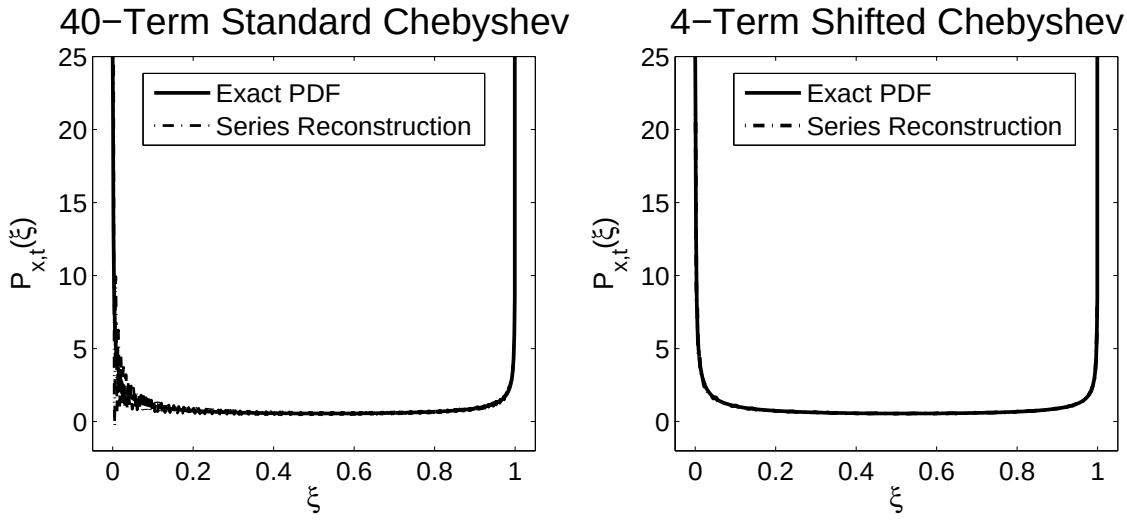

Figure 2.4: Reconstructions of the PDF at $t = 1$ via Different Orthogonal Polynomials

the series reconstruction relies on the capability of $(r(\xi))^{-1}$ to recover the singularities in $P_{x,t}(\xi)$, since the numerator in (2.57) is always continuous in $[0, 1]$. For example, when $x \neq 0$ and $\beta \geq 1$, we know from (2.5) and Table 2.1 that $P_{x,t}(0) = P_{x,t}(1) = \infty$. Therefore $[r(\xi)]^{-1} = [\xi\sqrt{(1-\xi^2)}]^{-1}$, which has two singularities at $\xi = 0$ and 1, should be adopted instead of $[r(\xi)]^{-1} = [\sqrt{(1-\xi^2)}]^{-1}$. Of course, $r(\xi)$ should be defined in such a way that $r(\xi)w(\xi) = \xi^k$ where k is an non-negative integer and thus the coefficients can be computed using statistical moments as shown in (2.46). Figure 2.7 is a comparison between the convergence rates of reconstructing the same PDF using the following three different combinations of $r(\xi)$ and Q_n, each of which corresponds to one curve in either panel

1. Shifted Legendre polynomials defined on $[0, 1]$ and $r(\xi) = \xi(1-\xi)$;
2. Shifted Chebyshev polynomials defined on $[0, 1]$ and $r(\xi) = \sqrt{\xi^3(1-\xi)}$;
3. Standard Chebyshev polynomials defined on $[-1, 1]$ and $r(\xi) = \xi\sqrt{1-\xi^2}$.

In the left panel of Figure 2.7, $x = 3$, Pe $= 2$ and $t = 1$, so $P_{x,t}(0) = P_{x,t}(1) = \infty$; whereas on the right, $x = 0$, Pe $= 2$ and $t = 1$, so $P_{x,t}(0) = 0$, $P_{x,t}(1) = \infty$. Notice that the number of singularities in $[r(\xi)]^{-1}$ is greater than (right) or equal to (left) that of the exact PDF (2.5) for all three choices. For both PDF's, shifted Chebyshev polynomials give the optimal results, with relative errors of $\sim 1\%$ when only 8 moments are used. It should also be noted that when we under-estimate the number of singularities, the reconstructions from any of the three polynomial families converges very slowly. This is not surprising because as we mentioned in Section 2.2.2, $f(\xi^*) = r(\xi^*)P_{x,t}(\xi^*) = \infty$

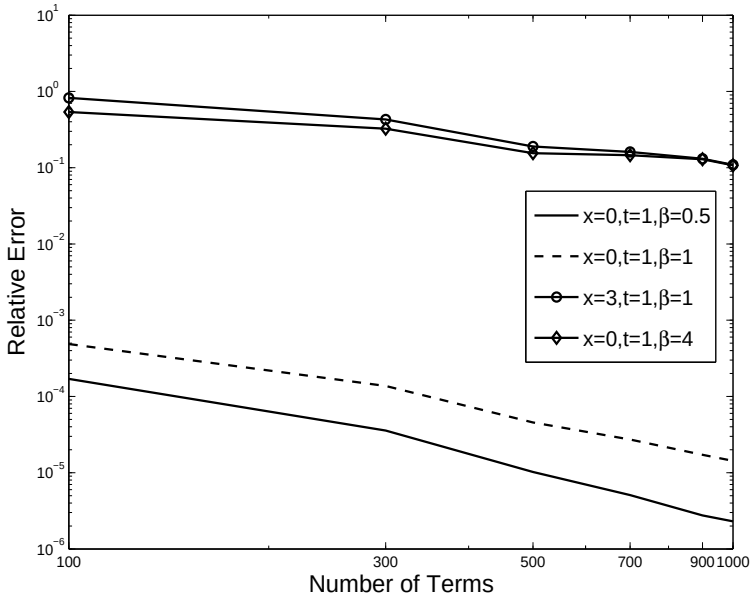

Figure 2.5: Relative Errors of Series Reconstructions VS Number of Terms Kept in (2.57)

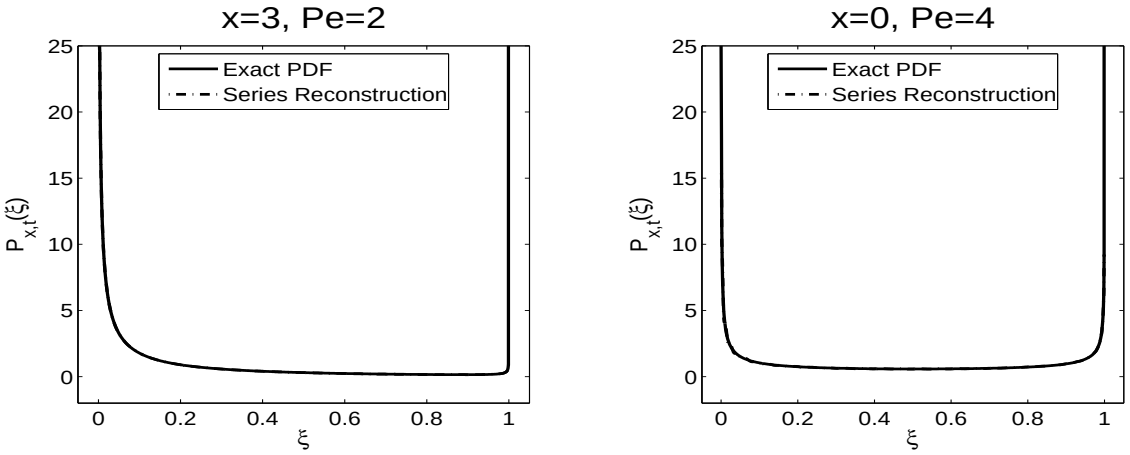

Figure 2.6: 4-Term Shifted Chebyshev Reconstructions of the PDF at $t = 1$

for some $\xi^* \in [0, 1]$ when this occurs.

Figure 2.7 also shows that even when the correct singularities are built into $r(\xi)$, the reconstructions using standard Chebyshev polynomials via extension converges much more slowly than those without extension. Other than the fact that different regularization functions are used here, extensions should be avoided if possible since they may introduce non-smoothness of $f(\xi)$ at the interior point $\xi = 0$ which can affect the convergence rate. More detailed quantitative analysis on this will be addressed in our future work.

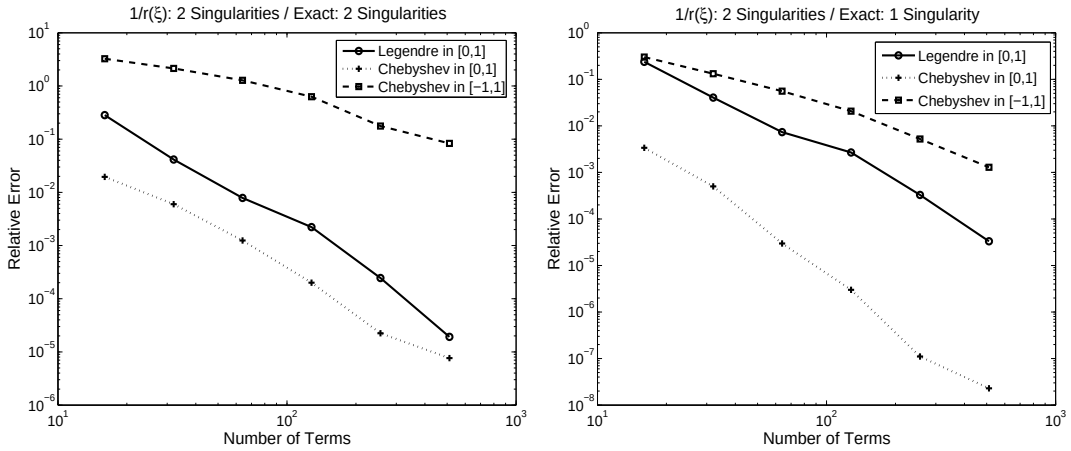

Figure 2.7: Convergence Rates for Different $r(\xi)$ and $Q_n(\xi)$

2.4 Monte-Carlo Simulations and PDF Dynamics

The purpose of this section is to study the effectiveness of Monte-Carlo methods applied in the problem (3.1), when the exact PDF for the tracer is known at all times. The Monte-Carlo simulation for Eq.(3.1) is straightforward by spectral methods, along with a simple random number generator. Moreover, at a fixed time t, the Monte-Carlo simulation for the tracer can be made easier by sampling $W(t)$ from a mean-zero Gaussian random variable with variance $\sigma^2 t$ from the scaling property of Wiener Processes. Nonetheless, to study the full temporal evolution of $P_{x,t}(\xi)$, one has to simulate the complete Wiener path $W(t)$, which is discretized as a sum of independent Gaussian random variables using standard techniques(Gardiner, 1985), namely, $W(t) \simeq \sum_{i=0}^{N} dw_i$ where $dw_i \sim \mathcal{N}(0, \sigma^2 \Delta t_i)$.

For general stochastic flows and initial data, the analytic solution to the random advection-diffusion problem is not available as well as the exact scalar PDF. Monte-Carlo simulation is a powerful numerical tool to approximate the PDF and investigate its dynamics in such cases. Moreover, accurate Monte-Carlo simulations can be used to benchmark the performance of the PDF reconstructions via orthogonal polynomials discussed in the previous sections.

2.4.1 Uni-Modal Positive, Gaussian Initial Data $T_0(x) = e^{-x^2}$

We will first examine the case with the initial data $T_0(x) = e^{-x^2}$, for which we have the exact PDF (2.5) and exact moments (2.24) to evaluate the Monte-Carlo simulations. As we will see, the simulation does give an accurate approximation to the exact PDF

and recover its spatio-temporal dynamics with a certain number of realizations.

Monte-Carlo Simulations

Figure 2.8 depicts the spatial structure of $P_{x,t}(\xi)$ obtained by two different approaches: exact formula (2.5) and Monte-Carlo simulations. Here Pe $= 2$ and $t = 1$. To obtain each histogram to simulate $P_{x,t=1}(\xi)$, 10^5 samples are drawn by the Monte-Carlo simulator and 100 bins are distributed uniformly between $[0, 1]$. Each panel is a snapshot of $P_{x,t}(\xi)$, exact on the left and Monte-Carlo simulated on the right, at time $t = 1$. The horizontal axis is the renormalized scalar ξ-axis, ranging from 0 to 1, and the vertical axis is the spatial x-axis between $[-5, 5]$. The grayscale ramp is set uniformly between $[0, 2]$ such that regions where $P_{x,t}(\xi) \approx 0$ are dark blue, whereas dark red regions implies $P_{x,t}(\xi) \gtrsim 2$. For example, if we take a horizontal slice of the left panel along $x = 3$, and interpret the brightness with corresponding numbers, we would recover the solid curve shown in the lower-left panel of Figure 2.3.

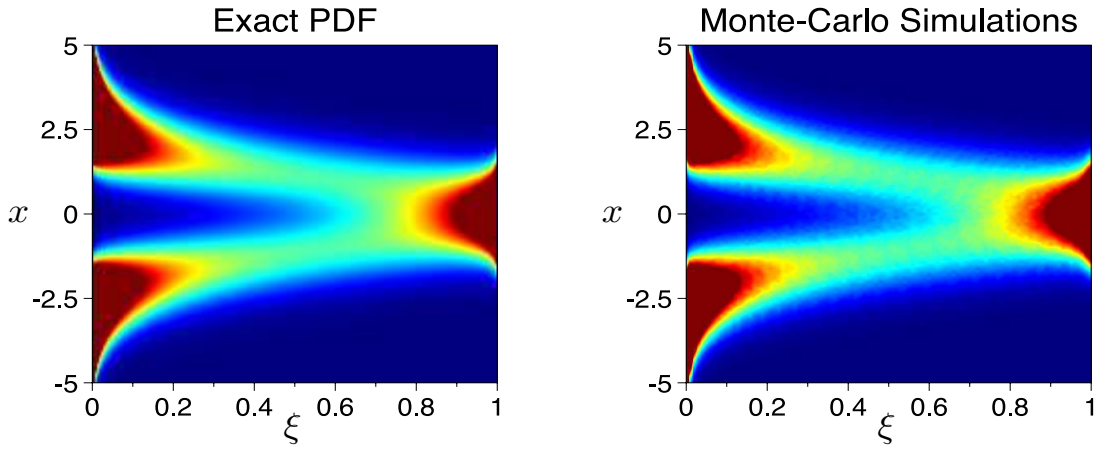

Figure 2.8: Comparison Between the Exact PDF (2.5) and MC Simulations. Horizontal Axis — Renormalized Tracer ξ. Vertical Axis — Spatial Variable x. *: Grayscale ramp uniformly set in [0,2], same in all other grayscale figures

The overall agreement between the Monte-Carlo simulations and the exact PDF is obvious from Figure 2.8. To benchmark quantitatively the performance of the Monte-Carlo simulator, we first compare the exact moments of the random variable ξ with the moments generated from the simulation histogram. A valid Monte-Carlo simulation should converge to the exact PDF as the numbers of realizations increases. Figure 2.9 is the summary of the two tests mentioned above, where $x = 2$, $\beta = 1$, $t = 1$ and 100 bins are used to construct the histograms. The relative error plotted in the right

panel is defined similarly to Eq.(2.58) by replacing the series reconstruction with the simulated histogram.

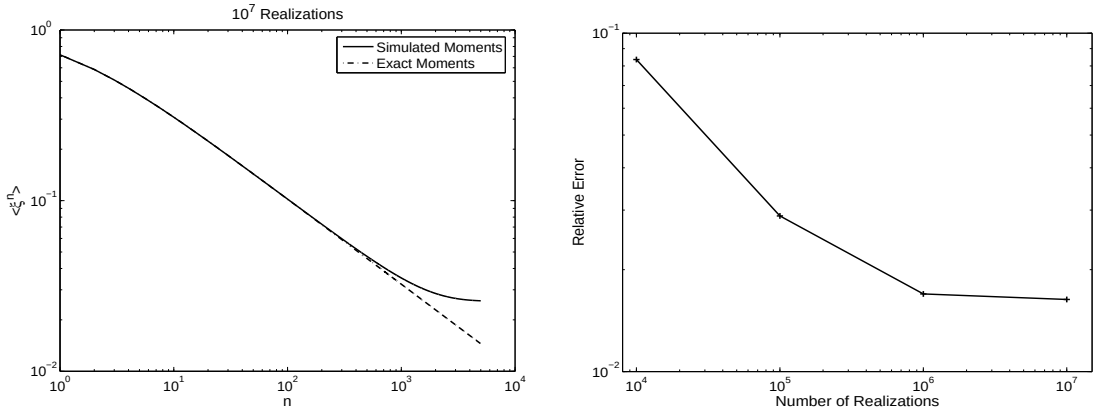

Figure 2.9: Benchmarking the Monte-Carlo Simulator. Left: Exact Moments VS Simulated Moments. Right: Relative Error in $P_{x,t}(\xi)$ VS Number of Realizations.

In the left panel, we can see that the simulated moments coincide with the exact moments for $n \lesssim 1000$. The right panel depicts the L^2 relative error which shows improved convergence with the number of realizations increasing from 10^4 to 10^7. With increasing M, the number of realizations, the relative error first decays like $\frac{1}{\sqrt{M}}$, while it remains almost the same for $M \geq 10^6$. We also find that the pointwise relative error is negligible ($\sim 0.1\%$) when $M \geq 10^5$ everywhere in $[0, 1]$ except near the singularity $\xi = 1$. This error saturation is however inevitable with any simulation approach because of the systematic bias introduced by discretization errors, the finite statistics, histogram binning, etc.

We next explore the decay of the pointwise, absolute error of the Monte-Carlo simulation with increasing number of realizations. Figure 2.10 shows the difference between $P_{0,10}(\xi)$ and its Monte-Carlo approximations. And we can see that with increasing number of realizations, the pointwise error vanishes except near $\xi = 1$, which is the singularity in $P_{0,10}(\xi)$. This is however inevitable with any Monte-Carlo approach since the finite statistics will not produce histograms with singularities, even with increasing number of realizations. This essentially explains the slow decay in the relative error shown in the right panel of Figure 2.9, for number of realizations greater than 10^5.

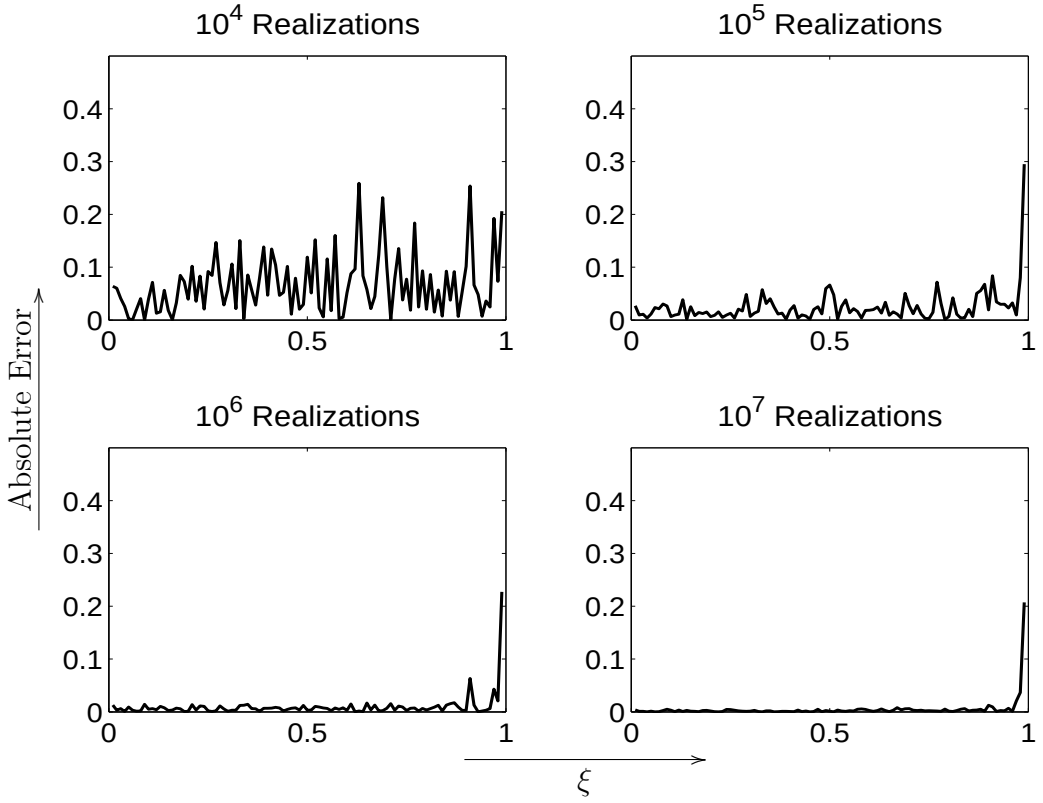

Figure 2.10: The Pointwise Error of the Monte-Carlo Simulated $P_{0,10}(\xi)$

Spatio-Temporal PDF Dynamics

We have seen that with 10^5 realizations (with L^2 relative error $\sim 1\%$), the Monte-Carlo simulation favorably reproduce measure, which serves as a tool to study more complicated PDF evolution for cases where the exact PDF is not available. As a test problem, first we present the dynamics associated with the exact PDF (2.5). For the deterministic heat equation, namely $\sigma = 0$, it is clear that $P_{x,t}(\xi) = \delta(\xi - e^{-x^2/b'})$ for any x and t, as we have seen in Section 2.1.5. But how does the random drift change the PDF dynamics? Figure 2.11 and 2.12 together offer a comprehensive illustration of the spatial-temporal structure of Monte-Carlo simulations of $P_{x,t}(\xi)$ when Pe = 2. In both figures, different panels, which are the counterparts of the right panel in Figure 2.8 at different times, form a time sequence showing the dynamical behavior of $P_{x,t}(\xi)$. Here replacing the Monte-Carlo simulations with the exact PDF will not change the dynamics at all since their relative difference is only about 1%.

Initially at $t = 0$, for any (ξ, x), $P_{x,t=0}(\xi) = \delta(\xi - e^{-x^2})$ since the initial data is deterministic. That is, $P_{x,t=0}(\xi) = 0$ except on the curve (e^{-x^2}, x), which is the rotated

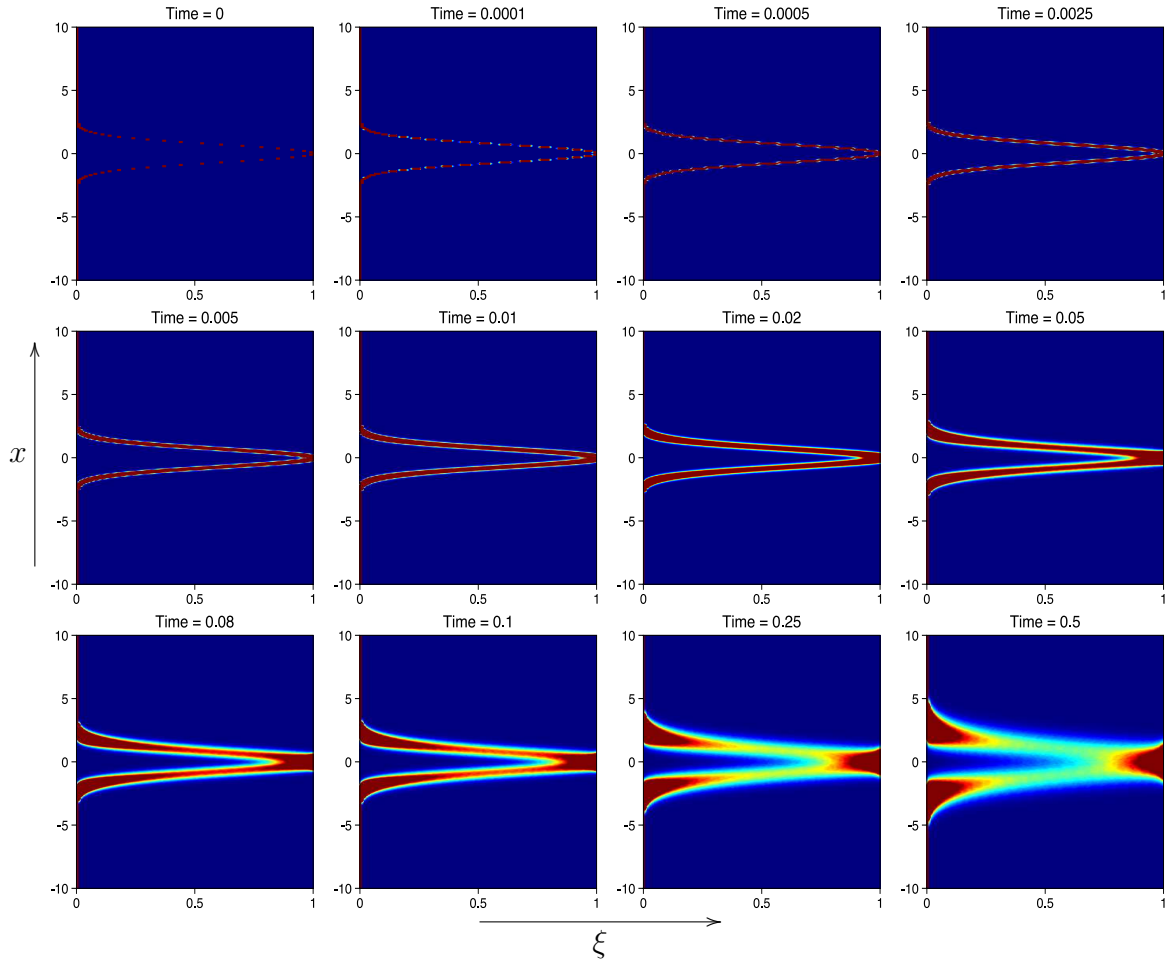

Figure 2.11: The Short Time Dynamics of $P_{x,t}(\xi)$: from Gaussian to Ribbons.

Gaussian in the top-left panel in Figure 2.11. Immediately after that, the random drift smears the deltas and we see a gray ribbon developing around the curve. Gradually, for any nonzero x, the majority of the probability will shift towards $\xi = 1$ since from Eq. (2.27), $P_{x,t}(\xi) \sim P_{0,t}(\xi)$ as $t \to \infty$, which has a singularity at $\xi = 1$. Moreover, from the panels $t = 0.08, 0.1, 0.25$ and 0.5 in Figure 2.11, we conclude that for those x's in the core of the Gaussian, the probability shifts faster than for those in the tails of the Gaussian. This explains the emergence of:

1. Two dark, red regions at the junctions between the core and the tails of the initial Gaussian when $t = 0.5$. For these x values, the singularity in the initial delta function slowly begins to disappear and the probability "smears" around these junctions.

2. Two gray ribbons around the core region of the initial Gaussian when $t = 0.5$, in

which the probability density is substantially greater than 0 (dark) but not very large (red). For any fixed x within this region, the transient measure Eq.(2.5) is drastically different from the initial measure $\delta(\xi - e^{-x^2})$ and is converging to its long time asymptotic limit Eq.(2.11).

3. A dark, red region near $(\xi = 1, x = 0)$, within which $P_{x,t}(\xi) \approx P_{0,t}(\xi)$.

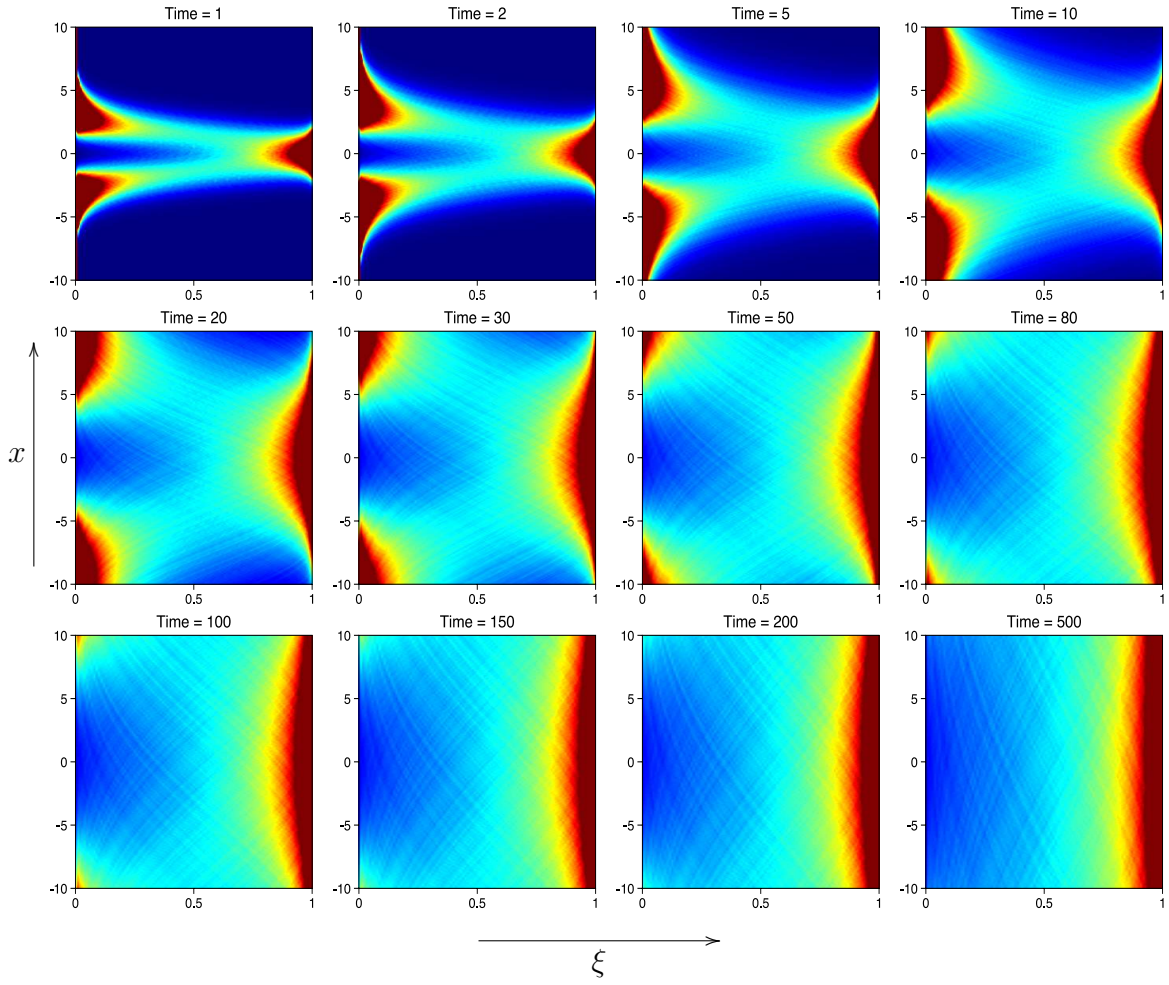

Figure 2.12: The Long Time Dynamics of $P_{x,t}(\xi)$: from Ribbons to Stripes.

The time series shown in Figure 2.11 continues in Figure 2.12. Notice that two high density regions near $\xi = 0$ "moves away" from the line $x = 0$ towards large $|x|$ values. Eventually when $t = 500$, the initial Gaussian disappears completely. For $|x| \leq 10$, the brightness is almost homogeneous in x direction and we see only vertical stripes. This agrees with Eq.(2.27), namely, $P_{x,t}(\xi)$ is uniform in x when $t \to \infty$. However, this argument should be valid only over compact sets, since if we extend the plotted portion

of x-axis, we will see the two dark, red regions again. In fact, this moving speed can be estimated here to be proportional to $1/\sqrt{t}$, which is ultimately attributed to the x^2/t self-similarity that we discussed in Section 2.1.3 and can be seen from Eq.(2.5). For general models with such behavior, one way to identify the speed is to find $|\tilde{x}|$ where $\tilde{x}$ maximizes $P_{x,t}(D)$ for some small number D as a function of t, which is approximately the $|x|$ value at the centers of the high density regions. At the spatial locations with larger $|x|$ values, $P_{x,t}(D)$ is smaller since the initial scalar profile concentrated near $x = 0$ has not yet arrived via diffusion. Thus the probability is confined in a very small interval with $\xi \ll D$, while for smaller $|x|$, $P_{x,t}(D)$ is also smaller since these locations are inside the core of the diffusing Gaussian and the probability accumulates near $\xi = 1$. Therefore, $\pm\ \tilde{x}$ can be regarded as the "fronts" of the averaged tracer concentration. Setting $D = 0.1$ and with time running from 1 to 10^6, we obtained Figure 2.13. The interpretation of the slope ~ 0.5 is that $\tilde{x}^2 \propto t$ and then the speed $d\tilde{x}/dt \propto 1/\sqrt{t}$. This confirms that the random solution (2.9) inherit the self-similarity from the pure heat equation. Essentially, for this simple random advection, the averaged tracer concentration is govern by a heat equation with an effective diffusivity computed by the Green-Kubo formula.

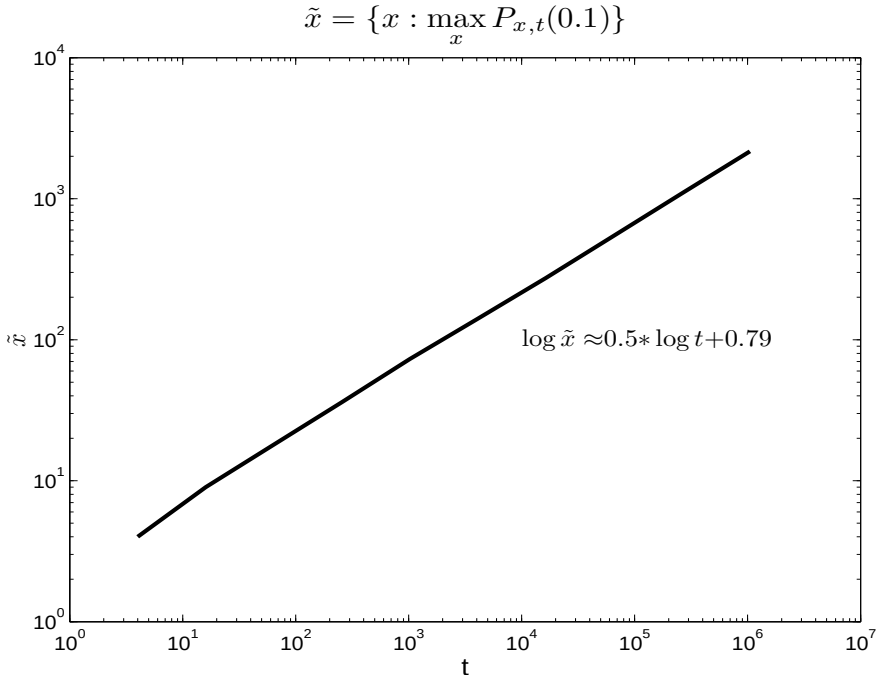

Figure 2.13: The $|x|$ Value at the "Information Fronts" of VS Time

Effects of the Péclet number

As we mentioned in Section 2.1.5, the Péclet number $\mathrm{Pe} = \frac{\sigma^2}{\kappa}$ dictates $P_{x,t}(\xi)$ at large times. Figure 2.14 demonstrates the spatio-temporal evolutions of $P_{x,t}(\xi)$ for different values of Pe. Recall that from Eq.(2.5), (2.27) and (2.34),

$$\lim_{t\to\infty} P_{x,t}(\xi) \;=\; \lim_{t\to\infty} P_{0,t}(\xi) \;=\; \frac{\sqrt{2}\,\xi^{\frac{2}{\mathrm{Pe}}-1}}{\sqrt{\mathrm{Pe}\,\pi\ln\xi}} \tag{2.59}$$

where Pe characterizes the competition between the random drift and the diffusion. This is manifested in the $t = 500$ panels, in which more and more density shifts from near $\xi = 1$ and accumulates near $\xi = 0$ with increasing Pe, although the short-time PDF behaviors when $t < 0.5$ are similar for these four Pe values. This shift in the PDF is attributed to the fact that the higher Pe is, the more turbulent the flow is and therefore the higher probability the scalar has to access far-field, small values.

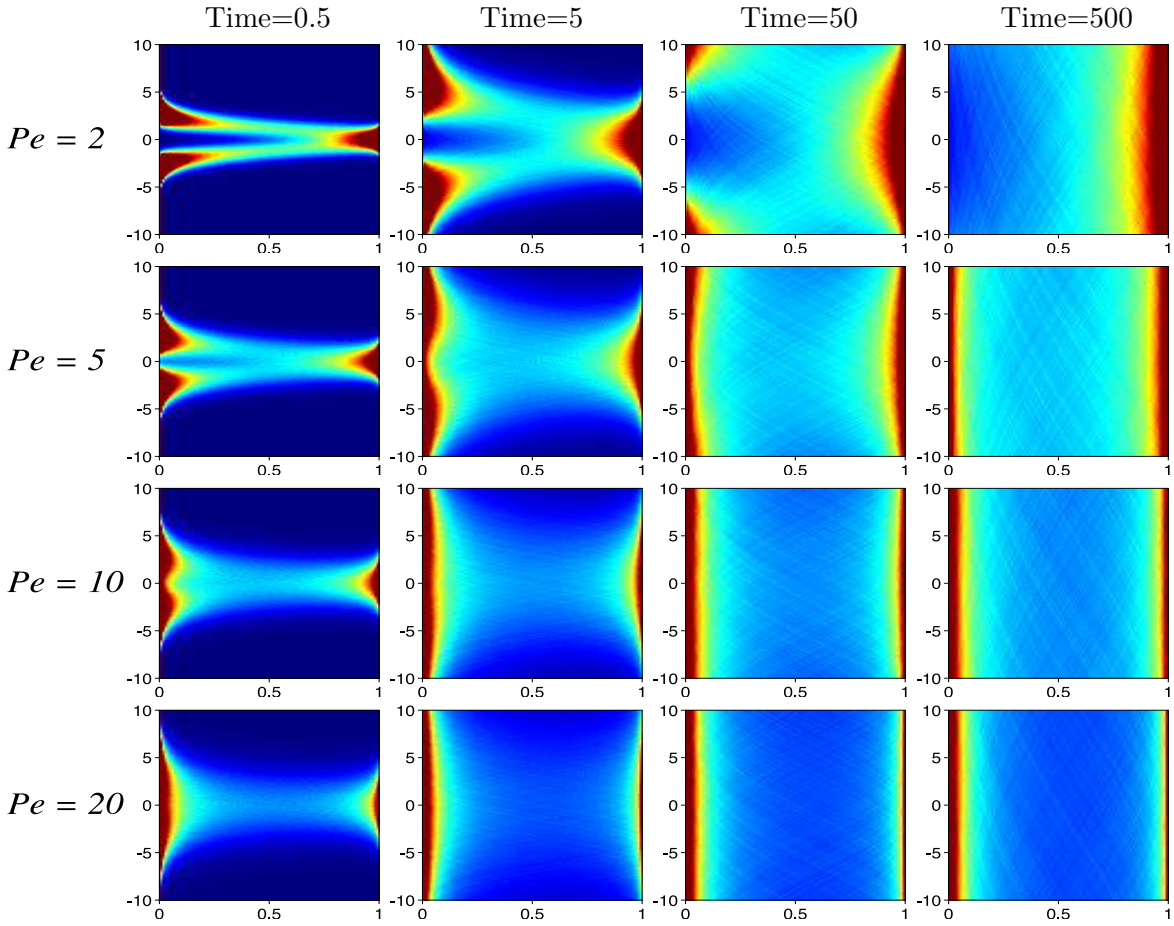

Figure 2.14: Effects of the Péclet number for $T_0(x) = e^{-x^2}$

2.4.2 Bimodal Initial Data $T_0(x) = 2xe^{-x^2}$

For this initial data, the general exact PDF solution is not available. However, we can still solve the linear, random advection-diffusion problem (3.1) analytically, by simply taking the spatial derivative of (2.9) and the exact solution for $T_0(x) = 2xe^{-x^2} = -\frac{d}{dx}e^{-x^2}$ reads

$$T(x,t) = \frac{2(x - W(t))}{(1+4\kappa t)^{\frac{3}{2}}} \exp\Big(- \frac{(x-W(t))^2}{1+4\kappa t}\Big). \tag{2.60}$$

which has two extrema (bimodal) in x-direction. Now we can re-define $T_{max}(t) = \frac{\sqrt{2\,e^{-1}}}{4\kappa t+1}$ such that the random variable $\xi = \frac{T(x,t)}{T_{max}(t)} \in [-1,1]$ and its exact statistical moments are

$$\langle T^N \rangle_\gamma = \Big(\frac{4a}{b'^2(aN+b')}\Big)^{\frac{N}{2}} \frac{e^{-\frac{Nx^2}{b'} + \frac{\beta N^2 x^2}{aN+b'}}}{\sqrt{\pi(1+\beta N)}} \sum_{\substack{j=0,\\ \text{j even}}}^{N} \binom{N}{j} \Big(\frac{x}{\sqrt{a(1+\beta N)}}\Big)^{N-j} \Gamma\Big(\frac{j+1}{2}\Big) \tag{2.61}$$

from similar calculations as in Eq. (2.21).

Although in this case, the exact PDF is not available by performing inverse Laplace transform as shown in Sec. 3.4, we are able to find the space-independent, limit distribution $P_\infty(\xi)$ as $t \to \infty$ as follows. First, the long time asymptotic moments are

$$\langle \xi^N \rangle_\gamma \sim \frac{1+(-1)^N}{2} \Big(\frac{e\ \mathrm{Pe}}{1+\mathrm{Pe}N/2}\Big)^{\frac{N}{2}} \frac{\Gamma(\frac{1+N}{2})}{\sqrt{\pi(1+\mathrm{Pe}N/2)}}. \tag{2.62}$$

Notice that this is not in the form of Eq.(2.27) because $\hat{T}_0(0) = 0$. These moments are reminiscent of formulas involving the Lambert W- or tree functions(Corless et al., 1997), which provides a generating function for the number of rooted trees on n points. Using this observation we have been able to explicitly compute the distribution in terms of the tree function as follows: If we define the functions $w_i(z),\ i = -1, 0$ for any $z \in [0,1]$ by

$$\begin{aligned} w_i(z)\ e^{1-w_i(z)} &= z, \\ w_{-1}(1) = w_0(1) &= 1, \\ w_0(0) = 0 \text{ and } w_{-1}(0) &= \infty, \end{aligned} \tag{2.63}$$

we have

$$
\begin{aligned}
&\frac{1}{\sqrt{e\pi\mathrm{Pe}}}\int_{-1}^{1}\xi^N\left(\frac{e^{\frac{\mathrm{Pe}-2}{2\mathrm{Pe}}w_0(\xi^2)}}{1-w_0(\xi^2)}-\frac{e^{\frac{\mathrm{Pe}-2}{2\mathrm{Pe}}w_{-1}(\xi^2)}}{1-w_{-1}(\xi^2)}\right)\,d\xi\\
=\;&\frac{1}{\sqrt{e\pi\mathrm{Pe}}}\Big(\int_{-1}^{1}\xi^N\frac{e^{\frac{\mathrm{Pe}-2}{2\mathrm{Pe}}w_0(\xi^2)}}{1-w_0(\xi^2)}\,d\xi-\int_{-1}^{1}\xi^N\frac{e^{\frac{\mathrm{Pe}-2}{2\mathrm{Pe}}w_{-1}(\xi^2)}}{1-w_{-1}(\xi^2)}\,d\xi\Big)\\
=\;&\frac{1+(-1)^N}{2\sqrt{e\pi\mathrm{Pe}}}\Big(\int_0^1 x^{\frac{N-1}{2}}\frac{e^{\frac{\mathrm{Pe}-2}{2\mathrm{Pe}}w_0(x)}}{1-w_0(x)}\,dx-\int_0^1 x^{\frac{N-1}{2}}\frac{e^{\frac{\mathrm{Pe}-2}{2\mathrm{Pe}}w_{-1}(x)}}{1-w_{-1}(x)}\,dx\Big)\\
=\;&\frac{1+(-1)^N}{2\sqrt{e\pi\mathrm{Pe}}}\int_0^\infty(w\,e^{1-w})^{\frac{n-1}{2}}\frac{e^{\frac{\mathrm{Pe}-2}{2\mathrm{Pe}}w}}{1-w}\,e^{1-w}(1-w)dw\\
=\;&\frac{1+(-1)^N}{2\sqrt{e\pi\mathrm{Pe}}}\int_0^\infty w^{\frac{N-1}{2}}e^{\frac{N+1}{2}(1-w)+\frac{\mathrm{Pe}-2}{2\mathrm{Pe}}w}dw\\
=\;&\frac{1+(-1)^N}{2}\Big(\frac{e\;\mathrm{Pe}}{1+\mathrm{Pe}N/2}\Big)^{\frac{N}{2}}\frac{\Gamma(\frac{1+N}{2})}{\sqrt{\pi(1+\mathrm{Pe}N/2)}}
\end{aligned}
\tag{2.64}
$$

in which we introduce the changes of variable $\xi=\sqrt{x}$ and $x=we^{1-w}$. Therefore,

$$
P_\infty(\xi)=\frac{e^{\frac{\mathrm{Pe}-2}{2\mathrm{Pe}}w_0(\xi^2)}}{1-w_0(\xi^2)}-\frac{e^{\frac{\mathrm{Pe}-2}{2\mathrm{Pe}}w_{-1}(\xi^2)}}{1-w_{-1}(\xi^2)},\quad \xi\in(-1,1). \tag{2.65}
$$

Further, the singular limits of the PDF as ξ approaches 0 and ±1 are

$$
\begin{aligned}
\lim_{\xi\to(-1)^+,1^-}\frac{e^{\frac{\mathrm{Pe}-2}{2\mathrm{Pe}}w_0(\xi^2)}}{1-w_0(\xi^2)}-\frac{e^{\frac{\mathrm{Pe}-2}{2\mathrm{Pe}}w_{-1}(\xi^2)}}{1-w_{-1}(\xi^2)}&=\lim_{\varepsilon\to0^+}\frac{e^{\frac{\mathrm{Pe}-2}{2\mathrm{Pe}}(1-\varepsilon)}}{\varepsilon}-\frac{e^{\frac{\mathrm{Pe}-2}{2\mathrm{Pe}}(1+\varepsilon)}}{-\varepsilon}=+\infty\\
\lim_{\xi\to0^+,0^-}\frac{e^{\frac{\mathrm{Pe}-2}{2\mathrm{Pe}}w_0(\xi^2)}}{1-w_0(\xi^2)}-\frac{e^{\frac{\mathrm{Pe}-2}{2\mathrm{Pe}}w_{-1}(\xi^2)}}{1-w_{-1}(\xi^2)}&=\lim_{\varepsilon\to0^+}\frac{e^{\frac{\mathrm{Pe}-2}{2\mathrm{Pe}}\varepsilon}}{1-\varepsilon}-\frac{\varepsilon e^{\frac{\mathrm{Pe}-2}{2\varepsilon\mathrm{Pe}}}}{\varepsilon-1}=\begin{cases}1, & \mathrm{Pe}\le2\\ +\infty, & \mathrm{Pe}>2\end{cases}.
\end{aligned}
\tag{2.66}
$$

So again, from the series reconstruction perspective, $\mathrm{Pe}=2$ is the critical value. Also, when $\mathrm{Pe}>2$, the scalar has a much higher probability of being near 0 due to a singularity.

Figure 2.15 through 2.18 are the Monte-Carlo simulations that illustrate the spatio-temporal dynamics of $P_{x,t}(\xi)$ with $T_0(x)=2xe^{-x^2}$. Similar to the PDF evolution shown in Figure 2.11 and 2.12, the initial Dirac mass supported by the curve $(\sqrt{2e}xe^{-x^2},\ x)$ is smeared as time advances. We observe that the smearing is symmetric with respect to the origin in the $x-\xi$ plane, due to the symmetry of the initial profile and the x-independence of the random drift. Also, four high density regions emerge near $\xi=0$ and $\xi=\pm1$. For $\mathrm{Pe}=4$, the high density regions near $\xi=0$ remains for all x's at $t>1$, whereas they vanishes for $\mathrm{Pe}=2$.

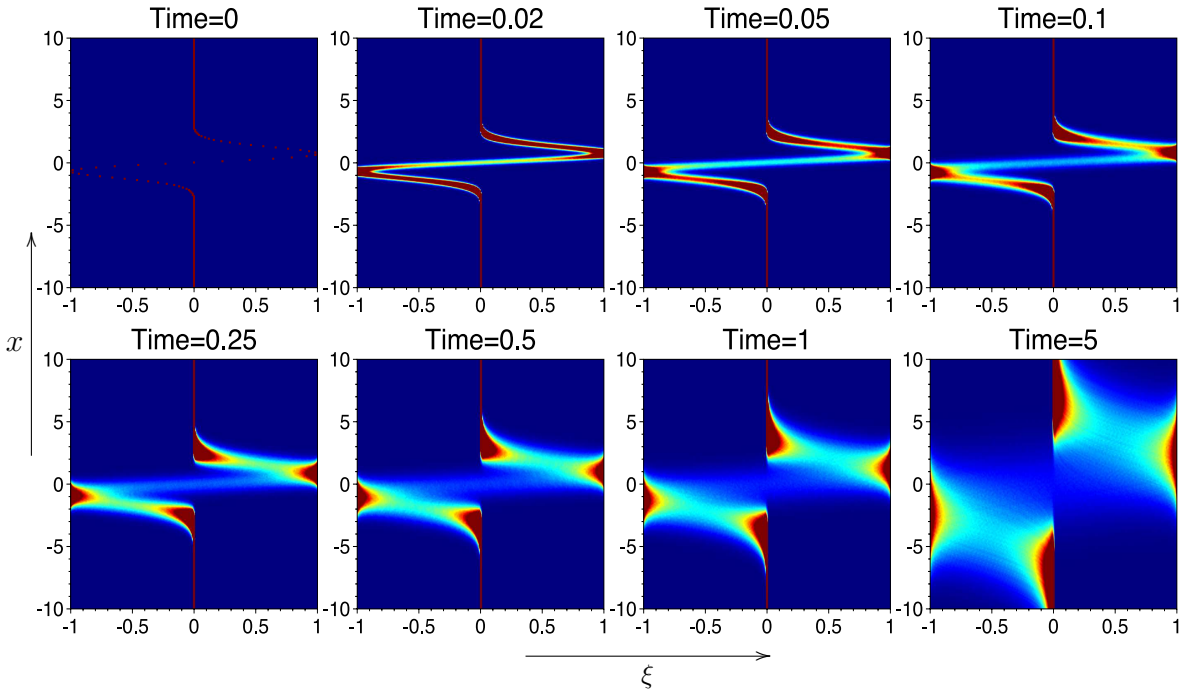

Figure 2.15: The PDF Dynamics of $P_{x,t}(\xi)$ with $T_0(x) = 2xe^{-x^2}$ where Pe $= 2$

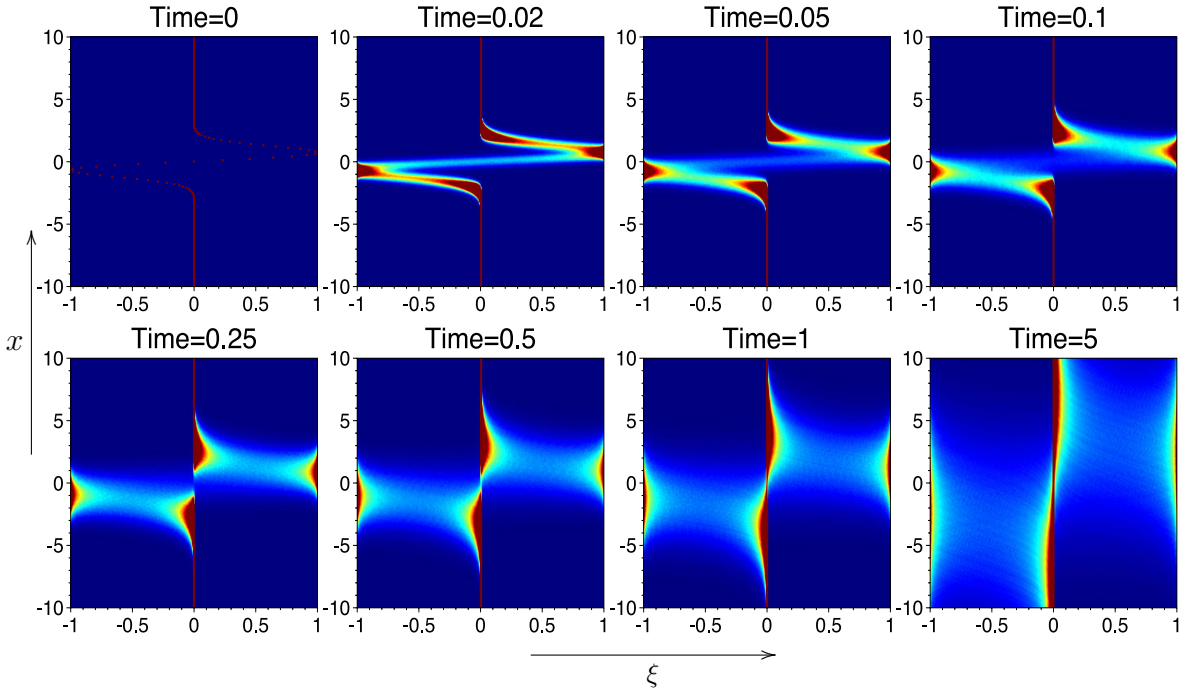

Figure 2.16: The PDF Dynamics of $P_{x,t}(\xi)$ with $T_0(x) = 2xe^{-x^2}$ where Pe $= 4$

Figure 2.15 and 2.16 also suggest that at the edges of the high density regions near $\xi = 0$, if we fix x, there seems to be a "jump discontinuity" in the PDF at $\xi = 0$, where the grayscale changes abruptly from blue to green. This is different from the singularities as we see where $P_{x,t}(\xi) = \infty$ and it is most noticeable in the $t = 1, 5$ panels in Figure 2.15 and $t = 0.25, 0.5$ panels in Figure 2.16. Figure 2.17 is an illustration of such a phenomena at $x = 2.5, t = 1$ for Pe $= 2$, which is essentially a horizontal slice of the "Time=1" panel in Figure 2.15. The rigorous analysis for this phenomena is an open question since the exact PDF is not available. An intuitive explanation can be made since the initial tracer field $T_0 = 2xe^{-x^2}$ has a positive bump near $x = 2.5$, which is translated by random advection and is smoothed by molecular diffusion as time advances. But by $t = 1$, the tracer at these locations will remain positive, often small, unless the initial field is randomly translated so far away that the tracer can admit negative values which are initially located at $x < 0$. Such a rare, large deviation has a probability much smaller than that of the realizations producing a positive scalar at $(x = 2.5, t = 1)$, which leads to a jump discontinuity in the tracer PDF at $\xi = 0$.

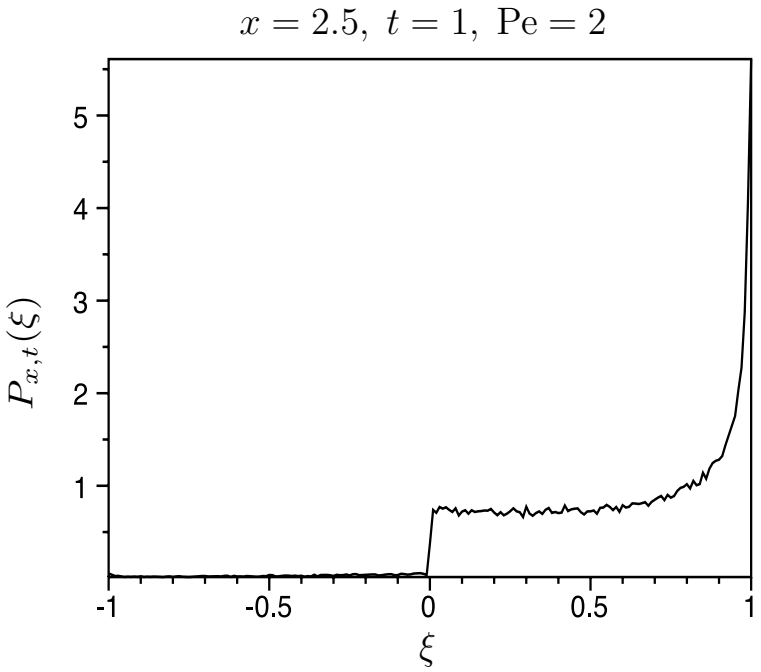

Figure 2.17: "Jump Discontinuity" of $P_{x,t}(\xi)$ with $T_0(x) = 2xe^{-x^2}$

Eventually at $t = 1000$, we see in Figure 2.18 three high density, vertical stripes, near $\xi = 0$ and $\xi = \pm 1$ respectively, for Pe $= 4$, whereas only two such stripes exist near $\xi = \pm 1$ for Pe $= 2$.

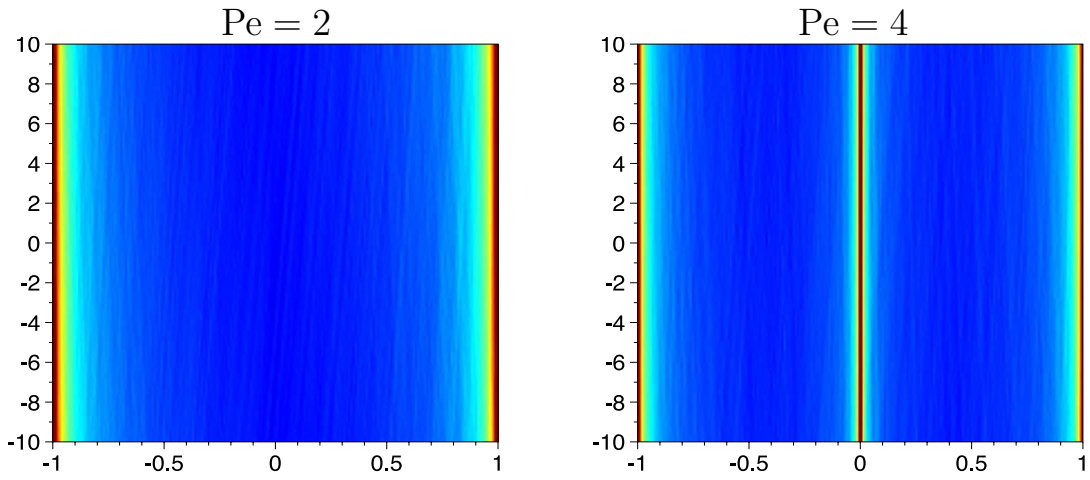

Figure 2.18: Monte-Carlo Simulations for $P_{x,t}(\xi)$ with $T_0(x) = 2xe^{-x^2}$ at $t = 1000$

The formula (2.62) also allows us to perform series reconstructions using the moments as discussed in Section 2.2, with which we compare the Monte-Carlo simulations in Figure 2.19 and two approximations exhibit favorable agreement. Here we employ standard Chebyshev polynomials to reconstruct the PDF and we set $r(\xi) = \sqrt{1-\xi^2}$ for Pe $= 2$ and $r(\xi) = \xi\sqrt{1-\xi^2}$ for Pe $= 4$. And the extensions discussed in Sec. 3.3 is not required here because $\xi \in [-1, 1]$. In Figure 2.19, the limit distributions $P_\infty(\xi)$ are not plotted since it overlaps completely with the series reconstructions.

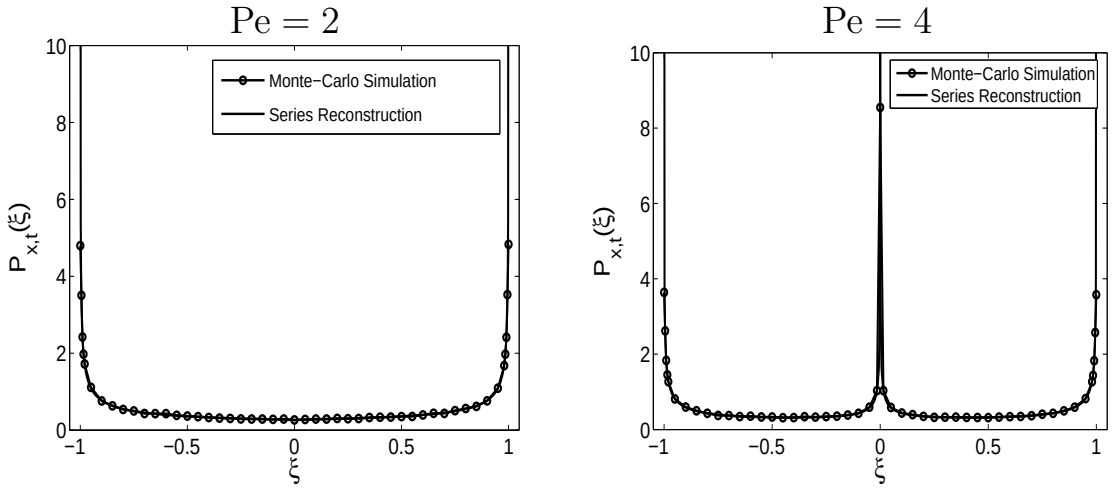

Figure 2.19: 10-Term Series Reconstions of $P_{0,t}(\xi)$ with $T_0(x) = 2xe^{-x^2}$ at $t = 1000$

2.4.3 Bimodal, Positive Initial Data $T_0(x) = e^{-(x-A)^2} + e^{-(x+A)^2}$

For this initial data, which is a sum of two Gaussians, the exact PDF solution is not available, although the corresponding random advection-diffusion problem (3.1) can again be solved analytically since it is linear. Moreover, we can obtain the exact moments for the renormalized scalar utilizing Eq.(2.22)

$$\langle \xi^N \rangle_\gamma = \frac{2^{-N}}{\sqrt{1+\frac{a}{b'}N}} \exp\Big(-\frac{N\pi^2(x+A)^2}{aN+b'}\Big) \sum_{j=0}^{N} \binom{N}{j} \exp\Big(\frac{4\pi^2 Aj[aA(j-N)+bx]}{b'(aN+b')}\Big). \tag{2.67}$$

It is obvious that in the long time limit $\langle \xi^N \rangle_\gamma \sim (1+\frac{\mathrm{Pe}}{2}N)^{-\frac{1}{2}}$ and thus the PDF is asymptotically equal to $P_{0,t}(\xi)$ for the uni-modal, Gaussian data $T_0(x) = e^{-x^2}$ from Eq.(2.24). In fact, this has been discussed in Section 2.1.3, since for large times $b = 4\kappa t \sim 4\kappa t + 1 = b'$ and therefore the PDFs for $T_0(x) = e^{-x^2}$ ($\hat{T}_0(0) \neq 0$) and $T_0(x) = \delta(x)$ are asymptotically equal to each other.

The short time PDF dynamics for this initial data has a unique feature different than the two cases we have seen in Section 2.4.1 and 2.4.2 — another singularity emerges besides the ones at $\xi = 0,\ 1$. This is illustrated in Figure 2.20. We can see from the figure that a singularity near $x = 0$ moves towards $\xi = 1$ as time increases and eventually merges with the singularity at $\xi = 1$. It is easy to check numerically that the ξ value at this singularity is approximately the corresponding pure heat solution at $x = 0$, which is a local minimum. This minimum becomes a maximum at a later time so it will merge with the maximum at $\xi = 1$ at later times. In light of this observation, next we present an explanation of why the singularities of $P_{x,t}(\xi)$ can only appear at the extrema of the renormalized pure heat solution.

2.4.4 Identifying the Singularities in $P_{x,t}(\xi)$

Now we show that, *at time t, if* $\Big(x^*, \xi^* = \frac{T(x^*,t)}{T_{max}(t)}\Big)$ *with* $|x^*| < \infty$ *is a critical point, namely,* $\frac{\partial}{\partial x}\Big(\frac{T(x^*,t)}{T_{max}(t)}\Big)\Big|_{x=x^*} = 0$ *, then* $P_{x,t}(\xi^*) = \infty$ *for any x, provided that* $\frac{T(x,t)}{T_{max}(t)}$ *is differentiable in x and satisfies the Lipshitz condition locally.* To see this, we consider

$$\begin{aligned} p(\varepsilon) &:= \mathrm{Prob}(|\frac{T(x^*,t)}{T_{max}(t)} - \xi^*| < \varepsilon) \\ &= \int_I P_{x,t}(\xi) d\xi \end{aligned} \tag{2.68}$$

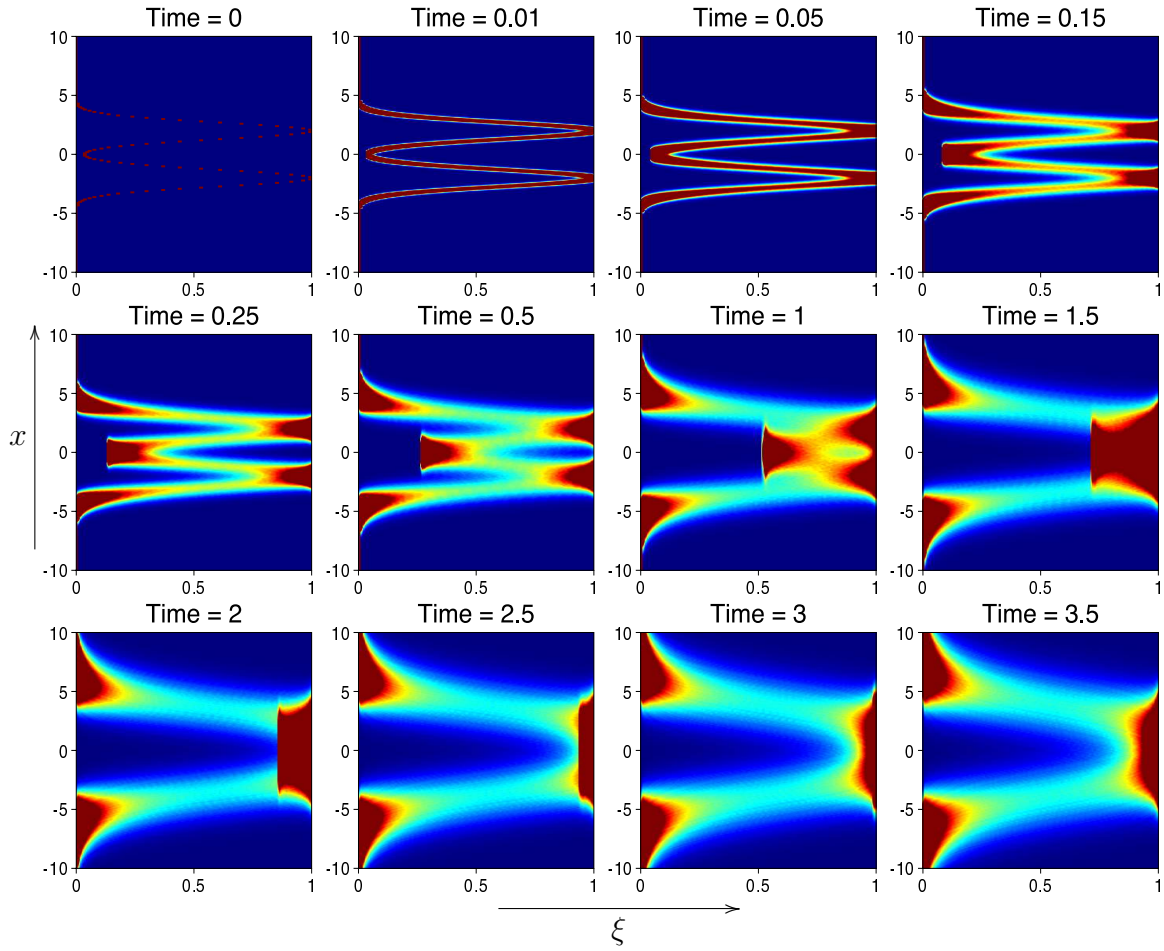

Figure 2.20: Short Time PDF Dynamics for $T_0(x) = e^{-(x-2)^2} + e^{-(x+2)^2}$

for any small $\varepsilon > 0$, where the integration interval $I = [\xi^* - \varepsilon, \xi^* + \varepsilon] \cap [0, 1]$. Thus $P_{x,t}(\xi^*) = \infty$ if and only if $\lim_{\varepsilon \downarrow 0} \frac{\varepsilon}{p(\varepsilon)} = 0$. Notice that for the same ξ^*, there can be multiple x^*'s such that $\frac{T(x^*,t)}{T_{max}(t)} = \xi^*$, but it suffices to consider the case where there is only one such x^* because we will see that we only need a lower bound for $p(\varepsilon)$ here.

Next we take the Taylor expansion of renormalized, random solution near (x^*, ξ^*). For the test problem (3.1), we can simply expand the pure heat solution, which is just a rigid translation of the random solution (2.12), and then replace x by $x - W(t)$. It is clear that when $|x - W(t) - x^*|$ is small, the renormalized random tracer satisfies

$$\left| \frac{T(x^*, t)}{T_{max}(t)} - \xi^* \right| \leq K_{x^*} |x - W(t) - x^*|^p \tag{2.69}$$

for some constant $p > 1$ and $K_{x^*} > 0$ determined by x^*, since (x^*, ξ^*) is a critical

point. Therefore $K_{x^*}|x - W(t) - x^*|^p < \varepsilon$ implies $|\frac{T(x^*,t)}{T_{max}(t)} - \xi^*| < \varepsilon$ and consequently, $\text{Prob}(K_{x^*}|x - W(t) - x^*|^p < \varepsilon) \leq p(\varepsilon)$. The probability on the left hand side of the inequality can be shown to be $O(\varepsilon^{1/p})$, via evaluating an elementary Gaussian integral. Thus $\lim_{\varepsilon \downarrow 0} \frac{\varepsilon}{p(\varepsilon)} = 0$.

However, the above arguments do not apply to $\xi^* = 0$, the heat solution at $|x| = \infty$, since we do not have local Taylor expansions at infinity. They also fails when there are infinitely many x^*'s such that $\frac{T(x^*,t)}{T_{max}(t)} = \xi^*$ and any (x^*, ξ^*) is not a critical point. Moreover, the question of whether such singularities at critical points exist in more complicated turbulent flows, where the solution is not just a random translation of the pure heat solution, remains open for further study.

2.5 Extended Model with a Source Term

Many geophysical problems are characterized not just by transport and diffusion, but also involve strong external sources, either through scalar production or destruction(Plasting and Young, 2006; Thiffeault et al., 2004). In the present calculation, to understand the role of such phenomena, scalar sources can be modeled with the addition of a scalar, deterministic, steady forcing function, $\Phi(x)$, and the governing equation for the scalar (3.1) becomes

$$\frac{\partial T}{\partial t} + \gamma(t)\frac{\partial T}{\partial x} = \kappa \frac{\partial^2 T}{\partial x^2} + \Phi(x) \tag{2.70}$$

It is interesting to compare the long time spatial distributions with and without the random white wind field. To have a finite long time limit, it is essential that the source function have spatial mean zero, namely, $\int_{-\infty}^{\infty} \Phi(x)dx = 0$.

The long time asymptotic solution, assumed to be non-zero, is given by

$$\begin{aligned} T_\infty^\omega(x) &= \lim_{t\to\infty} \int_{-\infty}^{\infty} e^{2\pi i k x} \hat{\Phi}(k) \left[\int_0^t e^{-4\pi^2 k^2 \kappa s - 2\pi i k W(s)} ds \right] dk \\ &= \int_{-\infty}^{\infty} e^{2\pi i k x}\, \widehat{T_\infty^\omega}(k)\, dk \end{aligned} \tag{2.71}$$

where $\hat{\Phi}(k)$ is the Fourier transform of $\Phi(x)$. Notice that the effect of the initial data vanishes since it decays to 0 at long time. If the random advection were absent (the

deterministic analogue), namely $\gamma(t) \equiv 0$, it is easy to verify that

$$\widehat{T_\infty}(k) = \frac{\hat{\Phi}(k)}{4\pi^2 k^2 \kappa} \tag{2.72}$$

Now we consider the mean of the random field T_∞^ω, in the presence of the white wind

$$\begin{aligned} \langle \widehat{T_\infty^\omega}(k) \rangle &= \hat{\Phi}(k) \lim_{t\to\infty} \int_0^t e^{-4\pi^2 k^2 \kappa s} \left\langle e^{-2\pi i k W(s)} \right\rangle ds \\ &= \frac{\hat{\Phi}(k)}{4\pi^2 k^2 (\kappa + \frac{\sigma^2}{2})} \end{aligned} \tag{2.73}$$

according to Eq.(2.71). This is just the counterpart of its deterministic version (2.72) by replacing κ with the effective diffusivity $\kappa + \frac{\sigma^2}{2}$, namely,

$$\frac{\langle T_\infty^\omega(x) \rangle}{T_\infty(x)} = \frac{\langle \widehat{T_\infty^\omega}(k) \rangle}{\widehat{T_\infty}(k)} = \frac{1}{1 + \frac{\mathrm{Pe}}{2}}. \tag{2.74}$$

This shows that the effect of the white wind on a sourced passive scalar equation always leads to a long time spatial distribution with mean values smaller than the deterministic counterpart, with an explicit, Péclet-dependent reduction.

Next we compare the mean of the two-point correlator of the random field in Fourier domain, $\langle \widehat{T_\infty^{\omega,2}}(j,k) \rangle$, with that of its deterministic analogue, $\widehat{T_\infty^2}(j,k)$. To recover the second moment of the random field, we only need to perform the two-dimensional inverse transform

$$\left\langle [T_\infty^\omega(x)]^2 \right\rangle = \int_{\mathbb{R}^2} e^{2\pi i (j+k)x} \left\langle \widehat{T_\infty^{\omega,2}}(j,k) \right\rangle dj\, dk \tag{2.75}$$

and likewise for $T_\infty^2(x)$. Explicit integrations over simplices in $\mathbb{R}^2$ yield

$$\begin{aligned} \left| \frac{\langle \widehat{T_\infty^{\omega,2}}(j,k) \rangle}{\widehat{T_\infty^2}(j,k)} \right| &= \frac{1}{1 + \frac{\mathrm{Pe}}{2}} \, \frac{1}{1 + \frac{\mathrm{Pe}}{2} \frac{(j+k)^2}{j^2+k^2}} \\ &< \frac{1}{1 + \frac{\mathrm{Pe}}{2}} \end{aligned} \tag{2.76}$$

for finite Pe, that is, the magnitude of each Fourier component of the second moment is also reduced in the presence of the random wind, with a similar Pe dependent reduction.

We also generalize these calculations for the higher order moments of the random field T_∞^ω

$$\left\langle \widehat{T_\infty^{\omega,N}}(k_1,\cdots,k_N)\right\rangle = (4\pi^2)^{-N}\prod_{i=1}^{N}\hat{\Phi}(k_i)\sum_{p_1,\ldots,p_N}\Big[\prod_{i=1}^{N}\Big(\kappa\sum_{j=1}^{i}k_{p_j}^2+\frac{\sigma^2}{2}(\sum_{j=1}^{i}k_{p_j})^2\Big)\Big]^{-1} \tag{2.77}$$

where $\{p_1,p_2,\cdots,p_N\}$ is any permutation of $\{1,2,\cdots,N\}$. These preliminary results indicate a non-trivial distribution and we will explore more thoroughly in future work.

2.6 Conclusions

We have explored the probability measures for a renormalized passive scalar diffusing in the presence of a random, Gaussian, white in time, wind field using a combination of tools. For initial data which is a single pure Gaussian profile, we are able to explicitly calculate in closed form the complete spatio-temporal probability measure. This is of great value in understanding the procedure for re-summing a measure from its statistical moments in that it provides an exact test problem, and further provides a mean to calculate directly asymptotic convergence rates for the reconstruction. For more general initial data, explicit calculations are not generally available, and we utilized well benchmarked orthogonal polynomial expansions and Monte-Carlo simulations for the reconstruction. For the bimodal initial data corresponding to the spatial derivative of a single Gaussian, we are able to explicitly calculate the exact long time asymptotic PDF, which was also useful in validating the Monte-Carlo simulations. For initial data comprised of a sum of spatial Gaussians, we employed Monte-Carlo simulation which documented the possibility of an interior singularity in the probability density function.

This elementary model provides a clear picture for the role in which the Péclet number plays in adjusting the spatio-temporal structure of the probability measure. Specifically, these calculations show a clear transition between the pure heat decay problem, which corresponds to a Dirac mass located at the heat solution, $\delta(\xi - e^{-x^2/(4\kappa t)})$, and the pure advection case, which formally is recognized as the singular limit of infinite Péclet number, corresponding to the Dirac mass $\delta(\xi)$. In such a case at large times, any observer at a fixed location is almost sure to be far from the center of where the initial distribution has been shifted. Between these two extreme cases, there is a balance between diffusion and advection, and the calculations provide the explicit measures depicting this balance.

These studies provide solid benchmarking for future studies involving more complicated fluid flows for which only a finite number of a statistical moments may be available. In such cases, we can approximate the probability measures of the random quantity with orthogonal polynomial expansions without the knowledge of the exact PDF.

Chapter 3

The Majda Model

In this chapter, we extend the elementary model in Chapter 1 by adding spatial dependence to the random advection. Consider the Majda Model(Majda, 1993b) for a passive tracer governed by a non-dimensional, 2D random advection-diffusion equation with planar initial condition:

$$T_t + \gamma(t) x T_y = \frac{1}{\mathrm{Pe}} \Delta_{x,y} T, \qquad T(x, y, t = 0) = T_0(y) \tag{3.1}$$

where Pe is the Péclet number which characterizes the importance of molecular diffusion and $\gamma(t)$ is again the temporal white noise satisfying Eq. (2.2) and $T_0(y)$ is a Gaussian Random Field with the spectral representation

$$T_0(y) = \int_{-\infty}^{\infty} e^{2\pi i k y} |k|^{\alpha/2} \hat{\phi}_0(k) dW(k). \tag{3.2}$$

Here the function $\hat{\phi}_0(k)$ is a rapidly decreasing cut-off function satisfying $\hat{\phi}_0(k) = \hat{\phi}_0(-k)$ and $\hat{\phi}_0(0) \neq 0$. Traditionally $\hat{\phi}_0(k)$ is renormalized so that $\hat{\phi}_0(0) = 1$. However, as we will see in (3.14), this is not necessary and therefore we do not renormalize it. The spectral parameter, α determines the spatial correlation scales of the initial scalar field, with increasing α corresponding to shorter range correlation. Lastly, $dW(k)$ is a complex white noise with

$$\langle dW(k) \rangle_W = 0, \qquad \langle dW(k) dW(k') \rangle_W = \delta(k + k') dk \, dk' \tag{3.3}$$

Given a fixed realization of $\gamma(t), t > 0$, Eq. (3.1) can be solved (in the Stratonovich's

sense) for all times as

$$T(x,y,t) = \int_{-\infty}^{\infty} e^{2\pi i k[y-B(t)x]} |k|^{\alpha/2} \hat{\phi}_0(k) e^{-\frac{4\pi^2 k^2}{\mathrm{Pe}}[t+\xi(t)]} dW(k). \tag{3.4}$$

where $B(t) = \int_0^t \gamma(s)ds$ is a Wiener Process and $\xi(t) = \int_0^t B^2(s)ds$ is the L^2-norm of the Wiener Process. To see this, one can first derive the evolution equation for the two-dimensional Fourier transform of the scalar field, namely,

$$\hat{T}(k_1,k_2,t) = \int_{\mathbb{R}^2} e^{-2\pi i(k_1 x + k_2 y)} T(x,y,t) dk_1 dk_2 \tag{3.5}$$

and get

$$\begin{aligned} \frac{\partial \hat{T}}{\partial t} - \gamma(t) k_2 \frac{\partial \hat{T}}{\partial k_1} &= -\frac{4\pi^2(k_1^2+k_2^2)}{\mathrm{Pe}}\, \hat{T}, \quad (k_1,k_2) \in \mathbb{R}^2,\ t>0 \\ \hat{T}|_{\,t=0} &= \delta(k_1)\hat{T}_0(k_2). \end{aligned} \tag{3.6}$$

Then a straight forward application of the method of characteristics yelds

$$\hat{T}(k_1,k_2,t) = \delta(k_1 + B(t)k_2)\ \hat{T}_0(k_2)\ e^{-\frac{4\pi^2}{\mathrm{Pe}}\left(k_2^2 t + \int_0^t [k_1 + B(t)k_2 - B(s)k_2]^2 ds\right)} \tag{3.7}$$

and an inverse Fourier tranform for the scalar in physical space provides the solution (3.4) to the original problem. Notice that the planar initial distribution reduces the two-dimensional Fourier integral to one-dimensional and the effects of the random shear are manifested in only the phase term $e^{2\pi i k[y-B(t)x]}$ as a random rotation and in the diffusive damping term $e^{-\frac{4\pi^2 k^2}{\mathrm{Pe}}[t+\xi(t)]}$ as an enhancement. Consequently, the scalar field remains effectively one-dimensional and $y - B(t)x$ can be regarded as a random, self-simiilar variable.

It is known that soluble, closed form moment equation for the $N-$point correlation function $\langle \prod_{i=1}^N T(x_i,y_i,t)\rangle_{W,\gamma}$ is available for this problem(Majda, 1993b; McLaughlin and Majda, 1996). Furthermore, this random process $\xi(t)$ can be transformed into a random variable η, utilizing the rescaling property of the Wiener process (Vanden-Eijnden, 2001), namely,

$$\xi(t) = t^2\eta = t^2 \int_0^1 B^2(s)ds, \qquad \text{in law} \tag{3.8}$$

Therefore, we can replace $\xi(t)$ by $t^2\eta$ to simplify the calculations while the statistical

properties of the tracer field remain the same.

It's easy to check via cluster expansion that, the moment of arbitrary order of T defined in (3.4) is independent of x and y(Majda, 1993b; McLaughlin and Majda, 1996). Thus this is a homogeneous random field at all times. Without loss of generality, for single-point statistics, it suffices to study the statistics of

$$T(0,0,t) = \int_{-\infty}^{\infty} |k|^{\alpha/2} \hat{\phi}_0(k) e^{-\frac{4\pi^2 k^2}{\mathrm{Pe}}[t+t^2\eta]} dW(k). \tag{3.9}$$

Notice the in this solution for T, the randomness that the tracer inherited from the random shear is manifested through a single random variable, η, as the previous work (Bronski, 2003; Vanden-Eijnden, 2001) has recovered. Next we will see how the full tracer PDF is connected to the PDF of η. And it has been established (Bronski and McLaughlin, 1997; Bronski and McLaughlin, 2000a; Vanden-Eijnden, 2001) that for finite Pe, the invariant (infinite time) probability measure of the renormalized tracer, denoted as $\bar{T}$, has stretched exponential tails controlled by the parameter α:

$$P_{\bar{T}}(\bar{T}) \sim A(\alpha) e^{-B(\alpha)|\bar{T}|^{\frac{4}{3+\alpha}} + o(|\bar{T}|^{\frac{4}{3+\alpha}})}, \quad |\bar{T}| \to \infty \tag{3.10}$$

In this thesis, we present the following new results for this simple shear model:

1. The integral representation for the renormalized tracer PDF of the Majda shear model is established via the Total Law of Probability. This representation enables the usage of numerical integration to study the spatio-temporal evolution of the tracer PDF, whose results are verified by Monte Carlo simulations, but with much improved computation cost and accuracy.

2. From the numerical results for the PDF evolution, a *non-monotonic*, transitional phenomena is discovered and then defined as "breathing". An explicit example is proposed in Section 3.4 to rigorously predict such phenomena.

3. Rigorous asymptotic analysis shows that for a broad class of initial cut-off functions, the long time, invariant PDF has a Gaussian core. In other words, the stretched exponential behavior of the tails does not extend to the core.

4. Through the integral representation of the tracer PDF in the integral form, the "breathing" PDF is identified as the consequence of choosing specific cut-off functions, by exploring different time scalings in the diffusionless limit.

5. As an extension to previous work, the critical rate at which the stretched exponential region in the tracer PDF propagates towards the tail is identified, by following the curves $\bar{T} = Ct^{\gamma}$ in the tracer ($\bar{T}$)-time (t) phase plane.

3.1 The Law of Total Probability

Given any fixed realization of $\gamma(t)$ for $t \geq 0$, or equivalently in law, η, (3.4) suggests that T is still a Gaussian Random Field *conditionally*, with conditional PDF

$$P_{T|\eta}(T|\eta) = \frac{1}{\sqrt{2\pi\sigma_c^2(\eta,t)}} e^{-\frac{T^2}{2\sigma_c^2(\eta,t)}} \tag{3.11}$$

in which the conditional variance $\sigma_c^2(\eta,t)$ can be computed from (3.9) as

$$\sigma_c^2(\eta,t) = \langle T^2 \rangle_W = \int_{-\infty}^{\infty} |k|^{\alpha} \hat{\phi}_0^2(k) e^{-\frac{8\pi^2 k^2}{\mathrm{Pe}}(t+t^2\eta)} dk \ . \tag{3.12}$$

Further, if we renormalize T with its unconditional variance (Majda, 1993b)

$$\sigma_{uc}^2(t) = \langle T^2 \rangle_{W,\eta} = \int_{-\infty}^{\infty} \frac{|k|^{\alpha} \hat{\phi}_0^2(k) e^{-\frac{8\pi^2 k^2}{\mathrm{Pe}}t}}{\sqrt{\cosh \frac{4\pi k t}{\sqrt{\mathrm{Pe}}}}} dk \ . \tag{3.13}$$

so that $\bar{T} = \frac{T}{\sigma_{uc}(t)}$ has unit variance, very similar formula for $P_{\bar{T}|\eta}(\bar{T}|\eta)$ follows with σ_c^2 in (3.11) replaced by

$$\sigma^2(\eta,t) = \frac{\sigma_c^2(\eta,t)}{\sigma_{uc}^2(t)} \ . \tag{3.14}$$

The details of the averaging in Eq.(3.13) will be shown in the Appendix. Then *the Law of Total Probability* implies that the unconditional PDF for $\bar{T}(0,0,t)$, which we denote simply as $\bar{T}$ from now on since it is a homogeneous field in space, can be calculated as

$$P_{\bar{T}}(\bar{T}) = \int_0^{\infty} P_{\bar{T}|\eta}(\bar{T}|\eta) P_{\eta}(\eta) d\eta. \tag{3.15}$$

From this formulation, we can see that the time evolution of the tracer PDF is completely manifested in the time dependence of σ^2. Also, we need to know $P_{\eta}(\eta)$ to evaluate the tracer PDF. Although the explicit formula for $P_{\eta}(\eta)$, the probability density function for the L^2 norm of the Wiener process $B(t)$, is beyond authors' knowledge, it is known to have the inverse Laplace Transform representation (Bronski, 2003;

Vanden-Eijnden, 2001):

$$P_\eta(\eta) = \frac{1}{2\pi i}\int_{-i\infty}^{i\infty}\prod_{k=1}^{\infty}\Big(1+\frac{2s}{(k-\frac{1}{2})^2\pi^2}\Big)^{-\frac{1}{2}}e^{s\eta}ds \tag{3.16}$$

for which we will derive in details in the Appendix.

3.2 PDF Dynamics: Monte Carlo Simulation and Numerical Integration

Previous work has explored the long time, tail behavior of the renormailzed tracer PDF, $P_{\bar{T}}(\bar{T})$, and rigorously predict the emergence of heavy-tailed distributions. However, its finite time and the finite tracer value dynamics remains an open question. In this section, we use two different numerical approaches to simulate the evolution of the PDF. These two sets of results support the validity of the simulation algorithms by their mutual agreement, and further illuminate the analytical study discussed in Section 3.3. In particular, a nontrivial, transitional phenomena which was not documented before is revealed by the numerical results.

3.2.1 Monte Carlo Simulation for the Tracer PDF

As a universal, powerful tool for stochastic problems, Monte Carlo simulation can be readily developed in light of the random solution (3.4) for the majda1993rus model, to illustrate the temporal evolution of the renormalized tracer PDF, $P_{\bar{T}}(\bar{T})$, where $\bar{T} = \frac{T}{\sigma_{uc}(t)}$ and σ_{uc} is defined in (3.13) so that $\langle \bar{T}^2\rangle_{W,\eta} = 1$. In particular, the Fourier integral is first truncated for $|k| > K$ (K fixed) and then is discretized with $2N_k$ Fourier modes as

$$T(x,y,t) \approx \sum_{j=-N_k}^{N_k-1} e^{\frac{2\pi i j K}{N_k}[y-B(t)x]-\frac{4\pi^2 j^2 K^2}{N_k^2 \mathrm{Pe}}[t+\xi(t)]}\Big|\frac{jK}{N_k}\Big|^{\frac{\alpha}{2}}\hat{\phi}_0\Big(\frac{jK}{N_k}\Big)(w_j^r + i w_j^i) \tag{3.17}$$

where w_j^r, w_j^i are the real and imaginary parts of the discretized complex white noise $dW(k)$, respectively and thus they are i.i.d., Gaussian random numbers with variance $\frac{K}{N_k}$. With a simple random number generator, the summing in (3.17) for one realization of the random field $T(x,y,t)$ can be made highly efficient via FFT (Fast Fourier Transform) given a realization of $\gamma(t), t \geq 0$ and $(w_j^r, w_j^i), j = -N_k, \cdots, N_k - 1$. Furthermore,

at each time step, a histogram of $\bar{T}$ as an approximation to $P_{\bar{T}}(\bar{T})$ requires a sample of $R_f \times R_\gamma$ realizations of $T(0,0,t)$ computed by (3.17) and renormalized by the sample variance, where R_f is the number of realizations of the initial field, (w_j^r, w_j^i) and R_γ is the number of realizations of the random shear, $(B(t), \xi(t))$.

To obtain the realizations for the Wiener process $B(t)$ and its L^2-norm, $\xi(t)$, we utilize the scaling properties of $B(t)$ and $\xi(t)$, namely, $B(t) = \sqrt{t}B(1)$ and $\xi(t) = t^2\eta$ *in law*, with η defined in (3.8). Moreover, the Law of Large Numbers guarantees that as the temporal discretization, N_t, goes to infinity, the following approximations converges with probability 1:

$$B(1) \approx \sum_{j=1}^{N_t} dB_j \quad \text{and} \quad \eta \approx \frac{1}{N_t} \sum_{l=1}^{N_t} \Big(\sum_{j=1}^{l} dB_j \Big)^2 \tag{3.18}$$

where $dB_j, j = 1, 2, \cdots, N_t$ are i.i.d., Gaussian random variables with variance $\frac{1}{N_t}$. Consequently, instead of generating realizations for $(B(t), \xi(t))$ at each time step, we can repeatedly use the same sample of $(B(1), \eta)$ at different times and multiply it with proper time scalings and thus the temporal complexity of the simulation is greatly reduced.

To summarize, the total computation count of the Monte Carlo simulation consists of the one-time generation of the samples for $(w_j^r, w_j^i), j = -N_k, \cdots, N_k - 1$ and $(B(1), \eta)$, which are of order $R_f N_k$ and $R_\gamma N_t$ respectively, and summing (3.17) with FFT at each time step, which is of order $R_f R_\gamma N_k \ln N_k$. It is obvious that other than the influences of discretizations N_k and N_t, the computation complexity is greatly intensified when performing the FFT summing, by the fact that both of the two sources of randomness, the initial random field and the random shear, need enough realizations to obtain good approximations to the statistical distributions, namely, the product $R_f R_\gamma$ is large. In our simulations, by setting $N_k = N_t = 512$ and $R_f = R_\gamma = 10^6$, we obtain reasonably smooth, statistically stationary histograms that agree with the PDF numerically computed as described below.

3.2.2 Numerical Integration for the Tracer PDF

Although the Monte Carlo simulations are straightforward to implement, we need some independent methodology to verify the above results. And more importantly, robust as Monte Carlo simulations are, the statistical convergence is generally slow which in this problem, leads to intense computation complexity as mentioned before. Alternatively,

utilizing the integral forms which we discussed in Section 3.1, we can directly compute the tracer PDF in its simple, integral form (3.15) with numerical quadratures, to avoid the complex simulation. However, with only the integral representations (3.12), (3.13) and (3.16) for $\sigma_c^2, \sigma_{uc}^2$ and $P_\eta(\eta)$, respectively, we have to also evaluate them numerically. In particular, the evaluation of $P_\eta(\eta)$ will be discussed in Appendix, where we find the analytic continuation of $(\cosh\sqrt{2s})^{-1/2}$ along the integration path, the imaginary axis, or transform the original Bromwich integral (3.16) into a series of real integrals via (A.48). Moreover, for vary small or very large values of η, $P_\eta(\eta)$ can be asymptotically approximated by (A.47) and (A.49).

Figure 3.1 shows the results evaluating the integrator, compared with the Monte Carlo simulated PDF generated by setting $N_t = 10^3$ and $R_\gamma = 10^6$ as discussed in Section 3.2.1. In the right panel, the accuracy of numerically integrated $P_\eta(\eta)$ is estimated by comparing the numerical moments with the exact moments utilizing

$$\langle \eta^n \rangle = (-1)^n n! \frac{\partial^n}{\partial s^n} \frac{1}{\sqrt{\cosh\sqrt{2s}}}\Big|_{s=0} \approx \Delta\eta \sum_{i=1}^{10^6} (i\Delta\eta)^n \tilde{P}_\eta(i\Delta\eta) \tag{3.19}$$

where $\Delta\eta = 10^{-4}$ and $\tilde{P}_\eta$ is the numerically integrated PDF for η. Furthermore, the accuracy of numerically computed $P_\eta(\eta)$ is estimated by comparing the numerical moments with the exact moments generated by

$$\langle \eta^n \rangle = (-1)^n n! \frac{\partial^n}{\partial s^n} \frac{1}{\sqrt{\cosh\sqrt{2s}}}\Big|_{s=0} \tag{3.20}$$

The robustness of the integrator has also been verified by the numerical convergence test in which the relative error decreases with increasing resolution of the quadrature.

3.2.3 Numerical Results

Applying the methods discussed above, we obtain two sets numerical results from Monte Carlo simulation and numerical integration, which agree with each other, as shown in Figure 3.2. Here we set $\hat{\phi}_0(k) = e^{-\frac{k^2}{70}}$ and $\mathrm{Pe} = 10^5$, and implemented the numerical approximations for three different values of α, each at three different times. We can observe the gradual transition of the renormalized tracer PDF from its initial state, unit Gaussian, to its long time limiting state, strechted exponential (3.10). In fact, for this combination of $\hat{\phi}_0$ and Pe, the PDFs remains almost identical after $t = 1000$.

Notice that at large times, the stretched exponential region in each of the invariant

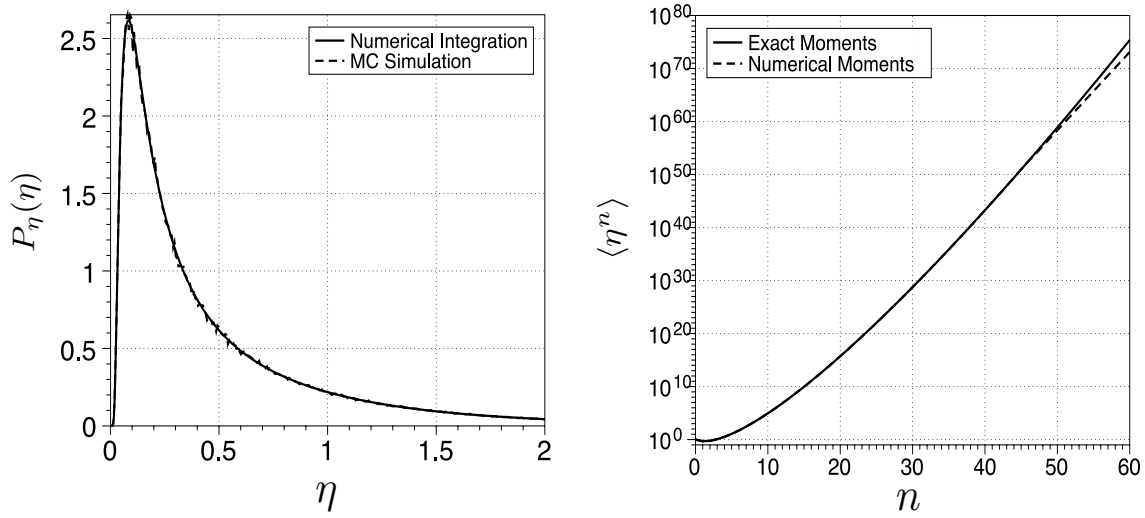

Figure 3.1: The Statistics of η. Left: Numerical Approximations for $P_\eta(\eta)$. Right: The Accuracy of Numerical Moments

measures extends far into the core, except for the small interval $|\bar{T}| \ll 1$, where the PDF remains Gaussian as we would see if we zoom in into these intervals and will analyze in Section 3.3. Also, the PDF tails heavier than Gaussian obviously suggest that there are also regions "lighter" than Gaussian, namely, for some intermediate values of $|\bar{T}|$, $P_{\bar{T}}(\bar{T})$ has to be less than its Gaussian value, $\exp(-\frac{\bar{T}^2}{2})/\sqrt{2\pi}$, since $\int_{-\infty}^{\infty} P_{\bar{T}}(\bar{T}) \equiv 1$.

3.2.4 Observation: The "Breathing" PDF

As expected, the above numerical results verifies that the renormalized PDF becomes stationary at sufficient large times and the shape is controlled by the value of the parameter α, while the effect of the initial cut-off function $\hat{\phi}_0$ vanishes. In particular, the long time, invariant measure for fixed α and 1/Pe, which will be derived in Section 3.3, reads

$$P_{\bar{T}}(\bar{T}) \sim \frac{\sqrt{C(\alpha)}}{\sqrt{2\pi}} \int_0^\infty \eta^{\frac{\alpha+1}{4}} e^{-\frac{\bar{T}^2}{2} C(\alpha) \eta^{\frac{\alpha+1}{2}}} P_\eta(\eta) d\eta, \quad t \to \infty \tag{3.21}$$

where $C(\alpha)$ is a function of α alone. However, there is a striking difference between the PDF evolutions for different initial cut-off functions $\hat{\phi}_0$, which is shown in Figure 3.3, where the numerical integrated PDFs are plotted.

In particular, we expect the behavior of the measure when $\hat{\phi}_0(k) = \exp(-\frac{k^2}{70})$ since at each intermediate time, the measure is just an "interpolation" between the initial, unit Gaussian and the long time, invariant measure (3.21), which is asymptotically

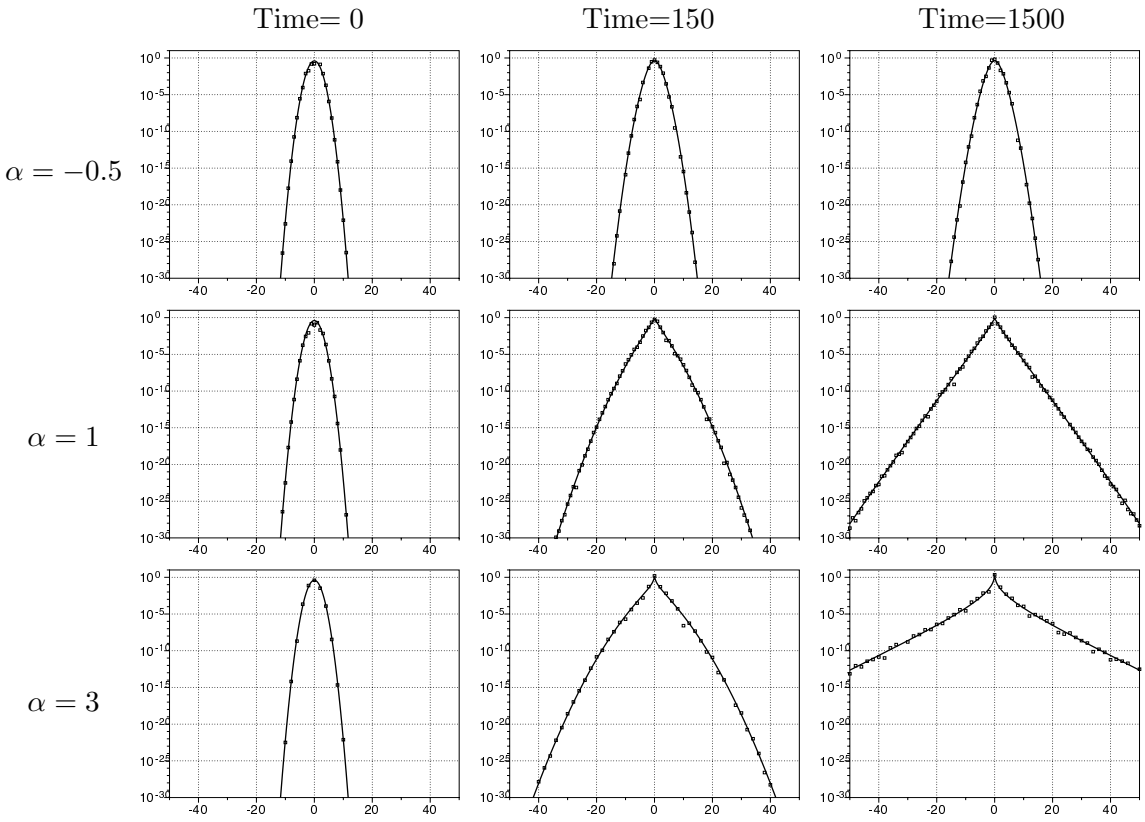

Figure 3.2: PDF Evolutions when $\hat{\phi}_0(k) = e^{-\frac{k^2}{70}}$ and Pe $= 10^5$ Obtained by Monte Carlo Simulation ($\square$) and Numerical Integration ($-$). Horizontal Axis — Renormalized Tracer $\bar{T}$. Vertical Axis — Probability Density $P_{\bar{T}}(\bar{T})$

equal to $Ae^{-B|\bar{T}|+o(|\bar{T}|)}$ in the tails when $\alpha = 1$ and thus is approximately straight lines as plotted in the panels for $t = 1000$. In contrast, when $\hat{\phi}_0(k) = \exp(-\frac{(|k|-20)^2}{70})$, it seems that at $t = 50$, the PDF tails are even heavier than the invariant measure. However, we know that this is not true since at the PDF has Gaussian tails so eventually it will be "lighter" than the invariant measure when $|\bar{T}|$ is large enough.

Therefore, what really distinguishes the two cases in Figure 3.3 is that for some values of $|\bar{T}|$, the tracer PDF inherited from $\hat{\phi}_0(k) = \exp(-\frac{(|k|-20)^2}{70})$ has a larger *concavity* than that of the corresponding invariant measure. As another example to illustrate this difference, now consider two different initial cut-off functions whose induced PDFs at three different times are compared in Figure 3.4, where the thick, solid line always corresponds to the intermediate, transitional PDF of interest. Clearly, the same discrepancy as shown in Figure 3.3 emerges: for $\hat{\phi}_0(k) = \frac{1}{100+k^{10}}$, the concavity of the intermediate measure at $t = 50$ does not exceed that of the invariant measure anywhere; while for $\hat{\phi}_0(k) = \frac{1+k^2}{100+k^{10}}$ and for $|\bar{T}|$ approximately between 0 and 3, the intermediate measure

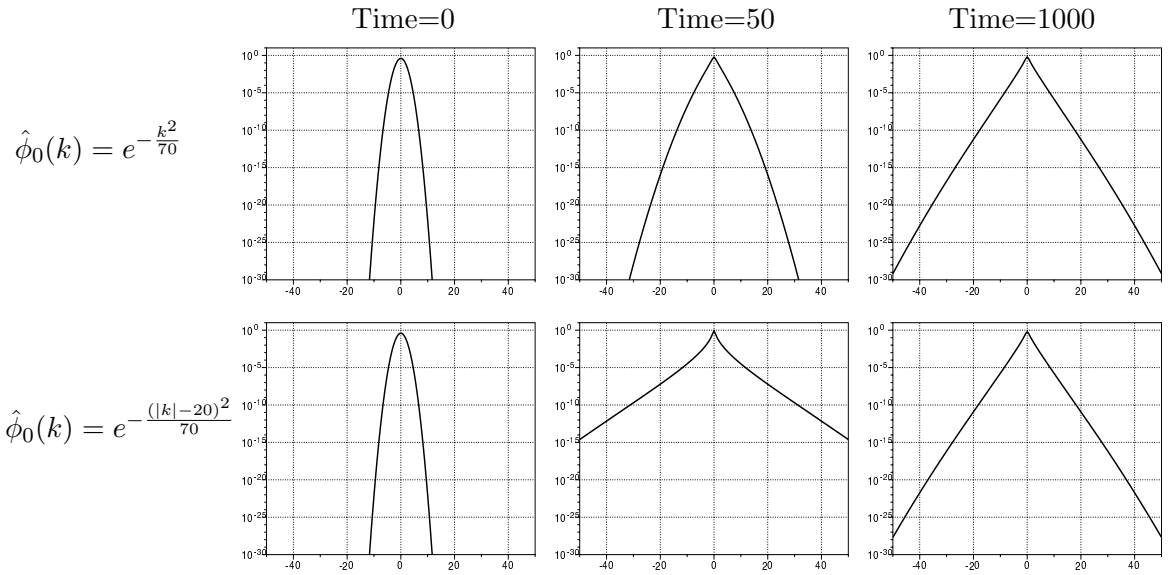

Figure 3.3: PDF Evolutions for Different $\hat{\phi}_0(k)$ where $\alpha = 1$, Pe $= 10^5$

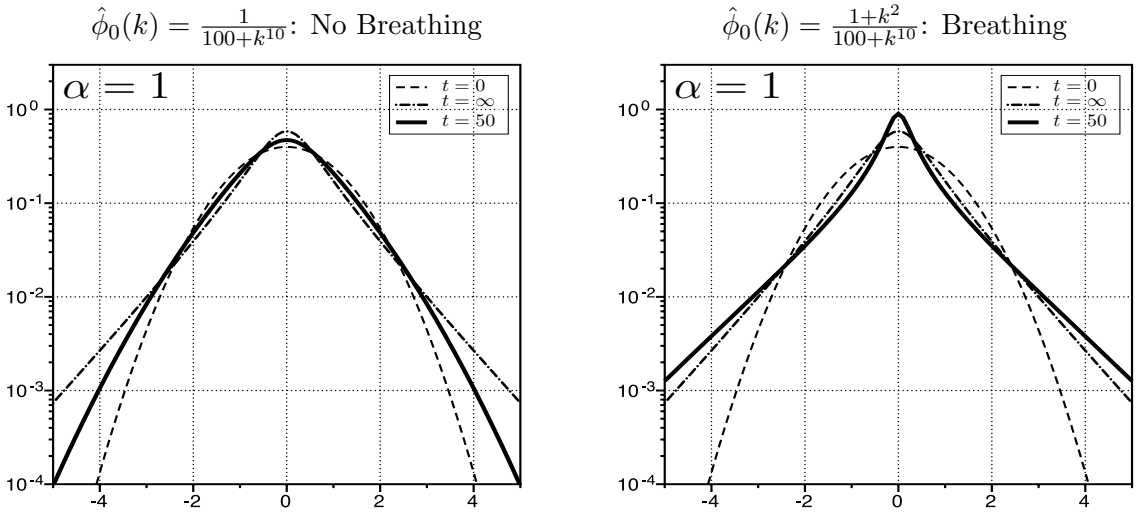

Figure 3.4: PDF Evolutions for Different $\hat{\phi}_0(k)$ where $\alpha = 1$, Pe $= 10^5$. Horizontal Axis — Renormalized Tracer $\bar{T}$. Vertical Axis — Probability Density $P_{\bar{T}}(\bar{T})$

has a larger concavity than the invariant measure.

Figure 3.5 further illustrates the dynamical evolution of the PDFs from $t = 0$ to $t = 400$, where the logarithm, $\ln P_{\bar{T}}(\bar{T})$, is colormapped and the ramp is set uniformly between $[-30, 1]$. Here $\ln P_{\bar{T}}(\bar{T})$ has larger values in red regions whereas it is smaller in blue regions. Again, the difference between the PDFs at intermediate times is salient from left to right.

There is another intriguing phenomena that co-exists with the concavity anomaly

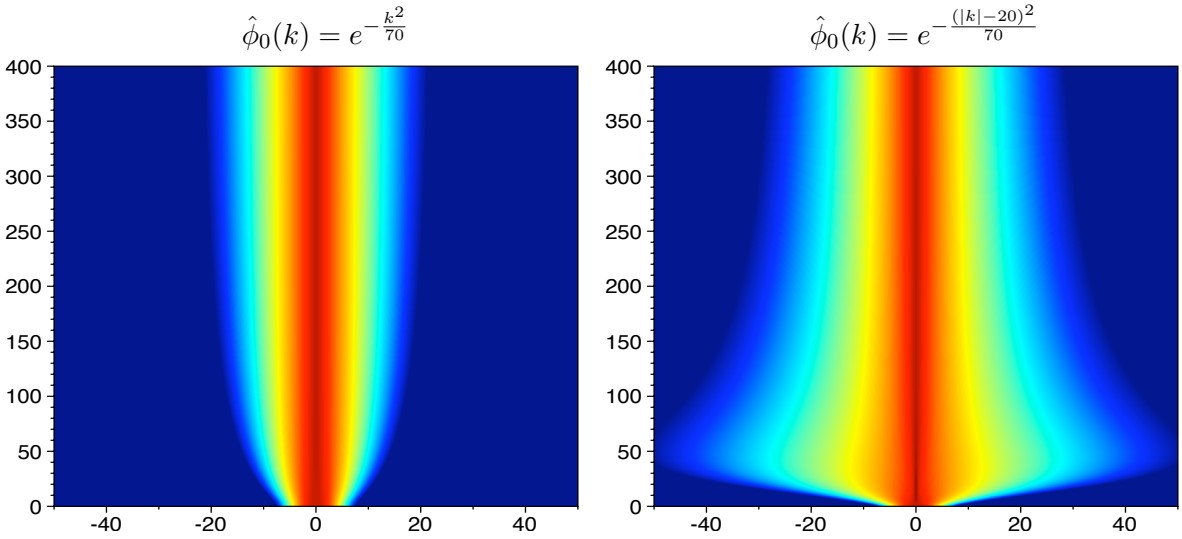

Figure 3.5: PDF Evolutions for Different $\hat{\phi}_0(k)$ where $\alpha = 1$, $\mathrm{Pe} = 10^5$

discussed above and can be observed in Figure 3.4, which we would also see if a similar figure for $\hat{\phi}_0(k) = \exp(-\frac{k^2}{70})$ and $\hat{\phi}_0(k) = \exp(-\frac{(|k|-20)^2}{70})$ is produced. In the right panel, $P_{\bar{T}}(0; t = 50)$ is larger than both $P_{\bar{T}}(0; t = 0)$ and $P_{\bar{T}}(0; t = \infty)$, which implies that $P_{\bar{T}}(0)$ has to evolve *non-monotonically* in time, whereas in the left panel, such non-monoticity cannot be seen and $P_{\bar{T}}(0; t = 0) < P_{\bar{T}}(0; t = 50) < P_{\bar{T}}(0; t = \infty)$. In fact, when $\hat{\phi}_0(k) = \frac{1}{100+k^{10}}$, $P_{\bar{T}}(\bar{T})$ varies monotonically in time from its initial value at $t = 0$, to its invariant value at $t = \infty$ for most fixed values of $\bar{T}$. However, in the case where $\hat{\phi}_0(k) = \frac{1+k^2}{100+k^{10}}$, these evolutions are not monotonic, which are shown in Figure 3.6, where $P_{\bar{T}}(\bar{T})$ is computed at $t = n\Delta t,\ n = 0, 1, \cdots, 50$ and $\Delta t = 25$.

Although the same non-monotonic evolution can also be recovered for the case where $\hat{\phi}_0(k) = \frac{1}{100+k^{10}}$ for $\bar{T}$ in some small intervals away from 0, the discrenpancy in the temporal dynamics of $P_{\bar{T}}(0)$ does distinguishes these two cases. Therefore, to identify this special *"breathing"* phenomena, we have the following definition based on the temporal monotonicity of $P_{\bar{T}}(0)$:

Definition: For any fixed $\varepsilon > 0$, the renormalized tracer PDF $P_{\bar{T}}(\bar{T})$ is said to *"breath"* in time if there exists at least one $0 < t^* < \infty$ such that $P_{\bar{T}}(\bar{T} = 0; t = t^*) \geq P_{\bar{T}}(\bar{T} = 0; t)$ for any $t \in (t^* - \varepsilon, t^* + \varepsilon)$.

One of the reasons that we are interested in this phenomena is that the probability, which is the integral of the density, concentrates near $|\bar{T}| = 0$ and physically this measures what values of the tracer are most likely to be observed. Therefore, its temporal evolution is important to our understanding of the random tracer field. It should be noted that when breathing occurs for $\hat{\phi}_0(k) = \frac{1+k^2}{100+k^{10}}$ or $\hat{\phi}_0(k) = \exp(-\frac{(|k|-20)^2}{70})$,

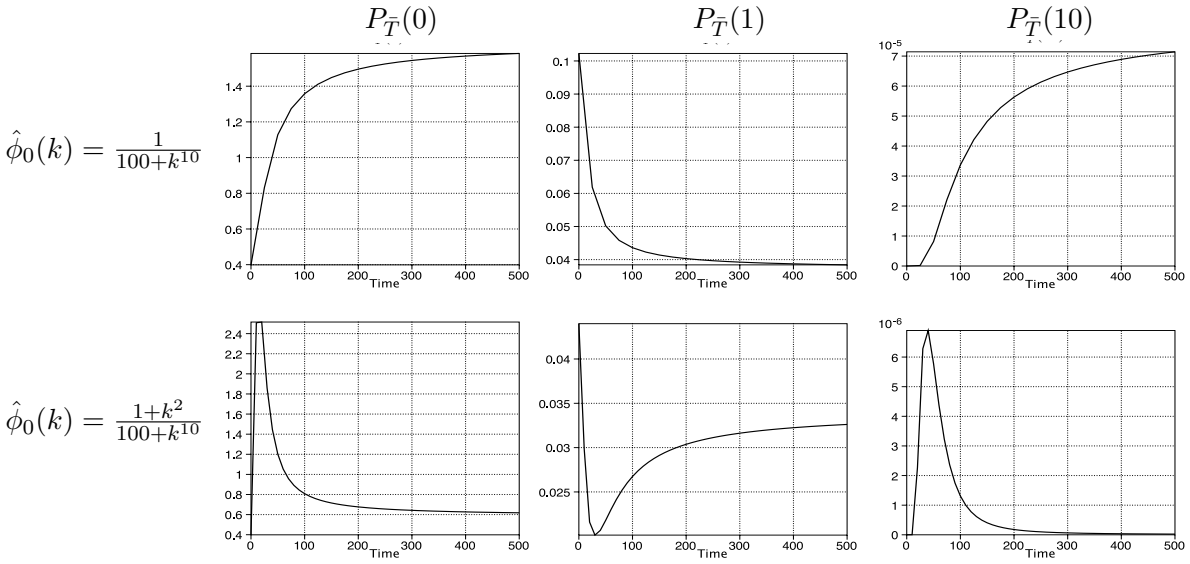

Figure 3.6: Fixed Point PDF Evolutions for Different $\hat{\phi}_0(k)$ where $\alpha = 1$, Pe $= 10^5$ Horizontal Axis — Time; Vertical Axis — $P_{\bar{T}}(\bar{T})$ with $\bar{T}$ Fixed.

the relationship between the concavity anomaly in the PDF and the temporal non-monotonicity of $P_{\bar{T}}(0)$ as discussed is an open question and we adopt the above definition for breathing due to its simplicity and unambiguity. As it will be shown in Section 3.3 and 3.4, the occurrence of this non-monotonic transition, or "breathing", is not universal for general $\hat{\phi}_0$. From the specific choices of $\hat{\phi}_0$ that invoke "breathing" as shown in Figure 3.3 through 3.6, it is natural to conjecture that the non-monotonicity in $\hat{\phi}_0$ itself contributes. In particular, neither of the functions $\exp(-\frac{(|k|-20)^2}{70})$ and $\frac{1+k^2}{100+k^{10}}$ is monotonic in $|k|$, while $\exp(-\frac{k^2}{70})$ and $\frac{1}{100+k^{10}}$ are monotonic and no "breathing" is observed for these two cases. Moreover, the definition for breathing above can be extended to define "multiple breathing", when $P_{\bar{T}}(\bar{T}=0)$ has multiple temporal extrema $t_i^*, i = 1, 2, \cdots$. In fact, we have seen *double breathing*, where $P_{\bar{T}}(\bar{T}=0)$ has two temporal maxima, if we set $\hat{\phi}_0$ to be quad-modal, for example, in the form of $\exp(-\frac{(|k|-M_1)^2}{V_1}) + R\exp(-\frac{(|k|-M_2)^2}{V_2})$, for some values of M_1, M_2, V_1, V_2 and R. This further supports the conjecture that breathing is caused by the non-monotonicity of $\hat{\phi}_0$ and the number of temporal maxima in $P_{\bar{T}}(\bar{T}=0)$ is related to that of maxima in $\hat{\phi}_0(k)$ with respect to $|k|$. In fact, Figure 3.7 suggests the fundamental difference between the ensuing two-point correlation functions for the initial data in the physical domain:

$$R(r) = \frac{\Big\langle T_0(y)\, T_0(y+r)\Big\rangle_W}{\sqrt{\langle T_0^2(y)\rangle_W \langle T_0^2(y+r)\rangle_W}} = \frac{\int_{-\infty}^{\infty} |k|^\alpha e^{2\pi i k r} \hat{\phi}_0^2(k) dk}{\int_{-\infty}^{\infty} |k|^\alpha \hat{\phi}_0^2(k) dk} \tag{3.22}$$

where there are multiple peaks in the correlation function for $\hat{\phi}_0(k) = \exp(-\frac{(|k|-20)^2}{70})$ while there is only one at $r = 0$ for $\hat{\phi}_0(k) = \exp(-\frac{k^2}{70})$.

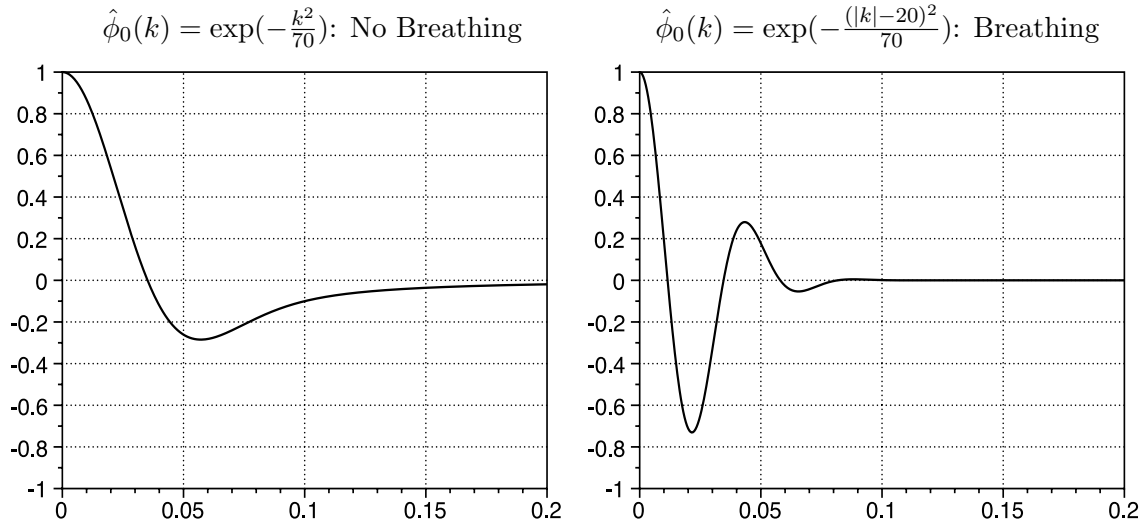

Figure 3.7: Two-Point Correlation Functions for Different $\hat{\phi}_0(k)$ where $\alpha = 1$. Horizontal Axis — r: Distance Between Two Points in Space. Vertical Axis — $R(r)$: Two-Point Correlation of the Initial Random Field

We also plotted the evolutions for $R(r)$ but they do not exhibit anything particularly intriguing. Therefore, the relationship between this multiply-peaked behavior and the breathing PDF is an open question and will be addressed in the future work.

3.3 Asymptotics of the Tracer PDF (3.15)

3.3.1 Core Behavior of $P_{\bar{T}}(\bar{T})$ ($\bar{T} \to 0$)

It is known from Section 3.1 that

$$P_{\bar{T}}(\bar{T}) = \frac{1}{\sqrt{2\pi}} \int_0^\infty \frac{e^{-\frac{\bar{T}^2}{2\sigma^2}} P_\eta(\eta)}{\sigma} d\eta \tag{3.23}$$

For $|\bar{T}| \ll 1$, we expand the exponential $e^{-\frac{\bar{T}^2}{2\sigma^2}}$ and a term-by-term integration leads to

$$P_{\bar{T}}(\bar{T}) = \sum_{n=0}^{\infty} \frac{(-1)^n \langle \sigma^{-2n-1} \rangle_\eta}{2^n \, n!} \, \bar{T}^{2n}, \quad \bar{T} \to 0 \tag{3.24}$$

given that $\langle \sigma^{-2n-1} \rangle_\eta = \int_0^\infty \sigma^{-2n-1} P_\eta(\eta) d\eta$ exists for $n = 0, 1, 2, \cdots$ and the above series converges. For smooth initial cut-off $\hat{\phi}_0$, (3.24) generally holds. In particular, for the invariant measure (3.21) where $\sigma \propto \eta^{-\frac{\alpha+1}{4}}$, $\langle \sigma^{-2n-1} \rangle_\eta$ exists for any n and its asymptotic approximation yields

$$\langle \sigma^{-2n-1} \rangle_\eta \sim n^{\frac{\alpha+1}{2}n + \frac{\alpha+1}{4}} e^{-\frac{\alpha+1}{2}n[1-2\ln 2+2\ln \pi - \ln(\alpha+1)]}, \quad n \to \infty \tag{3.25}$$

up to some constant factor as a function of α only. Therefore, (3.24) holds when $\alpha \leq 1$ and thus $P_{\bar{T}}(\bar{T})$ is analytic at $\bar{T} = 0$. Although the series fails to converge for $\alpha > 1$, it is still a valid *asymptotic* series and thus $P_{\bar{T}}(\bar{T})$ is always differentiable (derivative of any finite order exists) at $\bar{T} = 0$. To summerize, this essentially implies that the tail does *not* extend to the core, $\bar{T} = 0$, where the PDF is still Gaussian for its differentiability, since the stretched exponential form $Ae^{-B|\bar{T}|^{\frac{4}{3+\alpha}}}$ implies non-differentiability at $\bar{T} = 0$. Figure 3.8 illustrates the core and tail behavior of the invariant measure (3.21) for three different values of α, where the inset figures show the Gaussian behavior near the core. Notice that the widths of these Gaussian regions are on the order of 1, 10^{-3} and 10^{-6}, respectively, because of the fact that the expansion coefficients (3.25) are increasing with respect to α.

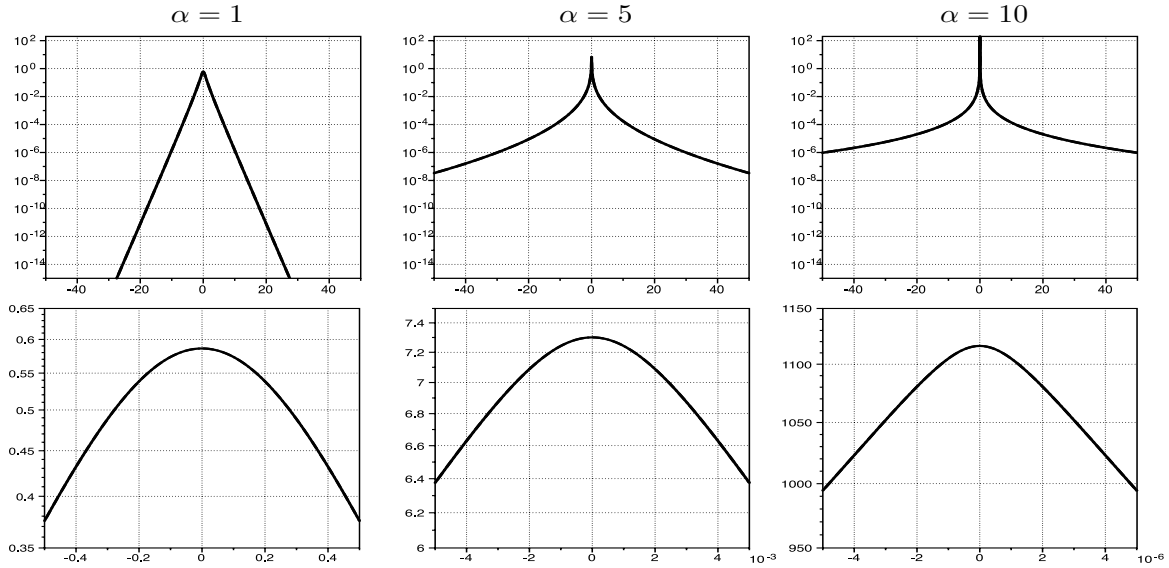

Figure 3.8: Tail and Core Behavior of the Invariant PDF (3.10) for Different α

However, when σ^{-1} grows faster in η than the decay rate (A.49) of $P_\eta(\eta)$ and thus $\langle \sigma^{-2n-1} \rangle_\eta$ diverges for $n \geq 0$, the tracer PDF is singular at the core $\bar{T} = 0$. Consequently, we would not be able to obtain the series expansion (3.24) in such a

case. An example will be given in Section 3.4 where $\hat{\phi}_0^2(k) = \delta(|k| - m)$ with the constant $M > 0$ so that

$$\sigma^{-1} = \frac{\exp(\frac{4\pi^2 m^2 t^2 \eta}{\mathrm{Pe}})}{(\cosh(4\pi m\sqrt{\frac{1}{\mathrm{Pe}}}\, t)^{\frac{1}{4}}}. \tag{3.26}$$

3.3.2 Long Time Asymptotics for $P_{\bar{T}}(\bar{T})$ in the Diffusionless Limit ($\mathrm{Pe} \to \infty$)

Now let's consider the scaling $t = (\mathrm{Pe})^\theta$ with $\theta > 0$ therefore $t \to \infty$ when $\mathrm{Pe} \to \infty$.

1. $\theta < \frac{1}{2}$. Substitute the scaling ansatz in (3.12), (3.13) and (3.14) and we have

$$\begin{aligned} \sigma^2 &= \frac{\int_{-\infty}^{\infty} |k|^\alpha \hat{\phi}_0^2(k) e^{-8\pi^2 k^2[(\mathrm{Pe})^{\theta-1} + (\mathrm{Pe})^{2\theta-1}\eta]} dk}{\int_{-\infty}^{\infty} \frac{|k|^\alpha \hat{\phi}_0^2(k) e^{-8\pi^2 k^2 (\mathrm{Pe})^{\theta-1}\eta}}{\sqrt{\cosh(4\pi\sqrt{(\mathrm{Pe})^{2\theta-1}}k)}} dk} \\ &\to \frac{\int_{-\infty}^{\infty} |k|^\alpha \hat{\phi}_0^2(k) dk}{\int_{-\infty}^{\infty} |k|^\alpha \hat{\phi}_0^2(k) dk} = 1 \end{aligned} \tag{3.27}$$

   as $\mathrm{Pe} \to \infty$ since in this limit, both $(\mathrm{Pe})^{\theta-1}$ and $(\mathrm{Pe})^{2\theta-1}$ vanish. Therefore

$$P_{\bar{T}}(\bar{T}) \sim \frac{1}{\sqrt{2\pi}} e^{-\frac{\bar{T}^2}{2}} \int_{-\infty}^{\infty} P_\eta(\eta) d\eta = \frac{1}{\sqrt{2\pi}} e^{-\frac{\bar{T}^2}{2}} \tag{3.28}$$

   and $\bar{T}$ remains asymptotically a Gaussian Random Field in this time scale. It is also clear that in this limit, effectively the diffusion is neglected and the random advection doesn't change the initial statistical distribution of the tracer.

2. $\theta > \frac{1}{2}$. First we consider the case where $\frac{1}{2} < \theta < 1$. In this time scale, $t/\mathrm{Pe} = (\mathrm{Pe})^{\theta-1} \to 0$ and $t^2/\mathrm{Pe} = (\mathrm{Pe})^{2\theta-1} \to \infty$ as $\mathrm{Pe} \to \infty$. And therefore

$$\begin{aligned} \sigma^2 &\to \frac{\int_{-\infty}^{\infty} |k|^\alpha \hat{\phi}_0^2(k) e^{-8\pi^2 k^2 (\mathrm{Pe})^{2\theta-1}\eta} dk}{\int_{-\infty}^{\infty} \frac{|k|^\alpha \hat{\phi}_0^2(k)}{\sqrt{\cosh(4\pi\sqrt{(\mathrm{Pe})^{2\theta-1}}k)}} dk} \\ &\to \frac{\Gamma(\frac{\alpha+1}{2})}{2^{\frac{\alpha+4}{2}}\Gamma(\alpha+1) \sum_{n=0}^{\infty} \frac{\binom{-1/2}{n}}{(4n+1)^{\alpha+1}}}\, \eta^{-\frac{\alpha+1}{2}} \\ &= [C(\alpha)\, \eta^{\frac{\alpha+1}{2}}]^{-1} \end{aligned} \tag{3.29}$$

by applying the Watson's Lemma. Furthermore, It is a very similar calculation to generalize this result for the case where $\theta \geq 1$. Substituting σ^2 in (3.15) with its asymptotic approximation (3.29) and we arrive at the formula (3.21). Furthermore, noticing the fact that $P_\eta(\eta) \sim \frac{1}{2\sqrt{\pi\eta^3}}\, e^{-\frac{1}{8\eta}}$ as $\eta \to 0$, for large $\bar{T}$

$$P_{\bar{T}}(\bar{T}) \sim \frac{\sqrt{C(\alpha)}}{2\sqrt{2}\,\pi} \int_0^\varepsilon \eta^{\frac{\alpha+1}{4}-\frac{3}{2}} e^{-\frac{\bar{T}^2}{2}C(\alpha)\eta^{\frac{\alpha+1}{2}}-\frac{1}{8\eta}} d\eta \tag{3.30}$$

for a small, fixed ε. To determine where this integral is dominated, we can solve the equation

$$\psi'(\eta) = \frac{d}{d\eta}\Big(\bar{T}^2 C(\alpha)\eta^{\frac{\alpha+1}{2}} + \frac{1}{8\eta}\Big) = 0 \tag{3.31}$$

and we have $\eta = \tilde{C}(\alpha)|\bar{T}|^{-\frac{4}{3+\alpha}}$. Then the change of variable in $\eta = s|\bar{T}|^{-\frac{4}{3+\alpha}}$ in (3.30) leads to

$$P_{\bar{T}}(\bar{T}) \sim |\bar{T}|^{-\frac{\alpha-1}{\alpha+3}} \int_0^\infty s^{\frac{\alpha-1}{4}} e^{-|\bar{T}|^{\frac{4}{3+\alpha}} D(s)} ds \tag{3.32}$$

where the function $D(s)$ achieves its minimum at $s = 1$. This is a standard Laplace integral and its asymptotic expansion reads

$$P_{\bar{T}}(\bar{T}) \sim A(\alpha)|\bar{T}|^{-\frac{\alpha+1}{\alpha+3}} e^{-B(\alpha)|\bar{T}|^{\frac{4}{\alpha+3}} + o(|\bar{T}|^{\frac{4}{\alpha+3}})}, \quad |\bar{T}| \to \infty \tag{3.33}$$

where A and B are constant functions of α only. Thus, this PDF has a stretched exponential tail, which is exactly the one recovered in previous work (Bronski and McLaughlin, 1997; Bronski and McLaughlin, 2000a; Vanden-Eijnden, 2001), namely, the measure (3.10). But the significance of the above analysis lies in the distinguished scaling between t and Pe it reveals.

3. $\theta = \frac{1}{2}$. In this critical time scale,

$$\sigma^2 \to \frac{\int_{-\infty}^{\infty} |k|^\alpha \hat{\phi}_0^2(k) e^{-8\pi^2 k^2 \eta} dk}{\int_{-\infty}^{\infty} \frac{|k|^\alpha \hat{\phi}_0^2(k)}{\sqrt{\cosh(4\pi k)}}\, dk} \tag{3.34}$$

The ensuing PDF (3.23) is special in the sense that we cannot further approximate the conditional variance and it suggests nontrivial dependence on the initial cut-off function, $\hat{\phi}_0(k)$. And the numerical results, shown in Figure 3.9, suggest that this scaling, $t = \sqrt{\mathrm{Pe}}$ and $\mathrm{Pe} \to \infty$, corresponds to the "breathing" PDF we described in Section 3.2. Here the initial Gaussian ($t = 0$) and the invariant

measure (3.33) ($t = \text{Pe}$ and $\text{Pe} \to \infty$) are also plotted as comparison. Therefore, this is a *new* long time, invariant measure in the diffusionless limit, different than the measure (3.33) and its existence is completely determined by the initial cut-off function $\hat{\phi}_0$. In particular, when breathing occurs for $\hat{\phi}_0(k) = e^{-\frac{(|k|-20)^2}{70}}$, for some intermediate values of $\bar{T}$, the measure has a larger concavity than the initial Gaussian and the measure (3.33), and $P_{\bar{T}}(0)$ is largest when $t = \sqrt{\text{Pe}}$ and $\text{Pe} \to \infty$, which is consistent with the characteristics discussed in Section 3.2.

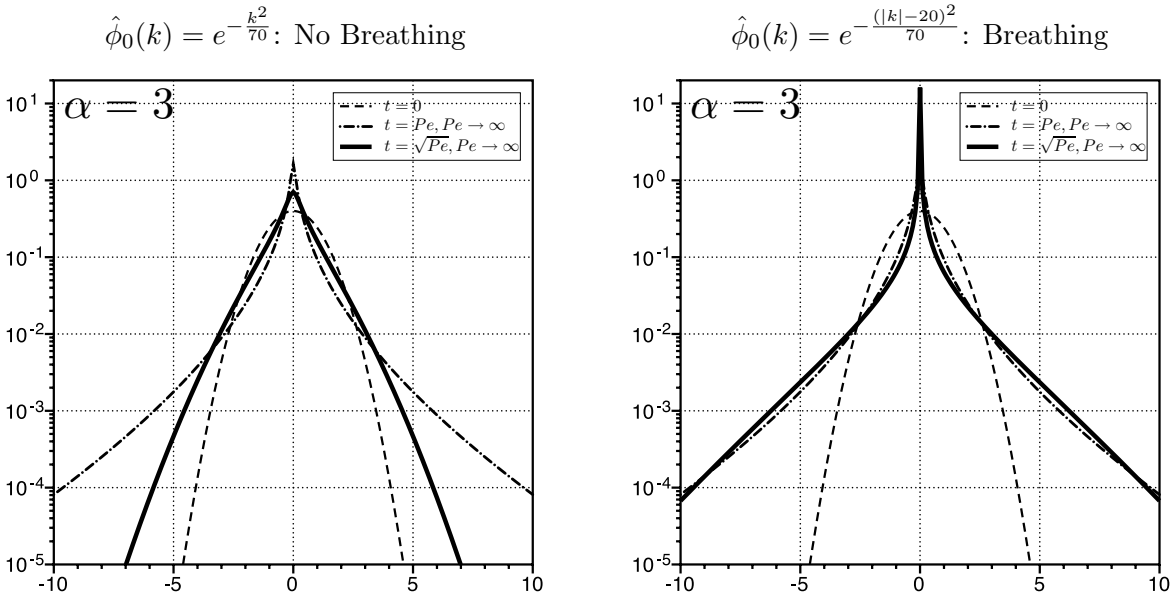

Figure 3.9: New Long Time, Invariant Measure in the Diffusionless Limit

Moreover, the anomalies in the PDF concavity and the zero fluctuation density, $P_{\bar{T}}(0)$, together change the relationship between the new invariant measure and the invariant measure (3.10): as $|\bar{T}|$ increases from 0, the new invariant measure exhibits "larger→smaller→ larger→smaller" behavior compared to the measure (3.33), when breathing occurs in the right panel; whereas in the left, the transition has only three phases, smaller→larger→ smaller. This adds another characterization of the breathing phenomena which can also be inferred from Figure 3.4, although the phase where the breathing PDF is smaller than the invariant measure in the tails is not shown.

Next we study the tail asymptotics of the tracer PDF in this regime and see if it is different from Gaussian and the stretched exponential (3.33). First consider the special case when $\hat{\phi}_0(k) = \exp(-\frac{\pi^2 k^2}{2V})$ with V as a constant determining the spread of the random spectrum of the initial random field. Then (3.34) can be

simplified as $\sigma^2 \to (A+B\eta)^{-\frac{\alpha+1}{2}}$ as $\mathrm{Pe} \to \infty$ where

$$\begin{aligned} A &= A(V,\alpha) = \pi^2 V^{-1}\Big(\int_{-\infty}^{\infty} \frac{|k|^\alpha \hat{\phi}_0^2(k)}{\sqrt{\cosh(4\pi k)}}\, dk\Big)^{\frac{2}{\alpha+1}}, \\ B &= B(\alpha) = 8\pi^2\Big(\int_{-\infty}^{\infty} \frac{|k|^\alpha \hat{\phi}_0^2(k)}{\sqrt{\cosh(4\pi k)}}\, dk\Big)^{\frac{2}{\alpha+1}}. \end{aligned} \tag{3.35}$$

By letting $k = \frac{B}{A}\eta = 8V\eta$, we claim that for large $|\bar{T}|$,

$$\begin{aligned} P_{\bar{T}}(\bar{T}) &\sim \frac{A^{\frac{\alpha+1}{4}}}{2\sqrt{2}\,\pi}\int_0^{\varepsilon} \sqrt{\frac{(1+8V\eta)^{\frac{\alpha+1}{2}}}{\eta^3}}\, \exp\Big(-\frac{\bar{T}^2 A^{\frac{\alpha+1}{2}}}{2}(1+8V\eta)^{\frac{\alpha+1}{2}} - \frac{1}{8\eta}\Big)d\eta \\ &\sim \frac{A^{\frac{\alpha+1}{4}}\sqrt{V}}{\pi}\int_0^{\varepsilon} \sqrt{\frac{(1+k)^{\frac{\alpha+1}{2}}}{k^3}}\, \exp\Big[-x(1+k)^{\frac{\alpha+1}{2}} - \frac{V}{k}\Big]dk \end{aligned} \tag{3.36}$$

where $x = \frac{\bar{T}^2 A^{\frac{\alpha+1}{2}}}{2}$. Here, $\varepsilon \ll 1$ is fixed so that $P_\eta(\eta) \sim \frac{1}{2\sqrt{\pi\eta^3}}\, e^{-\frac{1}{8\eta}}$ when $\eta \le \varepsilon$. We prove this by showing that

$$\int_{\varepsilon}^{\infty} \sqrt{(1+k)^{\frac{\alpha+1}{2}}}\, \exp\Big[-x(1+k)^{\frac{\alpha+1}{2}}\Big] P_\eta(\frac{k}{8V})dk \sim D(\alpha)e^{-x(1+\varepsilon)^{\frac{\alpha+1}{2}}}, \tag{3.37}$$

is sub-dominant compared to (3.36) from the following asymptotic expansion of thd Laplace integral with a movable maximum

$$\begin{aligned} &\int_0^{\varepsilon} \sqrt{\frac{(1+k)^{\frac{\alpha+1}{2}}}{k^3}}\, \exp\Big[-x(1+k)^{\frac{\alpha+1}{2}} - \frac{V}{k}\Big]dk \\ =\;& e^{-x}\int_0^{\varepsilon} \sqrt{\frac{(1+k)^{\frac{\alpha+1}{2}}}{k^3}}\, \exp\Big(-x[(1+k)^{\frac{\alpha+1}{2}} - 1] - \frac{V}{k}\Big)dk \\ \sim\;& M\sqrt{\frac{2\pi}{-\phi''(1)}}\, e^{\phi(1)}\Big(f(1) - \frac{f''(1)}{2\phi''(1)} + \frac{f(1)\phi^{(4)}(1)}{8[\phi''(1)]^2} \\ &+\frac{f'(1)\phi'''(1)}{2[\phi''(1)]^2} - \frac{5f(1)[\phi'''(1)]^2}{24[\phi''(1)]^3}\Big) \end{aligned} \tag{3.38}$$

where $f(s) = (sM)^{-\frac{3}{2}}(1+sM)^{\frac{\alpha+1}{4}}$, $\phi(s) = -x(1+sM)^{\frac{\alpha+1}{2}} - \frac{V}{sM}$ and $M = M(x,\alpha,V)$ is a root of the algebraic equation for k

$$\frac{\partial}{\partial k}\Big(-x(1+k)^{\frac{\alpha+1}{2}} - \frac{V}{k}\Big) = 0 \tag{3.39}$$

that is close to 0. Naturally, for this argument to hold, x needs to be large enough so that $M < \varepsilon$. Although the closed-form expression for M is not available, its asymptotic expansion can be obtained by solving Eq. (3.39) perturbatively

$$M(x,\alpha,V) = \sqrt{\frac{2V}{(\alpha+1)x}}\Big(1+\frac{1-\alpha}{4}\sqrt{\frac{2V}{(\alpha+1)x}}+\frac{2V(\alpha-1)(3\alpha+1)}{32(\alpha+1)x}\Big)+O(x^{-2}) \tag{3.40}$$

with which the integral (3.36) can be asymptotically expanded as

$$P_{\bar{T}}(\bar{T}) \sim \frac{\sqrt{\tilde{A}}}{e^{\frac{V(\alpha-1)}{4}}\sqrt{\pi}} e^{-\frac{\tilde{A}}{2}\bar{T}^2-\sqrt{\tilde{A}V(\alpha+1)}\,|\bar{T}|}\Big(1+\frac{(\alpha+3)\sqrt{2V}}{48\sqrt{(\alpha+1)x}}[6+V(\alpha-1)]\Big) \tag{3.41}$$

when $|\bar{T}| \to \infty$ and $\tilde{A} = A^{\frac{\alpha+1}{2}}$. Thus, this PDF still has a Gaussian tail, although it is different than that of the unit Gaussian at $t = 0$. Although the explicit formula for σ^2 is not available when $\hat{\phi}_0(k) = e^{-\frac{(|k|-20)^2}{70}}$, which is more relevant to the breathing phenoma, numerical results suggest that the induced PDF also has Gaussian tails similar to (3.41).

3.3.3 Tail Asymptotics for $P_{\bar{T}}(\bar{T})$ ($\bar{T} \to \infty$) at large times for finite, non-zero Pe

It has been noted by Bronski, McLaughlin (Bronski and McLaughlin, 1997; Bronski and McLaughlin, 2000a) and Vanden-Eijnden (Vanden-Eijnden, 2001) that at finite time for fixed Pe $\neq 0$, the tails of the renormalized scalar PDF in the Majda Model are Gaussian with outward propagating non-Gaussianity, in particular, the stretched exponential regime (3.10). Here we provide a crisp estimate of the speed of such propagation, as a function of time.

Letting $\beta = \frac{\alpha+1}{2} > 0$, a similar calculation as in (3.29) reads

$$\sigma^2 \sim [\widetilde{C}(\beta)(\eta+\frac{1}{t})^{\beta}]^{-1} \tag{3.42}$$

for finite, non-vanishing Pe, where

$$\widetilde{C}(\beta) = C(\alpha) = \frac{2^{\frac{\alpha+4}{2}}\Gamma(\alpha+1)}{\Gamma(\frac{\alpha+1}{2})}\sum_{n=0}^{\infty}\binom{-\frac{1}{2}}{n}\frac{1}{(4n+1)^{\alpha+1}} \tag{3.43}$$

Therefore, in this case

$$P_{\bar{T}}(\bar{T}) \sim \frac{\sqrt{\widetilde{C}(\beta)}}{2\sqrt{2}\,\pi} \int_0^{\varepsilon} \sqrt{\frac{(\eta+\frac{1}{t})^{\beta}}{\eta^3}} \exp\Big[-\frac{\bar{T}^2}{2}\widetilde{C}(\beta)(\eta+\frac{1}{t})^{\beta} - \frac{1}{8\eta}\Big] d\eta \tag{3.44}$$

for large $|\bar{T}|$. Notice that there are two large parameters in (3.44), namely, the magnitude of the renormalized tracer, $|\bar{T}|$ and the time, t. If we first let t go to infinity, then (3.44) formally reduces to (3.30) and this corresponds to the tail asymptotics of the long time, stationary tracer PDF with finite diffusivity, $\frac{1}{\mathrm{Pe}}$ (Bronski, 2003; Vanden-Eijnden, 2001). In other words, in the $\frac{1}{t}$-$\frac{1}{|\bar{T}|}$ phase plane, this limiting procedure is equivalent to approaching the origin along the $\frac{1}{|\bar{T}|}$-axis.

Alternatively, next we consider the singular limit along the curve $\widetilde{C}(\beta)|\bar{T}|^2 = 2t^{2\gamma}$ with $\gamma > 0$. Then (3.44) becomes

$$P_{\bar{T}}(\bar{T}) \sim \frac{\sqrt{\widetilde{C}(\beta)}}{2\sqrt{2}\,\pi}\, e^{-t^{2\gamma-\beta}} \int_0^{\varepsilon} \sqrt{\frac{(\eta+\frac{1}{t})^{\beta}}{\eta^3}} \exp\Big\{ -t^{2\gamma-\beta}[(t\eta+1)^{\beta}-1] - \frac{1}{8\eta}\Big\} d\eta \tag{3.45}$$

Again, this is a Laplace integral with a movable maximum and we have to solve the algebraic equation

$$\frac{\partial}{\partial\eta}\Big\{ t^{2\gamma-\beta}[(t\eta+1)^{\beta}-1] + \frac{1}{8\eta}\Big\} = 0 \tag{3.46}$$

to determine where the dominant contribution localizes near $\eta = 0$. Next we consider two different cases:

Case 1: $2\gamma - \beta \le 1$, or equivalently, $\gamma \le \frac{\beta+1}{2} = \frac{\alpha+3}{4}$. In this case, using the Method of Dominant Balance for $\gamma < \frac{\beta+1}{2}$, we have

$$\eta \sim (8\beta)^{-\frac{1}{1+\beta}} t^{-\frac{2\gamma}{1+\beta}} \tag{3.47}$$

since $t\eta \propto t^{\frac{\beta-2\gamma+1}{1+\beta}} \gg 1$ when t is large. Moreover, this result also applies when $\gamma = \frac{\beta+1}{2}$ and thus $t\eta = O(1)$. Then the change of variable $\eta = s(8\beta)^{-\frac{1}{1+\beta}} t^{-\frac{2\gamma}{1+\beta}}$ reproduces very similar calculations as in (3.30) through (3.33) and the result reads

$$P_{\bar{T}}(\bar{T}) \sim A_1(\alpha,\gamma)|\bar{T}|^{-\frac{\alpha+1}{\alpha+3}} e^{-B_1(\alpha,\gamma)|\bar{T}|^{\frac{4}{\alpha+3}} + o(|\bar{T}|^{\frac{4}{\alpha+3}})} \tag{3.48}$$

for $|\bar{T}|$ large, where $A_1(\alpha,\gamma)$ and $B_1(\alpha,\gamma)$ are functions of α and γ alone.

Notice that here $|\bar{T}|^{\frac{4}{\alpha+3}} = t^{\frac{2\gamma}{1+\beta}} \geq t^{2\gamma-\beta}$ and therefore the $e^{-t^{2\gamma-\beta}}$ term in the prefactor of (3.45) doesn't affect the asymptotic result (3.48).

Case 2: $2\gamma - \beta > 1$, or equivalently, $\gamma > \frac{\alpha+3}{4}$. In this case, solving Eq. (3.46) implies

$$\eta \sim \frac{1}{\sqrt{8\beta}} t^{\frac{\beta-1}{2}-\gamma} \tag{3.49}$$

since here $t\eta \propto t^{1-\gamma+\frac{\beta-1}{2}} \ll 1$ when t is large. And thus the asymptotic approximation to (3.45) reads

$$P_{\bar{T}}(\bar{T}) \sim A_2(\alpha,\gamma)\bar{T}^{\frac{1}{2}-\frac{1+3\alpha}{8\gamma}} e^{-B_2(\alpha,\gamma)|\bar{T}|^{2-\frac{\alpha+1}{2\gamma}}+o(|\bar{T}|^{2-\frac{\alpha+1}{2\gamma}})}, \qquad |\bar{T}| \to \infty. \tag{3.50}$$

This is also "heavier" than Gaussian, since $\alpha + 1 > 0$, but "lighter" than the stretched exponential shown in (3.48).

The results (3.48) and (3.50) suggest that as time advances, the the stretched exponential regime in the renormalized tracer PDF propagates towards the tail of the PDF at a critical, algebraic rate proportional to $t^{\frac{\alpha+3}{4}}$. However, for the values of $|\bar{T}|$ growing in an faster algebraic rate with respect to time, the corresponding region in the PDF also exhibits heavi-tailed behavior, which is an intermediate state between Gaussian and the tail behavior of the long time, stationary PDF.

3.4 Discussion of the Condition for the "Breathing"

As we saw in the numerical results in Section 3.2, the "breathing" phenomena is characterized by the non-monotonic behavior of the renormalized tracer PDF in time. And we further defined that $P_{\bar{T}}(\bar{0})$ has at least one temporal extrema at finite time when a "breathing" occurs. Moreover, the initial cut-off function $\hat{\phi}_0$ contributes in determining the occurrence since we don't observe "breathing" if $\hat{\phi}_0$ is a uni-modal Gaussian using the same set of parameter values. As we have seen in Section 3.3, this dependence on the initial cut-off function can also be revealed through proper asymptotic limiting procedure.

From the difference between the two types of $\hat{\phi}_0$ we choose, it is natural to conjecture that the temporal non-monotonicity of the PDF might be related to the non-monoticity of $\hat{\phi}_0(k)$ as $|k|$ varies. However, the analysis for the relationship between these two is very complicated for general $\hat{\phi}_0(k)$, with the integral forms of the variances and $P_\eta(\eta)$ in

Section 3.1. Therefore in this section, we illustrate how "breathing" can be established by choosing $\hat{\phi}_0(k)$ to be related to Dirac delta functions so that the variance (3.14) has explicit, closed form expressions. From Section 3.1, we can derive that

$$\begin{aligned}\frac{\partial}{\partial t}P_{\bar{T}}(\bar{T}) &= \frac{1}{\sqrt{2\pi}}\int_0^\infty \frac{\partial}{\partial t}\Big(\frac{e^{-\frac{\bar{T}^2}{2\sigma^2}}}{\sigma}\Big)P_\eta(\eta)d\eta \\ &= \frac{1}{2\sqrt{2\pi}}\int_0^\infty \frac{e^{-\frac{\bar{T}^2}{2\sigma^2}}}{\sigma^5}(\bar{T}^2-\sigma^2)\frac{\partial}{\partial t}(\sigma^2)P_\eta(\eta)d\eta\end{aligned} \tag{3.51}$$

Clearly, if $\frac{\partial}{\partial t}(\sigma^2)$ is sign definite for any t and η, then so is $\frac{\partial}{\partial t}P_{\bar{T}}(0)$ and thus $P_{\bar{T}}(0)$ is monotonic. Similarly, since $\sigma^2(t,\eta) \le \sigma^2(t,0)$, for $|\bar{T}| \ge \sigma(t,0)$ from (3.12), uniform monotonicity of σ^2 also implies the monotonicity of $P_{\bar{T}}(\bar{T})$. In fact, as we will see in Section 3.3, $\sigma^2 \propto (\eta+\frac{1}{t})^{-\frac{\alpha+1}{2}}$ when t is large enough and therefore σ^2 is monotonically increasing for large times. Consequently, $P_{\bar{T}}(0)$ is decreasing and the tails of the PDF are increasing, monotonically. Of course, it is too restrictive to impose uniform monotonicity on σ^2 for general t and η and from above figures, $P_{\bar{T}}(0)$ attains a temporal, local maximum when breathing occurs while it is monotonically increasing if there's no breathing. To illustrate how such monotonicity in $P_{\bar{T}}(0)$ can be established, let us first consider the special case for $\bar{T}=0$, since from above figures, $P_{\bar{T}}(0)$ is monotonically increasing if there's no breathing while it attains a temporal, local maximum when breathing occurs. Further, we consider a simple example by using the initial cutoff function $\hat{\phi}_0^2(k) = \delta(|k|-m)$ with the constant $m>0$ so that $\sigma^2(t,\eta) = \big[\cosh(4\pi mt\sqrt{\frac{1}{\mathrm{Pe}}})\big]^{-\frac{1}{2}}\exp(-\frac{8\pi^2m^2t^2\eta}{\mathrm{Pe}})$, which can be easily verified from the definitions (3.12), (3.13) and (3.14). Then to show that $P_{\hat{T}}(0)$ is constantly increasing, it suffices to show that

$$\int_0^\infty e^{\xi\eta}(\eta-\frac{1}{2})P_\eta(\eta)d\eta > 0 \tag{3.52}$$

for any $\xi>0$ since in this case

$$\begin{aligned}\frac{\partial}{\partial t}P_{\bar{T}}(0) &= \frac{1}{\sqrt{2\pi}}\int_0^\infty \frac{\partial}{\partial t}\Big(\frac{1}{\sigma}\Big)P_\eta(\eta)d\eta \\ &= \frac{\xi}{t\sqrt{2\pi\sqrt{\cosh(2\sqrt{\xi})}}}\int_0^\infty e^{\xi\eta}\Big(\eta-\frac{\tanh(2\sqrt{\xi})}{4\sqrt{\xi}}\Big)P_\eta(\eta)d\eta \\ &\ge \frac{\xi}{t\sqrt{2\pi\sqrt{\cosh(2\sqrt{\xi})}}}\int_0^\infty e^{\xi\eta}\Big(\eta-\frac{1}{2}\Big)P_\eta(\eta)d\eta\end{aligned} \tag{3.53}$$

with $\xi = 4\pi^2 M^2 \frac{1}{\mathrm{Pe}} t^2 > 0$. To prove (3.52), one only needs to realized

$$\int_0^\infty e^{\xi\eta}(\eta - \frac{1}{2})P_\eta(\eta)d\eta > e^{\xi/2}\int_0^\infty (\eta - \frac{1}{2})P_\eta(\eta)d\eta = 0 \tag{3.54}$$

since

$$\int_0^\infty \eta P_\eta(\eta)d\eta = \langle\eta\rangle = -\frac{\partial}{\partial s}\frac{1}{\sqrt{\cosh\sqrt{2s}}}\Big|_{s=0} = \frac{1}{2} \tag{3.55}$$

Next we consider a slightly different type of cut-off function with energy spectrum concentrated at two wavenumbers, namely,

$$\hat{\phi}_0^2(k) = \delta(|k| - m) + R\delta(|k| - cm) \tag{3.56}$$

for which we observed breathing for some combinations of values of positive constants m, c and R. In this case, the explicit formula for the conditional variance is also available via

$$\sigma^2(\eta, t) = \frac{e^{-2M^2(t+t^2\eta)} + Rc^\alpha e^{-2c^2M^2(t+t^2\eta)}}{\frac{e^{-2M^2t}}{\sqrt{\cosh(2Mt)}} + Rc^\alpha\frac{e^{-2c^2M^2t}}{\sqrt{\cosh(2cMt)}}} \tag{3.57}$$

with $M = \frac{2\pi m}{\sqrt{\mathrm{Pe}}}$. Thus,

$$\begin{aligned}\frac{\partial}{\partial t}\Big(\frac{1}{\sigma}\Big) \;=\; & \frac{M^2(1+2t\eta)[e^{-2M^2(t+t^2\eta)} + Rc^{\alpha+2}e^{-2c^2M^2(t+t^2\eta)}]}{\sigma(e^{-2M^2(t+t^2\eta)} + Rc^\alpha e^{-2c^2M^2(t+t^2\eta)})} \\ & -\frac{\sigma M^2\frac{e^{-2M^2t}}{\sqrt{\cosh(2Mt)}}(1 + \frac{\tanh(2Mt)}{2M})}{e^{-2M^2(t+t^2\eta)} + Rc^\alpha e^{-2c^2M^2(t+t^2\eta)}} \\ & -\frac{\sigma M^2 Rc^{\alpha+2}\frac{e^{-2c^2M^2t}}{\sqrt{\cosh(2cMt)}}(1 + \frac{\tanh(2cMt)}{2cM})}{e^{-2M^2(t+t^2\eta)} + Rc^\alpha e^{-2c^2M^2(t+t^2\eta)}}\end{aligned} \tag{3.58}$$

To reduce the complexity of exploring the four-dimensional (M, c, R, α) parameter space, we first take the asymptotic limit $c \to 0$ requiring finite $Rc^\alpha \equiv L > 0$, which implies that $R \to 0$ if $-1 < \alpha < 0$, $R \to \infty$ if $\alpha > 0$ and $R \equiv 1$ if $\alpha = 0$. Thus, the conditional variance (3.57) is reduced to

$$\sigma^2(\eta, t) \to \frac{e^{-2M^2(t+t^2\eta)} + L}{\frac{e^{-2M^2t}}{\sqrt{\cosh(2Mt)}} + L}, \qquad c \to 0. \tag{3.59}$$

With this expression for σ^2, the numerical integration shows that the breathing phenomena occurs at a time scale proportional to $\frac{1}{M^2}$ for large M and thus we next study the large M asymptotics of

$$\frac{\partial}{\partial t}P_{\bar{T}}(0) = \frac{1}{\sqrt{2\pi}}\int_0^\infty \frac{\partial}{\partial t}\left(\frac{e^{-2M^2(t+t^2\eta)}+L}{\frac{e^{-2M^2t}}{\sqrt{\cosh(2Mt)}}+L}\right)^{-\frac{1}{2}} P_\eta(\eta)d\eta \tag{3.60}$$

at $t = \frac{l}{M^2}$ with some constant $l > 0$, to quantitatively identify the "breathing", the non-monotonic behavior of the tracer PDF. After some algebra, (3.60) is expanded into

$$\frac{\partial}{\partial t}P_{\bar{T}}(0)\Big|_{t=\frac{l}{M^2}} = \frac{Me^{-l}}{2\sqrt{2\pi\Big(e^{-2l}+L\sqrt{\cosh\frac{2l}{M}}\Big)}}\sum_{i=1}^{3} g_i(M)\int_0^\infty h\Big(\frac{\eta}{M^2}\Big)f_i\Big(\frac{\eta}{M^2}\Big)P_\eta(\eta)d\eta \tag{3.61}$$

where $h = e^{\frac{l^2\eta}{M^2}}\Big(1+Le^{2l(1+\frac{l\eta}{M^2})}\Big)^{-\frac{3}{2}}$ and

$$\begin{array}{lll} g_1 = 2MLe^{2l}\sqrt{\cosh\frac{2l}{M}}, & g_2 = 2M, & g_3 = -\tanh\frac{2l}{M}, \\ f_1 = 1+\frac{2l\eta}{M^2}, & f_2 = \frac{2l\eta}{M^2} - Le^{2l(1+\frac{l\eta}{M^2})}, & f_3 = 1+Le^{2l(1+\frac{l\eta}{M^2})}. \end{array} \tag{3.62}$$

We observe that $hf_i, i = 1,2,3$ are all smooth, bounded functions on $[0,\infty]$. Thus we can expand each of them into a power series of $\frac{\eta}{M^2}$, followed by a term-by-term integration to evaluate each of the three integrals in (3.61) utilizing

$$\begin{aligned} \int_0^\infty \Big(\frac{\eta}{M^2}\Big)^n P_\eta(\eta)d\eta &= M^{-2n}\langle\eta^n\rangle \\ &= (-1)^n n! M^{-2n}\frac{\partial^n}{\partial s^n}\frac{1}{\sqrt{\cosh\sqrt{2s}}}\Big|_{s=0}. \end{aligned} \tag{3.63}$$

In fact, the above analysis can be generalized to $\bar{T} \neq 0$ and ultimately we have

$$\frac{\partial}{\partial t}P_{\bar{T}}(\bar{T})\Big|_{t=\frac{l}{M^2}} = \frac{l^3 e^{-\frac{\bar{T}^2}{2}}[1+L(1-l)e^{2l}](3-6\bar{T}^2+\bar{T}^4)}{3\sqrt{2\pi}\,(1+Le^{2l})^3}M^{-2} + O(M^{-4}), \tag{3.64}$$

for $M \to \infty$. Therefore, for large M, the sign of $\frac{\partial}{\partial t}P_{\bar{T}}(\bar{T})$ is determined by that of $[1+L(1-l)e^{2l}](3-6\bar{T}^2+\bar{T}^4)$. Moreover, it is straightforward to see that the equation $1+L(1-l)e^{2l} = 0$ has one and only one positive root $l^* = l^*(L)$ for fixed $L > 0$, which in turn suggests that with the cut-off function (3.56), breathing will occur around

$t = t^* = M^{-2}l^*(L) = M^{-2}l^*(Rc^\alpha)$ for large M in the limit $c \to 0$ and $Rc^\alpha \equiv L$. In particular, for $\bar{T}^2 \in [0, 3-\sqrt{6}) \bigcap (3+\sqrt{6}, \infty)$, $P_{\bar{T}}(\bar{T})$ has exactly one temporal maximum; otherwise, $P_{\bar{T}}(\bar{T})$ has exactly one temporal minimum.

3.5 Self-Averaging and Semi-Ergodicity

As we saw in (3.9), the solution for the Majda Model (3.1) inherits the randomness from two independent sources: 1) the initial Gaussian random field, represented in $dW(k)$ and 2) the random shear, represented in $\xi(t)$. And by the analyses discussed above, we obtain a comprehensive illustration of the statistical distribution of single-point tracer. Alternatively, an interesting, practical question one might ask is that in reality, can we extract the same distribution from a single realization of the initial field and/or a single realization of the random shear? For example, through such question concerning ergodicity, it would be useful to know if the ensemble averages $\langle\cdot\rangle_W$ and $\langle\cdot\rangle_{W,\eta}$ can be replaced by spatial and spatio-temporal averages, respectively.

We seek the answer to the aforementioned question via Monte-Carlo simulations, whose procedure is discussed in details in our previous work (Camassa et al., 2006). Numerically, the ensemble average $\langle\cdot\rangle_W$ used in single point statistics were done by essentially discretizing and sampling different realizations of $dW(k)$ in the Fourier representation of T_0 in (3.1). Nonetheless, only one typical realization of $dW(k)$ can also reproduce the same empirical approximations (histograms) to the single-point tracer PDFs by binning on all the tracer values collected at different spatial locations. This feature not only greatly reduces the computation complexity of the Monte-Carlo simulations, which provides very accurate PDFs for the Majda Model, but also indicates the physical relevance of the model itself. For example, for a fixed history of $\gamma(t)$, the field remains Gaussian at any fixed time, as well as the single-point tracer statistics. This is shown in Figure 3.10, where a histogram of 200 uniform bins between $[-5, 5]$ is generated from 10^6 samples collected over $y \in [-500, 500]$ and it is compared with the single-point Monte-Carlo simulations for $T(0, 0, t)$ and the exact Gaussian with unit variance. Here the samples in the simulations are renormalized by the sample standard deviation, which is almost identical to the exact conditional standard deviation, the square root of $\langle T^2\rangle_W$ defined in (3.12). In fact, we will rigorously prove in the Appendix that the Majda model is spatially ergodic by showing that the spatial statistics converges in probability to the single-point ensemble statistics.

Next, we explore the possible equivalence of the full, joint ensemble average, $\langle\cdot\rangle_{W,\eta}$,

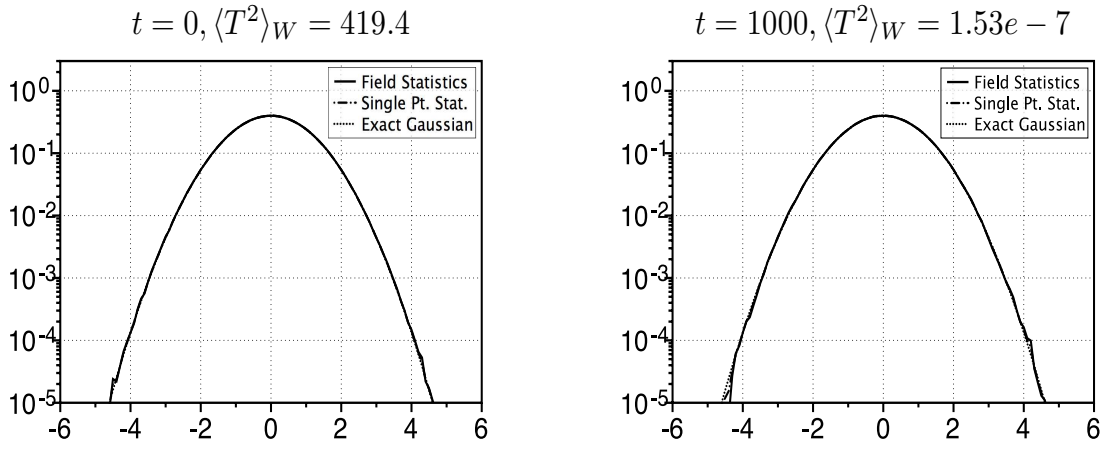

Figure 3.10: Conditional PDFs where $\alpha = 1$, $Pe = 10^5$ and $\hat{\phi}_0(k) = \exp(-\frac{(|k|-20)^2}{70})$

and the semi-empirical average, $\langle \cdot \rangle_{S,\eta}$, over the spatial locations with a single realization of the initial field and over an ensemble of histories of $\gamma(t)$. Results show that the field (spatial) statistics used in $\langle \cdot \rangle_{S,\eta}$ can also reproduce the heavy-tailed PDFs and breathing behavior we have seen for specific initial cutoffs in Figure 3.3: to generate an empirical histogram in each panel of Figure 3.11, 10^{12} joint statistical samples are obtained from a single realization of initial field using the parameters used above, which is then evolved by 10^6 realizations of the random shear.

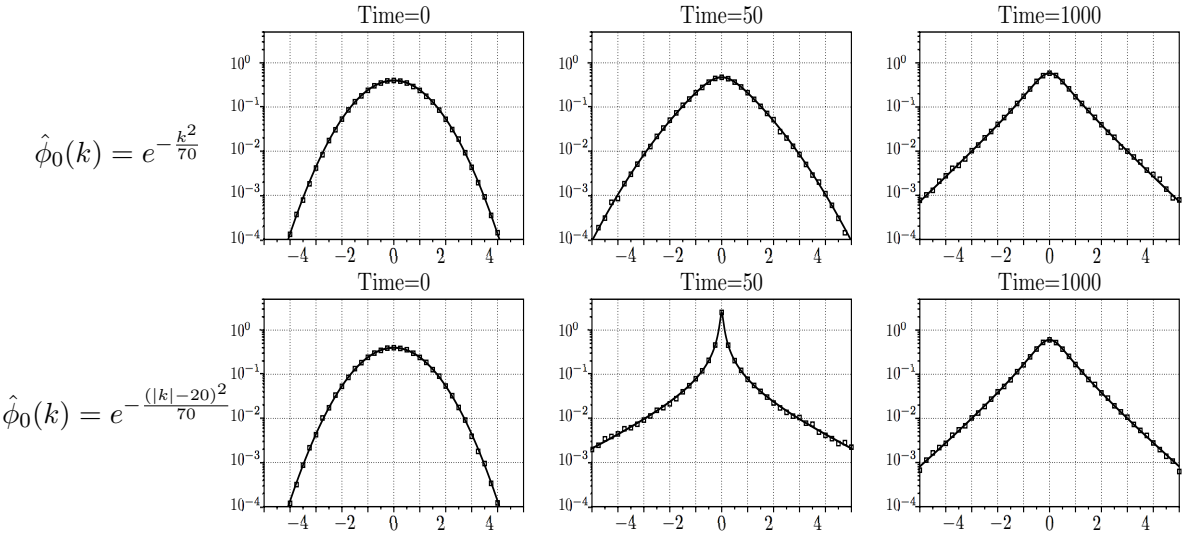

Figure 3.11: PDF for Different $\hat{\phi}_0(k)$ where $\alpha = 1$, Pe $= 10^5$ Obtained by Simulated Histogram of Spatial Samples in 10^6 Realizations of $\gamma(t)$ ($\square$) and Numerical Integration of Single-Point, Joint PDF (3.15) ($-$).

However, numerical evidence does not suggest that the model is "temporally" ergodic, or in other words, the ensemble statistics over the realizations of $\gamma(t), t > 0$ cannot be replace by temporal statistics on single realization of the random shear. In particular, we obtained neither the breathing PDFs, nor the invariant heavy-tailed distributions (3.10), by performing fully empirical statistics on the dynamical tracer field with a single realization of the initial field *and* a single realization of the random shear. To collect tracer samples for the full empirical statistics, we need to first discretize $T(x, y, t)$ in both space and time, then at each time step, renormalize the field with certain time scalings to compensate the effect of diffusion. Natural choices for the renormalized include the spatial tracer variance at fixed time, time scaling $\sqrt{t}$ for the pure diffusion, and the scaling $t^{\frac{\alpha+1}{2}}$ with the *a priori*, asymptotic analysis of the conditional variance (3.12). From this collection of renormalized tracer values, we obtain a "matrix" of samples, with each row being the spatially discretized tracer field at fixed time, and each column being the time series of a single-point tracer measurement. Nonetheless, we can not find statistical agreement between the histogram of this sample collection, and the joint ensemble PDF we studied in previous sections, regardless of the choice of renormalizations mentioned above. Therefore, we suspect that the probability measure of single-point tracer is not ergodic.

3.6 Conclusions

The integral formalism in this chapter presents a comprehensive picture of the evolution of the Majda model which had previously been only analyzed in the tail at long time, or from statistical moments. Through this formulation, we have documented a new breathing phenomena which occurs when there are multiple peaks in the initial scalar correlation function. This behavior is documented both numerically and analytically.

Further, we present a more detailed description of the invariant measure by establishing that it always has a Gaussian core which is distinguished from the stretched exponential tail in that the core is infinitely differentiable (but not necessarily analytic), whereas a pure stretched exponential distribution is not. Moreover, a joint distinguished limit of time and the Péclet number identifies breathing PDF as a new invariant measure. Additionally, we calculated the explicit rate of approach in time for the invariant heavy tail. Lastly, a class of special data is adopted to yield exact results that predict the occurrence of the breathing phenomena.

Future directions include the assessment of initial data possessing a non-trivial

mean as well as the exploration of multi-point and gradient statistics. Further Majda examined for finite moments the role of an additional deterministic linear shear layer (Majda, 1993b), and such flows may give rise to interesting transient dynamics in the PDF such as observed here.

Chapter 4

More Complicated Models

As mentioned in the Introduction, to obtain the full scalar probability measure for general random flows and initial condition is not possible. However, in the last two chapters, we were able to approximate numerically the full scalar PDF in the simplified models thanks to the following conditions:

a) The random flow $\vec{V}(\vec{x}, t)$ is simple enough so that we can solve the advection-diffusion equation (1.1) explicitly and the scalar can be formally written in closed (integral) forms, like in Eq. (2.9) and (3.4);

b) The randomness that the scalar inherits from the flow and from the initial distribution has simple correlation structure. Moreover, utilizing the scaling property of Wiener processes, we can transform the stochastic processes involved into random variables whose distribution or moment generating function is known.

When both of these conditions are satisfied, we can explicitly average the stochasticity to obtain the moment information or represent the PDF as a total probability. In particular, the infinite dimensional integral (1.4) reduces to the one-dimensional integral (3.15) in the case of the Majda model. However, the lack of spatial structure in the flows discussed would greatly reduce the significance of the methodologies if they cannot be applied to more general settings. To explore the prospects of extending the ideas discussed in Chapter 2 and 3, namely, the series reconstruction from the moments and numerical quadrature for a total probability, we examine several modified models by adding more spatial structure in $\vec{V}(\vec{x}, t)$ and/or in the initial scalar distribution.

4.1 Combining Shear and Translation

Let us consider the flow with both a shearing component and a translating component but in different directions

$$\vec{V}(\vec{x},t) = (\gamma(t), \gamma(t)x, 0)^T \tag{4.1}$$

where $\gamma(t)$ is again a temporal Gaussian white noise. Effectively, this is just the superposition of the flows we discussed in Chapter 2 and 3. After the change of variables

$$x' = x - B(t) \quad \text{and} \quad y' = y - \int_0^t \gamma(s)B(s)ds, \tag{4.2}$$

this problem formally reduces to the Majda Model discussed in Chapter 2. Therefore, the solution to this problem is just

$$T(x,y,t) = \bar{T}\big(x - B(t), y - \int_0^t \gamma(s)B(s)ds, t\big) \tag{4.3}$$

where $\bar{T}$ is defined in Eq.(3.4). Since this is just a random translation of Eq.(3.4) and we know that the scalar field in the Majda Model is homogeneous, the single-point statistics of the scalar in this modified problems is exactly the same as we recovered for 1D planar initial data. Observe that from the above analysis, the temporal Gaussian white noises in the shear and in the translation can be different, namely, the same statements apply to

$$\vec{V}(\vec{x},t) = (\gamma_1(t), \gamma_2(t)x, 0)^T \tag{4.4}$$

where γ_1 and γ_2 are two white noises that can be correlated, although the anomalous diffusion is only contributed to the random shear and therefore only γ_2 is statistically relevant. Another implication of this fact is that for the random translation model (3.1), if the initial data is a Gaussian random field as in (3.2), the single point scalar statistics will remain Gaussian at all times and no enhanced diffusion or intermittency would occur. However, if the initial data is deterministic and/or it has spatial dependence in the x-direction, the results would be different and calculations are much more involved.

4.2 2D Random, Linear Strain

Consider the passive scalar problem (1.1) reduced to two spatial dimensions with the incompressible, straining flow $\vec{V}(\vec{x},t) = (\gamma(t)x, -\gamma(t)y, 0)^T$. The corresponding equa-

tion in the Fourier domain with general 2D initial data reads

$$\begin{aligned} \frac{\partial \hat{T}}{\partial t} - \gamma(t)\Big(k_1\frac{\partial \hat{T}}{\partial k_1} - k_2\frac{\partial \hat{T}}{\partial k_2}\Big) &= -\frac{4\pi^2(k_1^2+k_2^2)}{\mathrm{Pe}}\,\hat{T}, \quad (k_1,k_2)\in\mathbb{R}^2,\ t>0, \\ \hat{T}|_{\,t=0} &= \hat{T}_0(k_1,k_2) \end{aligned} \tag{4.5}$$

whose solution is

$$\hat{T}(k_1,k_2,t) = \hat{T}_0(k_1e^{B(t)}, k_2e^{-B(t)})e^{-\frac{4\pi^2}{\mathrm{Pe}}[k_1^2f(t)+k_2^2g(t)]} \tag{4.6}$$

where $f(t)=\int_0^t e^{2B(s)}ds$ and $g(t)=\int_0^t e^{-2B(s)}ds$. Notice that it is not clear how these two functions compare with t, or if there is enhanced diffusion along either of the spatial dimensions. A special case is when the initial data is one-dimensional, the solution for the scalar problem remains one-dimensional. For example, if $T_0(x,y)=T_0(x)$, then

$$T(x,y,t)=T(x,t)=\int_{-\infty}^{\infty} e^{2\pi ikx-\frac{4\pi^2}{\mathrm{Pe}}k^2f(t)}\hat{T}_0(ke^{B(t)})dk \tag{4.7}$$

To average the solution to obtain moment information, we need to evaluate

$$\Big\langle e^{-\frac{4\pi^2}{\mathrm{Pe}}\vec{k}^2f(t)}\prod_{j=1}^{N}\hat{T}_0(k_je^{B(t)})\Big\rangle \tag{4.8}$$

over all realizations of the random strain and of the initial random fields where $\vec{k}=(k_1,\cdots,k_N)^T, N=1,2,\cdots$. However, the complication here compared with the solutions we have seen in previous chapters is that the 2D random flow introduces random effects not only in the diffusive term, $e^{-\frac{4\pi^2}{\mathrm{Pe}}\vec{k}^2f(t)}$, but also in the characteristics term, $\hat{T}_0(k_je^{B(t)})$. And the stochastic process $f(t)$ involved is also much more complicated than a Wiener process or its L^2-norm. For general 2D initial data, the averaging is even more difficult from (4.6).

4.3 Effects of Different Initial Data

The initial scalar distribution, $T_0(x,y)$, is also an important ingredient in the passive scalar problem. In particular, as we have seen in Chapter 3, a Gaussian random field in Fourier representation such as (3.2) greatly simplifies the calculations of the full scalar PDF since the condition distribution of the scalar remains Gaussian, or those of the its moments by reducing the dimensions of the quadrature with cluster expansion of white

noises. Moreover, the multiple spatial scales in the initial data would also introduce the "breathing" phenomena. For the elementary model in Chapter 2, we have discussed the connection between the extrema of the deterministic, initial data, and the number of the singularities in the scalar PDF.

An interesting observation can be made for the Majda Model when the initial data is a two-dimensional version of the Gaussian random field (3.2) (McLaughlin, 1994; McLaughlin and Majda, 1996), namely,

$$T_0(x,y) = \int_{\mathbb{R}^2} |\vec{k}|^{\frac{\alpha}{2}} \hat{\phi}_0(|\vec{k}|) dW(k_1) \otimes dW(k_2) \tag{4.9}$$

where $\vec{k} = (k_1, k_2)^T$ and $dW(k_1) \otimes dW(k_2)$ is complex two-dimensional Gaussian white noise satisfying

$$\begin{aligned} \langle dW(k_1) \rangle &= \langle dW(k_2) \rangle = 0, \\ \langle dW(k_1) \otimes dW(k_2), dW(k_1') \otimes dW(k_2') \rangle &= \delta(k_1 + k_1')\delta(k_2 + k_2') dk_1 dk_2 dk_1' dk_2'. \end{aligned} \tag{4.10}$$

The calculations for the arbitrary moments of the passive scalar for this initial data are similar to those for 1D random fields (McLaughlin and Majda, 1996; Bronski and McLaughlin, 2000a). However, if we seek to formulate the full scalar PDF as a total probability, we would encounter difficulty. First, the random solution reads

$$T(x,y,t) = \int_{\mathbb{R}^2} e^{2\pi i(k_1 x + k_2 y)} [F(\vec{k},t)]^{\frac{\alpha}{4}} \hat{\phi}_0(\sqrt{F(\vec{k},t)})\, e^{-\frac{4\pi^2}{\mathrm{Pe}} \int_0^t F(\vec{k},s) ds} dW(k_1) \otimes dW(k_2) \tag{4.11}$$

where $F(\vec{k},t) = [k_1 + B(t)k_2]^2 + k_2^2$. Although this is still a homogeneous, 2D Gaussian random field given a fixed history of $\gamma(t), t > 0$ and one can still compute $\langle T^N \rangle_{W,\gamma}$ for $N = 1, 2, \cdots$, it is not straightforward that the conditional scalar variance, $\langle T^2 \rangle_W$, is dependent on one single random variable, whereas for one-dimensional data in (3.12), the conditional variance is dependent only on the renormalized L^2-norm of the Brownian motion, $\eta = \int_0^1 B^2(s) ds$. Therefore, the integral representation of the full scalar PDF in this setting has to be further explored. Alternatively, we can use the moment information the reconstruct the PDF with orthogonal polynomials, as we did in Chapter 2. However, since the scalar value is not compactly supported anymore and it can take any value in $(-\infty, \infty)$, we need to use orthogonal polynomials defined for the positive real axis (the PDF is even because all odd moments vanish).

Chapter 5

Shallow Water Simulation

Ultimately, we would like to model and predict the scalar intermittency observed in realistic, large-scale fluid systems. In Chapter 2, we discussed the scalar PDF evolving from a Delta measure set by deterministic initial data in a simple, random translation of pure diffusion. The fluid flow was more complicated in Chapter 3 and the scalar is intially Gaussian-randomly distributed. In both of these scenarios, we obtained rather complete results for the probability measures of the scalar. Alternatively, in this chapter, we explore the random scalar evolution in a deterministic yet complex fluid model, since the flows in real, geophysical systems have much more complicated spatial and temporal dependence than the simple flows we have discussed. Here, we eliminate the stochastic components in the geophysical flows which are complex enough. Previous work on scalar intermittency in a deterministic fluid flow is reviewed and extended numerically in (Camassa et al., 2005). In particular, we will present some preliminary results of simulating a passive scalar in a shallow water model in which we observe the development of intermittency (Camassa et al., 2007). The flow simulation itself is non-trivial and we develop a numerical code based on the finite volume package CLAWPACK (Leveque, 2002).

5.1 Problem Formulation

The model is an idealized, two-dimensional, mid-latitude ocean model domain configuration whose size in both the zonal (x) and meridional (y) direction is denoted by L. We adopt the "one-and-a-half-layer" model with β-plane approximation for the earth rotation (Pedlosky, 1998) to model the upper ocean dynamics. We also take into account the viscous effects and mid-latitude wind forces. The dependent variables are

- Layer-averaged 2D velociy:

$$\begin{pmatrix}\bar{u}(x,y,t)\\ \bar{v}(x,y,t)\end{pmatrix} = \frac{1}{h}\int_0^h \begin{pmatrix}u(x,y,z,t)\\ v(x,y,z,t)\end{pmatrix} dz$$

- Fluctuation of the ocean thickness offset by a typical value H_0: $h(x,y,t)$

- Layer-averaged scalar concentration: $\bar{T}(x,y,t) = \frac{1}{h}\int_0^h T(x,y,z,t)dz$

The dimensional, governing equations for $(x,y) \in \Omega = [0,L]^2, t > 0$ are

$$\begin{aligned}
\bar{u}_t + \bar{u}\bar{u}_x + \bar{v}\bar{u}_y - (f_0 + \beta y)\bar{v} &= -g'h_x + \nu\Delta\bar{u} + F^x,\\
\bar{v}_t + \bar{u}\bar{v}_x + \bar{v}\bar{v}_y + (f_0 + \beta y)\bar{u} &= -g'h_y + \nu\Delta\bar{v} + F^y,\\
h_t + (h\bar{u})_x + (h\bar{v})_y &= 0,\\
\bar{T}_t + \bar{u}\bar{T}_x + \bar{v}\bar{T}_y &= \kappa\Delta\bar{T}
\end{aligned} \tag{5.1}$$

in which g' is the reduced gravity, ν is the kinematic viscocity, κ is the molecular diffusivity of the scalar, f_0 and β are Coriolis constants and F^x, F^y represent the zonal and meridional wind forces, respectively. In this thesis, we set $F^y \equiv 0$ and

$$F^x = -\frac{\tau_0}{\rho_0 H_0}\cos\Big(\frac{2\pi y}{L}\Big) \tag{5.2}$$

where ρ_0 is the reference density of the sea water and τ_0 is a parameter characterizing the magnitude of the zonal periodic wind stress. The uni-directional wind shear is strongest in the middle of the domain, $y = 0$. This is a reasonable approximation to the zonal wind observed at the mid-latitudes (Jones et al., 1997).

Eq.(5.1) are supplemented with the boundary and initial conditions given by

$$\begin{gathered}
\bar{u}|_{\partial\Omega} = \bar{v}|_{\partial\Omega} = \tfrac{\partial h}{\partial\vec{n}}|_{\partial\Omega} = \tfrac{\partial\bar{T}}{\partial\vec{n}}|_{\partial\Omega} = 0,\\
\bar{u}(x,y,0) = \bar{u}_0(x,y),\ \bar{v}(x,y,0) = \bar{v}_0(x,y),\ h(x,y,0) = h_0(x,y),\\
\bar{T}(x,y,0) = \bar{T}_0(x,y) = \textstyle\int_\Omega E^{\frac{1}{2}}(|\vec{k}|)dW(k_1)\otimes dW(k_2)
\end{gathered} \tag{5.3}$$

in which $\vec{n}$ is the outward-pointing normal to the boundary of the domain, $\partial\Omega$ and E is the energy spectrum of the initial random scalar field.

5.2 Numerical Implementation

Before running the code, we need to first specify the physical parameters which tabulated in Table 5.1. As for the numerical discretization, we use uniform, constant $\Delta x = \Delta y = 4$ km and $\Delta t = 720$ s, whose stability are verified in the simulations for this set of physical parameters.

Parameter	Value
H_0	500 m
L	2000 km
f_0	6×10^{-5} s^{-1}
β	2×10^{-11} m^{-1} s^{-1}
g'	0.02 m s^{-1}
ν	600 m^2 s^{-1}
κ	100 m^2 s^{-1}
ρ_0	1000 kg m^{-3}
τ_0	0.05 N m^{-2}

Table 5.1: Physical Parameters in Shallow Water Simulation

The numerical scheme for this problem adopts an *operator-splitting method* which divides the updating procedure from $t = t_i$ to $t = t_{i+1}$, into two stages:

1. First, we use a finite volume solver to update the hyperbolic part of the equations, namely, to solve for the equations

$$\begin{aligned} \bar{u}_t + \bar{u}\bar{u}_x + \bar{v}\bar{u}_y &= -g'h_x, \\ \bar{v}_t + \bar{u}\bar{v}_x + \bar{v}\bar{v}_y &= -g'h_y, \\ h_t + (h\bar{u})_x + (h\bar{v})_y &= 0, \\ \bar{T}_t + \bar{u}\bar{T}_x + \bar{v}\bar{T}_y &= 0 \end{aligned} \tag{5.4}$$

   from t_i to t_{i+1}. To accomplish this using the finite volume scheme, it is necessary to rewrite the above equations in a conservative form and to linearize and decompose the system in to simple waves (Leveque, 2002).

2. Next, we take the output of Stage 1 as the initial condition and use a fourth-order Runge-Kutta scheme to solve the PDE system

$$
\begin{aligned}
\bar{u}_t &= \nu\Delta\bar{u} + (f_0 + \beta y)\bar{v} + F^x, \\
\bar{v}_t &= \nu\Delta\bar{v} - (f_0 + \beta y)\bar{u} + F^y, \\
\bar{T}_t &= \kappa\Delta\bar{T}
\end{aligned}
\tag{5.5}
$$

from t_i to t_{i+1}. Then we use the output as the numerical solution of the original system (5.1) at $t = t_{i+1}$.

During this procedure, all spatial derivatives are descritized using second-order central-differencing scheme. The temporal derivatives are descritized with an explicit upwinding scheme. Alternatively, in Stage 2, we can use a Crank-Nicolson type scheme to implicitly discretize the heat operator and solve for Eq.(5.5), such as the numerical package FISHPAK (see `http://www.cisl.ucar.edu/softlib/FISHPAK.html`).

5.3 Preliminary Results and Discussions

The initial conditions for the velocity and height fields, $\bar{u}(x, y, 0), \bar{v}(x, y, 0)$ and $h(x, y, 0)$, are obtained from a "spin-up" run of the code, without the scalar evolution, for an ocean starting at rest with constant thickness H_0. The purpose of this run is to integrate the flow equations until a statically stationary flow is established and the duration of this spin-up is 10 physical years.

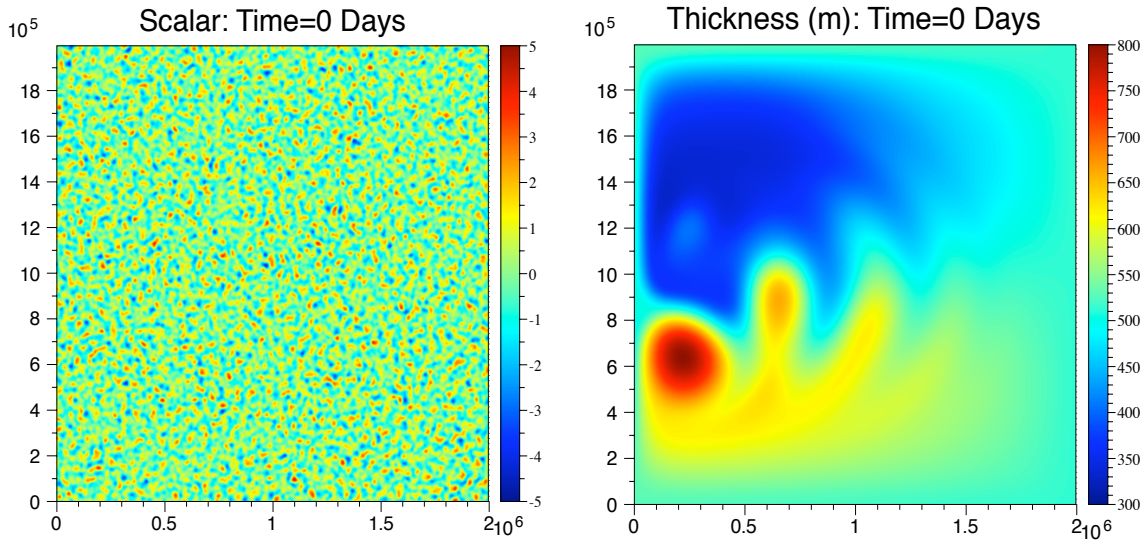

Figure 5.1: Initial Scalar and Thickness Distribution for the Shallow Water Simulation

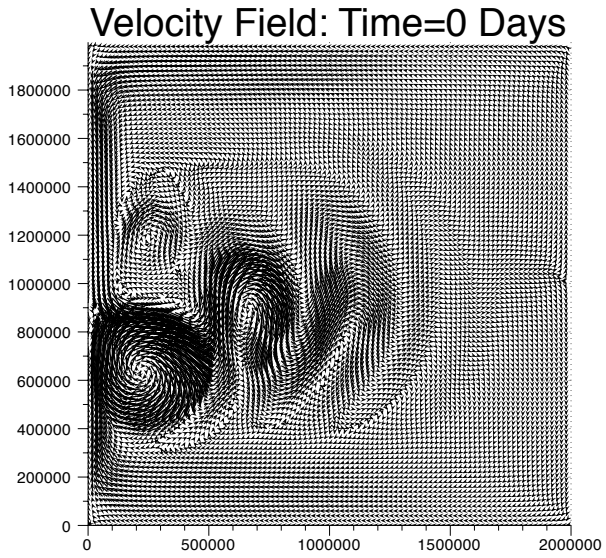

Figure 5.2: Initial Velocity Distribution for the Shallow Water Simulation

Figure 5.1 and 5.2 illustrate the outputs of the spin-up, along with the renormalized, initial two-dimensonal Gaussian random scalar field. The magnitude of the velocity field is around 1 ms^{-1}. We can clearly observe three distinguishing features of the shallow water model from the thickness and velocity distribution: the double-gyre structure, the western intensification and the meandering jet around $y = 0$ introduced by the wind stress. The initial scalar field is generated by a numerical approximation to the random integral in (5.3), which is essentially the two-dimensional version of Eq.(3.17), where the energy spectrum function E is

$$E(\vec{k}) = \frac{C|\vec{k}|^7}{(|\vec{k}| + 50)^{18}} \, . \tag{5.6}$$

where C is a renormalization constant to enforce the requirement that the variance of the initial field is unity. Motivated by the common experimental settings in which scalar values were measured over time as the measuring platforms (e.g. towboats or airplanes) move through the surrounding fluid, we conduct analogous statistics here by considering all the values at different spatial locations as samples from a distribution of possible scalar values. And histograms are made to approximate this distribution, in which the scalar is renormalized by its spatial variance. It should be noted that the results presented here are different from the more familiar ensemble- or time-averaging constructions of probability density functions. However, the spatial statistics conducted

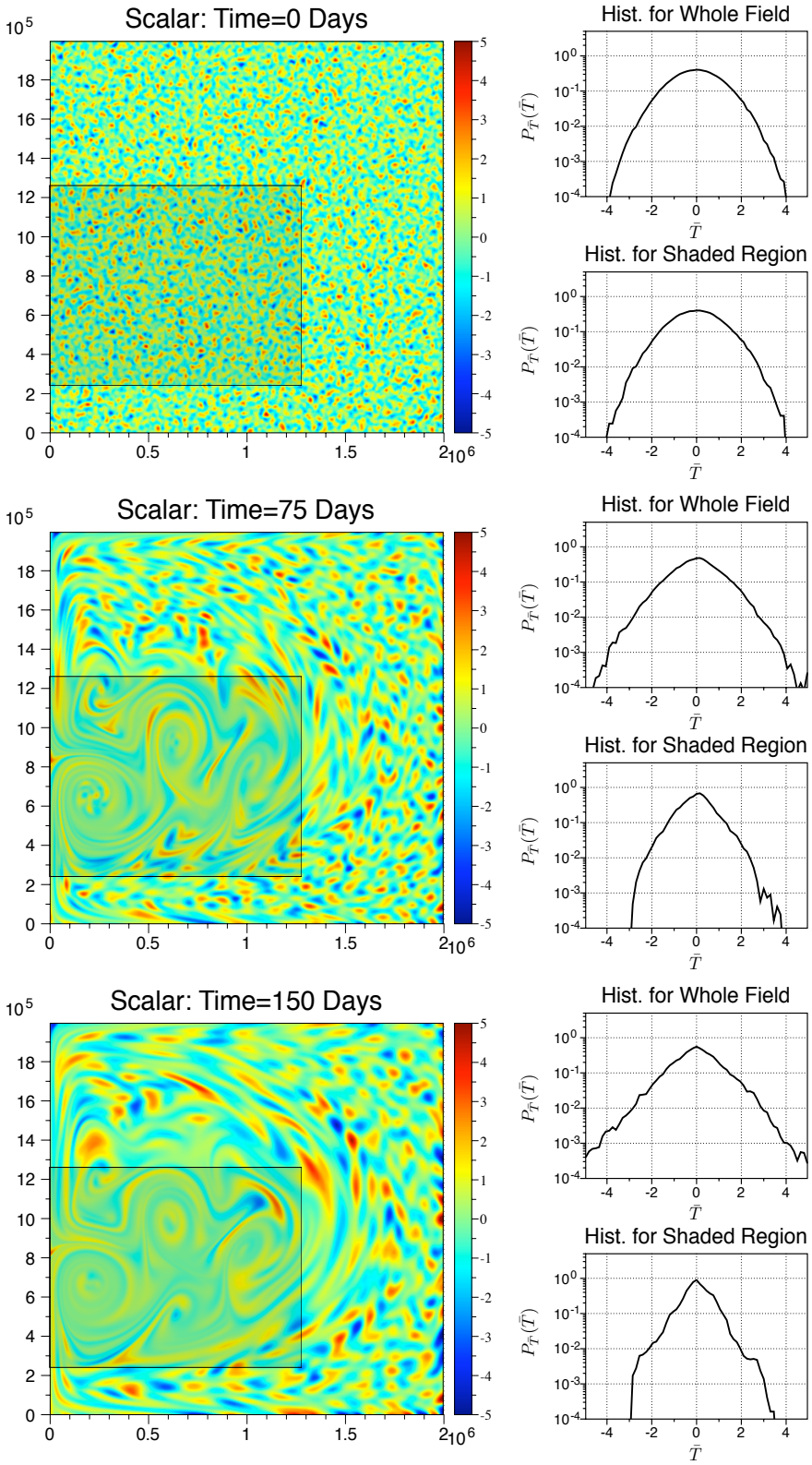

Figure 5.3: Scalar Intermittency in Shallow Water Equations.

is not *a priori* invalid, in light of its physical relevance and the previous discussion of spatially ergodicity in Chapter 3.

With the above initial conditions, we evolve the full system (5.1) in which the fluid flow is *deterministic*, although the passive scalar being advected is still stochastic due to its initial distribution. The code has been tested on a problem for which an exact solution is available, and the shallow water results has been verified by a benchmark run of an enslaved finite-differencing scheme with semi-Lagrangian method (Camassa et al., 2007; Poje et al., 1996). Notice that over the evolution, the velocity and water thickness profiles does not change much from the initial distributions, thanks to the spin-up stage and therefore they are not plotted here.

Over a run of 150 days, we observe the development of scalar intermittency from the deviation from Gaussian in the spatial histogram. This is demonstrated in Figure 5.3. In fact, the formation of the heavy tails starts immediately after $t = 0$, when the scalar is initially distributed throughout the fluid. We also pay special attention to the coherent structure in this model — the dominant vortices (the shaded area), and look at the scalar distribution restricted around that region. Therefore two spatial histograms are plotted separately, by collecting the scalar values in the whole domain, and only the values near the five vortices. By comparing these two histograms, an interesting observation can be made that large fluctuations are excluded from the vortices, where the scalar is well mixed. Consequently, although the tails in the histogram of the whole domain are growing to near exponential at 150 days, the trend is reversed near the vortices. For small fluctuations, the scalar distributes similarly in vortices as in the whole domain. Compared to what is observed in some cellular flows (Camassa et al., 2005) where the weak relative shear within the vortices preserves the large scalar fluctuations, the enhanced mixing we see here is potentially attributed to the relatively large correlation length in the initial scalar distribution, which is ultimately controlled by the initial energy spectrum function, $E(\vec{k})$. Alternatively, this might suggest the different natures between the vortices in this shallow water model and those in the cellular flows studied before, which will be explored in future work.

Since this is a complete, nonlinear PDE system that is known to predict many observed geophysical phenomena, such as Rossby and Kelvin waves (Pedlosky, 1998), the physical significance of studying the passive scalar behavior in such a system is obvious. However, the fluid flow is much more complicated than the simple flows that we discussed in previous chapters, even if it is still deterministic here. Moreover, different physical factors contribute to change the behavior of fluid flow and consequently the

scalar, such as gravity, rotation, viscosity, diffusivity and wind force. The complicated interaction between these effects increases the difficulty for analyses drastically yet it is critical for us to understand the key transport and mixing mechanisms in turbulent, geophysical flows. For example, if we only increase the molecular diffusivity of the scalar from $\kappa = 100$ to $\kappa = 400$, the scalar behavior becomes more diffusive and also more intermittent at $t = 150$ days and there is a noticeable difference between the whole domain and the region near the vortices. This is illustrated in Figure 5.4. Apparently, compared to Figure 5.3, the scalar distribution for small fluctuations (the core) is much closer to Gaussian, whereas the tails are heavier and appear stretched-exponentially. Furthermore, in our preliminary simulations, we see intensification of the intermittency, namely, heavier tails in the spatial histograms, by increasing the magnitude of the wind forces, τ_0 while keeping the values of other parameters unchanged. In addition to different flow parameters, alternative scales and correlation structures in the initial scalar distribution, in particular, the energy spectrum E, are also expected to change the pictures, as we have seen in Chapter 3.

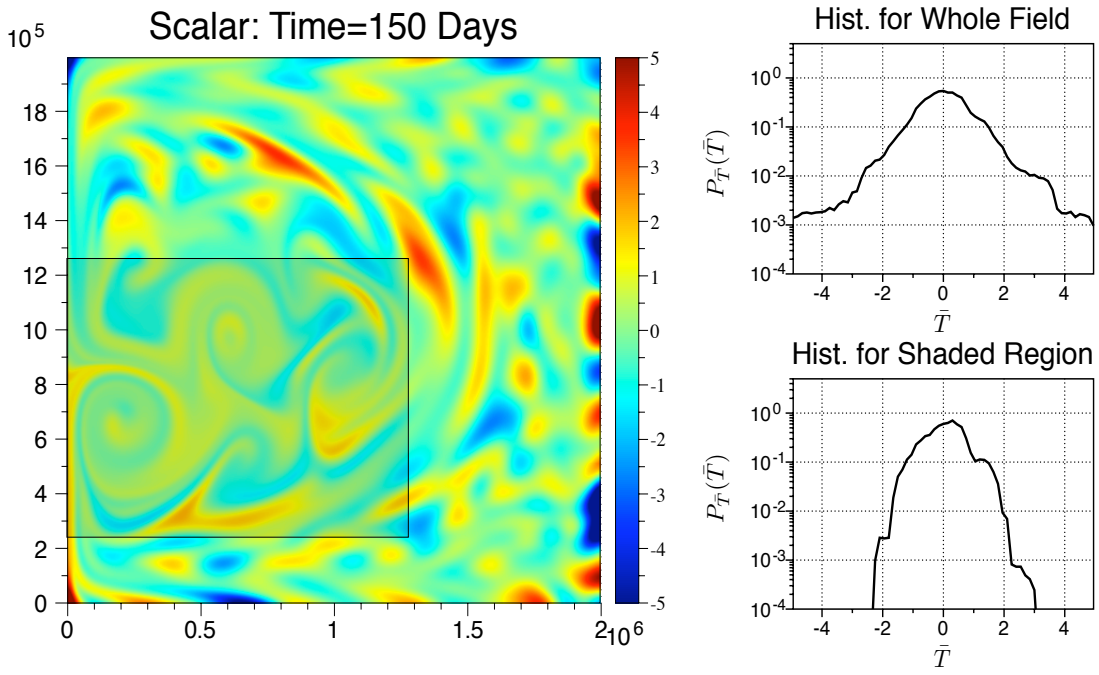

Figure 5.4: More Intermittent Scalar from Larger Diffusivity, $\kappa = 400$.

A possible way to analyze this model is to consider its non-dimensional formulation and the ensuing distinguishing limits for different parameters, such as the Froude number, Rossby number, Reynolds number, Prandtl number and Péclet number. For

example, for the purpose of simplification and to study the characteristic phenomena within the *Rossby deformation radius*, the quasi-geostrophic equations as the singular limit of shallow water equations (5.1) (Majda, 2003) should be studied. Furthermore, future directions will involve adding random components to the velocity and wind forces to make the flow itself random. For example, we can introduce white noise processes similar to what was discussed in previous chapters into the wind force terms, and/or the convective terms in the scalar equation. Moreover, for a more realistic model to mimic the processes in the ocean, external sources and sinks should be included in the scalar equation.

There is also many improvements that can be made to the numerical scheme. In particular, since the random scalar usually varies on spatial and temporal scales which are much smaller than those for velocity and water thickness fields, a multi-scale computation would greatly improve the accuracy and efficiency of the numerical simulation. In particular, the momentum and thickness equations in Eq.(5.1) can be solved on a coarser grid with larger time stepping, whereas a separate scalar solver can be used to evolve the scalar equation on a much denser grid with smaller time step.

Summary

The study of passive scalars is an important subject in the theory of turbulence since it is closely related to the dynamical features of the underlying turbulent flows. A particular phenomena of interest arose from recent experimental and computational observations of intermittency for diffusing passive scalars, as characterized by higher than Gaussian probability for large fluctuations, or "heavy tails".

Starting with the pioneering work by Kraichnan in 1968, the universality of passive scalar intermittency in turbulence has came to attention of physicists and mathematicians. However, it is generally an extremely difficult problem to model and understand this phenomena and most of the previous attempts were forced to adopt some *ad hoc*, phenomenological assumptions to derive closed equation without a systematic, first principle theory.

This thesis focuses on the spatio-temporal evolution of the probability measure of a passive tracer diffusing in a random fluid flow and overview the ongoing research involving nonlinear, multi-scale simulations for geophysical systems. In particular, we extended the previous study for a random, shear layer model that predicted heavy-tailed, non-Gaussian tracer distributions, with more detailed, comprehensive asymptotic analysis, and careful, benchmarked numerical simulations. Further, we would like to generalize the idea and methodology to study the effects of more realistic, large-scale geophysical flows like mid-latitude shallow water models, which scalar intermittency is observed from numerical simulations here, and general circulation models, and ultimately to improve the prediction of the state and the dynamics of the systems.

Detailed theoretical and numerical analysis are performed for two simple in space, Gaussian white in time random flows subject to deterministic or Gaussian random initial field. Although the geometry of the flows discussed are overly simplified so that the scalar PDF can be explicitly obtained or has been studied by previous researchers for its long time, tail behavior, the methodology presented here sheds new light on how one can numerically approximate the full scalar PDF for more complicated flows. Also,

the asymptotic analyses provides more complete illustration of the dynamical features and parametric sensitivity of the scalar measure. Moreover, a transient, "breathing" phenomena is discovered and identified as a product of initial data with multiple scales.

Appendix

A.1 Proof for Eq.(2.21)

First we claim that

$$\det A_N = \pi^{2N}(Nab^{N-1} + b^N). \tag{A.7}$$

To see this, we can use the induction method. After some algebra we arrive at

$$\begin{aligned}
\frac{\det A_N}{\pi^2} &= (a+b)\frac{\det A_{N-1}}{\pi^2} - a\begin{vmatrix} a & a & \cdots & a \\ a & a+b & \cdots & a \\ \cdots & \cdots & \cdots & \cdots \\ a & a & \cdots & a+b \end{vmatrix} + a\begin{vmatrix} a & a+b & \cdots & a \\ a & a & \cdots & a \\ \cdots & \cdots & \cdots & \cdots \\ a & a & \cdots & a+b \end{vmatrix} - \ldots \\
&= (a+b)\frac{\det A_{N-1}}{\pi^2} - (N-1)a\begin{vmatrix} a & a & a & \cdots & a \\ a & a+b & a & \cdots & a \\ \cdots & \cdots & \cdots & \cdots & \cdots \\ a & a & a & \cdots & a+b \end{vmatrix} \qquad \text{(A.8)} \\
&= (a+b)\frac{\det A_{N-1}}{\pi^2} - (N-1)a^2 b^{N-2}.
\end{aligned}$$

Here we use the fact that

$$\begin{vmatrix} a & a & a & \cdots & a \\ a & a+b & a & \cdots & a \\ a & a & a+b & \cdots & a \\ \cdots & \cdots & \cdots & \cdots & \cdots \\ a & a & a & \cdots & a+b \end{vmatrix} = \begin{vmatrix} a & 0 & 0 & \cdots & 0 \\ a & b & 0 & \cdots & 0 \\ a & 0 & b & \cdots & 0 \\ \cdots & \cdots & \cdots & \cdots & \cdots \\ a & 0 & 0 & \cdots & b \end{vmatrix} = ab^{N-2}. \tag{A.9}$$

With the same procedure, the formula for the characteristic polynomial of A_N reads

$$P_N(\lambda) = \pi^{2N}(\lambda - b)^{N-1}(\lambda - Na - b). \tag{A.10}$$

The eigenvector associated with the non-degenerate eigenvalue $\pi^2(Na+b)$ of A_N defined in (2.16) is explicitly $\vec{v}_N = \{\frac{1}{\sqrt{N}}, \frac{1}{\sqrt{N}}, \cdots, \frac{1}{\sqrt{N}}\}^t$, on account of the elementary matrix vector product for this eigenvector $A_N\vec{v}_N = \pi^2(Na+b)\vec{v}_N$. Therefore in Eq.(2.21)

$$V_m = \sum_{n=1}^{N} v_{mn} = \sqrt{N}\vec{v}_m^{\,t} \cdot \vec{v}_N = \begin{cases} 0, & m \neq N \\ \sqrt{N}, & m = N \end{cases} \tag{A.11}$$

since when $m \neq N$, $\vec{v}_m$ are eigenvectors associated with the multiple eigenvalue $\pi^2 b$.

A.2 Proof for Eq.(2.43)

Let series (2.38) be re-written as

$$P_{0,t}(\xi) = P_r(\xi)P_s(\xi), \tag{A.12}$$

where $P_s(\xi)$ is the singular part $\frac{1}{\sqrt{1-\xi^2}}$ (restricted to the interval [-1,1]), and $P_r(\xi)$ is the regular part $\sum_{m=0}^{\infty} c_m\, T_m(\xi)$, which we extend evenly to [-1,1] by symmetry around the origin. Then the *characteristic function* of $P_{0,t}(\xi)$:

$$\hat{P}(k) = \int_{-\infty}^{\infty} e^{ik\xi} P_r(\xi)P_s(\xi)d\xi, \tag{A.13}$$

and thus by the Convolution Theorem

$$\begin{aligned} \hat{P}(k) &= \frac{1}{2\pi}\int_{-\infty}^{\infty} \hat{P}_r(q)\hat{P}_s(k-q)\, dq \\ &= \frac{1}{2}\int_{-\infty}^{\infty} \hat{P}_r(q)J_0(k-q)\, dq \end{aligned} \tag{A.14}$$

since

$$\hat{P}_s(k) = \pi J_0(k) \tag{A.15}$$

where

$$J_0(k) = \sum_{m=0}^{\infty} \frac{(-1)^m k^{2m}}{(2m)!} \frac{(2m)!}{4^m (m!)^2}$$

is the Bessel function of the first kind of order zero. Then

$$\widetilde{M}_n = \frac{2}{\sqrt{1+\frac{a}{b'}n}} = (-i)^n \frac{d^n \hat{P}(k)}{dk^n}\Big|_{k=0} = \frac{1}{2}\int_{-\infty}^{\infty} \hat{P}_r(q) J_0^{(n)}(-q) dq \tag{A.16}$$

Further, we have the following identity (follows from the generating function of the Bessel functions)

$$J_0(x+y) = \sum_{m=-\infty}^{\infty} J_m(x) J_{-m}(y), \tag{A.17}$$

from which we derive

$$\hat{P}(k) = \frac{1}{2}\sum_{m=-\infty}^{\infty} J_m(k) \int_{-\infty}^{\infty} \hat{P}_r(q) J_{-m}(-q) dq. \tag{A.18}$$

since $\hat{P}_r(q)$ is real and even by construction and $J_{-m}(-x) = J_m(x)$. Thus

$$\hat{P}(k) = \frac{1}{2}\sum_{m=0}^{\infty} w_m J_m(k) \int_{-\infty}^{\infty} \hat{P}_r(q) J_m(q) dq, \tag{A.19}$$

where $w_m = 1$ if $m = 0$ and $w_m = 2$ otherwise. Another useful identity links Bessel functions to Chebyshev polynomials $T_m(x)$, that is

$$J_m(x) = i^m T_m\left(i\frac{d}{dx}\right) J_0(x), \tag{A.20}$$

Therefore

$$\begin{aligned} \int_{-\infty}^{\infty} \hat{P}_r(q) J_m(q) dq &= \frac{i^m}{\pi}\int_{-1}^{1} \frac{T_m(x) P_r(x)}{\sqrt{1-x^2}} dx = i^m C_m \\ \hat{P}(k) &= \frac{1}{2}\sum_{m=0}^{\infty} w_{2m} J_{2m}(k) (-1)^m C_{2m} \end{aligned} \tag{A.21}$$

where we utilize the fact that $C_{2m+1} = 0$, $m = 0, 1, 2, \cdots$. Now

$$\widetilde{M}_{2n} = \frac{2(-1)^n}{\sqrt{1+2\frac{a}{b'}n}} = \frac{1}{2}\sum_{m=0}^{\infty} w_{2m} J_{2m}^{(2n)}(0) (-1)^m C_{2m}, \tag{A.22}$$

which follows from the Taylor expansion of the Fourier transform. The last piece is to note that

$$J_{2m}^{(2n)}(0) = \frac{(-1)^{n-m}(2n)!}{2^{2n}(n-m)!(n+m)!} \tag{A.23}$$

for $m < n$ and zero otherwise, that is

$$\frac{2}{\sqrt{1+2\frac{a}{b'}n}} \;=\; \frac{1}{2}\frac{(2n)!}{4^n(n!)^2}\sum_{m=0}^{n}\frac{(n!)^2}{(n-m)!(n+m)!}\,c_{2m}\,w_{2m} \tag{A.24}$$

and this is essentially Eq.(2.43).

A.3 Asymptotic Analysis for Expansion Coefficients C_{2n} in Eq.(2.51)

Integrating $I(z)$ defined in (2.52) on $\mathcal{C}_1$ defined in Sec. 4.5 for large n, we have

$$\begin{aligned}
&\lim_{T\to\infty}\int_{\mathcal{C}_1} e^{i2nz}\sin z\,\frac{e^{-\frac{x^2}{a}}\,(\cos z)^{\frac{1}{\beta}-1}\,\cosh\sqrt{-\frac{4x^2b'}{a^2}\ln(\cos z)}}{\sqrt{-\beta\pi\ln(\cos z)}}\,dz \\
=\;& -ie^{-\frac{x^2}{a}}\int_0^\infty \frac{e^{-2ny}\,\sinh y\,(\cosh y)^{\frac{1}{\beta}-1}\,\cos\sqrt{\frac{4x^2b'}{a^2}\ln(\cosh y)}}{\sqrt{\beta\pi\ln(\cosh y)}}\,dy
\end{aligned} \tag{A.25}$$

which is purely imaginary since $\ln(\cosh y)$ is non-negative. Clearly, the contribution from $\mathcal{C}_2$ is bound to vanish as $T\to\infty$.

Finally, for large n on $\mathcal{C}_3$,

$$\begin{aligned}
&\lim_{T\to\infty}\int_{\mathcal{C}_3} e^{i2nz}\sin z\,\frac{e^{-\frac{x^2}{a}}\,(\cos z)^{\frac{1}{\beta}-1}\,\cosh\sqrt{-\frac{4x^2b'}{a^2}\ln(\cos z)}}{\sqrt{-\beta\pi\ln(\cos z)}}\,dz \\
=\;& \frac{e^{-\frac{x^2}{a}-i(\frac{\pi}{2\beta}-n\pi)}}{\sqrt{\beta\pi}}\int_0^\infty \frac{e^{-2ny}\cosh y\,(\sinh y)^{\frac{1}{\beta}-1}\cosh\sqrt{-\frac{4x^2b'}{a^2}\ln(-i\sinh y)}}{\sqrt{-\ln(-i\sinh y)}}\,dy \\
\sim\;& \frac{(-1)^n e^{-\frac{x^2}{a}-i\frac{\pi}{2\beta}}}{\sqrt{\beta\pi}}\int_0^\varepsilon \frac{e^{-2ny}\cosh y\,(\sinh y)^{\frac{1}{\beta}-1}\cosh\sqrt{-\frac{4x^2b'}{a^2}\ln(-i\sinh y)}}{\sqrt{-\ln(-i\sinh y)}}\,dy
\end{aligned} \tag{A.26}$$

for $1 \gg \varepsilon > 0$ fixed since

$$\Big| \int_\varepsilon^\infty \frac{e^{-2ny}\ \cosh y\ (\sinh y)^{\frac{1}{\beta}-1}\ \cosh\sqrt{-\frac{4x^2b'}{a^2}\ln(-i\sinh y)}}{\sqrt{-\ln(-i\sinh y)}}\ dy\Big| < K_\varepsilon e^{-2n\varepsilon} \tag{A.27}$$

where K_ε is a constant determined by ε and and we will see that this is negligible compared to the contribution from the interval $[0,\varepsilon]$ for large n. Moreover, the last integral in (A.26) can be asymptotically approximated by

$$(-1)^n\sqrt{\frac{1}{\beta\pi}}\ e^{-\frac{x^2}{a}-i\frac{\pi}{2\beta}}\int_0^\varepsilon \frac{e^{-2ny}\cosh\sqrt{-\frac{4x^2b'}{a^2}\ln(-iy)}}{y^{-\frac{1}{\beta}}\sqrt{-\ln(-iy)}}\ dy \tag{A.28}$$

since for $0 \le y \le \varepsilon$, $\cosh y \sim 1$ and $\sinh y \sim y$. Further, the contribution from the interval $[0, n^{-3/2}]$ in (A.28) is bounded by

$$\begin{aligned}\Big| \int_0^{n^{-3/2}} \frac{e^{-2ny}\cosh\sqrt{-\frac{4x^2b'}{a^2}(\ln(-iy)}}{y^{1-\frac{1}{\beta}}\sqrt{-\ln(-iy)}}\ dy\Big| \ &< \ K\int_0^{n^{-3/2}} \frac{\exp\sqrt{-\frac{4x^2b'}{a^2}\ln y}}{y^{1-\frac{1}{\beta}}\sqrt{-\ln y}}\ dy \\ &= \ \widetilde{K}\Big[1-\mathrm{Erf}\Big(\sqrt{\frac{3\ln n}{2\beta}}-\sqrt{\frac{\beta x^2b'}{a^2}}\Big)\Big] \\ &= \ O\Big(n^{-\frac{3}{2\beta}}(\ln n)^{-\frac{1}{2}}\exp\sqrt{\frac{6x^2b'}{a^2}\ln n}\ \Big)\end{aligned} \tag{A.29}$$

as $n \to \infty$, from the large x asymptotics of $\mathrm{Erf}(x)$ and here K, $\widetilde{K}$ are constants.

Next we claim that the dominating contribution of the integral in (A.28) comes from the integral $[n^{-3/2}, \varepsilon]$. To see this, it suffices to make a change of variable $r = ny$ and study

$$\begin{aligned}\mathcal{I}(n) \ &= \ \int_{n^{-3/2}}^{\varepsilon} \frac{\exp\Big(-2ny \pm \sqrt{-\frac{4x^2b'}{a^2}\ln(-iy)}\ \Big)\ y^{\frac{1}{\beta}-1}}{\sqrt{-\ln(-iy)}}\ dy \\ &= \ \frac{1}{n^{\frac{1}{\beta}}\sqrt{\ln n}}\int_{n^{-1/2}}^{\varepsilon n} \frac{\exp\Big[-2r \pm \sqrt{\frac{4x^2b'}{a^2}\ln n\Big(1-\frac{\ln r - i\pi/2}{\ln n}\Big)}\Big]}{\sqrt{1-\frac{\ln r-i\pi/2}{\ln n}}}\ r^{\frac{1}{\beta}-1}\ dr\end{aligned} \tag{A.30}$$

since for $x \neq 0$, $\Big|\frac{\ln r - i\pi/2}{\ln n}\Big| < 1$ over this interval and thus the inverse square root and the exponent in the numerator can be expanded. Then a term-by-term integration

and extending the integration interval to $[0,\infty]$ produce a valid asymptotic series by the Dominated Convergence Theorem applied for any fixed n and by the fact that $\lim_{n\to\infty}\int_{n^{-1/2}}^{\epsilon n} e^{-2r} r^{\frac{1}{\beta}-1}(\ln r - i\pi/2)^j dr$ exists and is finite for any $j \geq 0$ and $\beta > 0$ (a very similar example can be found in Section 6.6 of (Bender and Orszag, 1999)). At leading order, this yields

$$\mathcal{I}(n) \sim \frac{\exp\Big(\pm\sqrt{\frac{4x^2b'}{a^2}\ln n}\Big)}{n^{\frac{1}{\beta}}\sqrt{\ln n}} \int_0^\infty e^{-2r} r^{\frac{1}{\beta}-1}\Big[1 \mp \frac{\ln r - i\pi/2}{2\sqrt{\ln n}}\Big]\, dr, \quad n\to\infty \tag{A.31}$$

so finally we obtain the asymptotic approximation

$$|C_{2n}| \sim \left| Re\Big[\frac{\Gamma(\frac{1}{\beta})e^{-\frac{x^2}{a}-i\frac{\pi}{2\beta}}}{(2n)^{\frac{1}{\beta}}\sqrt{\beta\pi\ln n}} \cosh\sqrt{\frac{4x^2b'}{a^2}\ln n}\,\Big(1 + i\frac{\pi\tanh\sqrt{\frac{4x^2b'\ln n}{a^2}}}{4\sqrt{\ln n}}\Big)\Big]\right| \tag{A.32}$$

which dominates over (A.27) and (A.29). As a special case, when $x = 0$ and $\beta = \frac{1}{2k+1}, k = 0, 1, \cdots$, the leading order asymptotics of C_{2n} becomes proportional to $n^{-\frac{1}{\beta}}(\ln n)^{-\frac{3}{2}}$ because the term $\exp\big(-i\frac{\pi}{2\beta}\big)$ is pure imaginary and the tanh term in (A.32) vanishes. For $x = 0$ and $\beta = 1$, Figure 2.1 shows that when $n > 500$, C_{2n} is almost identical to its asymptotic approximation.

For the shifted Chebyshev polynomials and $r(\xi) = \sqrt{\xi^3(1-\xi)}$, a similar formula is obtained following exactly the same procedure except that $\frac{1}{\beta}$ is replaced by $\frac{1}{\beta}+1$.

A.4 Evaluation of the PDF for L^2-Norm of Brownian Motion, $P_\eta(\eta)$

Recall that $\eta := \int_0^1 B^2(s)ds$. Although the explicit formula for $P_\eta(\eta)$, the probability density function for the L^2 norm of the Wiener process $B(t)$, is beyond authors' knowledge, its Laplace transform can be obtained by discretizing $B(t)$ by $B(t) \approx \sum_{i=1}^n \xi_i$ where $\xi_i,\ i = 1, 2, \cdots, n$ are i.i.d., mean-zero Gaussian random variables with variance $\frac{1}{n}$. Then by letting $n \to \infty$, it is known by solving an eigenvalue problem (Bronski, 2003) that

$$\eta = \int_0^1 B^2(\tau)d\tau \approx \frac{1}{n}\sum_{i=1}^n \Big(\sum_{j=1}^i \xi_i\Big)^2 = \frac{1}{n}\,\vec{\xi}^{\,T} A\,\vec{\xi} \tag{A.33}$$

and the matrix A is the matrix product

$$A = \begin{pmatrix} 1 & 1 & \cdots & 1 \\ 0 & 1 & \cdots & 1 \\ \cdots & \cdots & \cdots & \cdots \\ 0 & 0 & \cdots & 1 \end{pmatrix} \cdot \begin{pmatrix} 1 & 0 & \cdots & 0 \\ 1 & 1 & \cdots & 0 \\ \cdots & \cdots & \cdots & \cdots \\ 1 & 1 & \cdots & 1 \end{pmatrix} = \Big(\min(n-i, n-j) \Big)_{i,j=1}^{n} \tag{A.34}$$

Then the Laplace Transform of $P_\eta(\eta)$ can be approximated by

$$\begin{aligned} \int_0^\infty e^{-s\eta} P_\eta(\eta) d\eta &= \langle e^{-s\eta} \rangle_\eta \\ &\approx \Big(\frac{2\pi}{n}\Big)^{-\frac{n}{2}} \int_{\mathbb{R}^N} e^{-\frac{s}{n}\vec{\xi}^{\,T} A\, \vec{\xi} - \frac{n|\vec{\xi}|^2}{2}} d\vec{\xi} \\ &= \prod_{k=1}^{n} \frac{1}{\sqrt{1 + 2s\lambda_k^n}} \end{aligned} \tag{A.35}$$

where λ_k^n, $k = 1, 2, \cdots, n$ solves the matrix eigenvalue problem

$$\frac{1}{n^2} A\, \xi = \lambda_k^n \xi \tag{A.36}$$

By letting $n \to \infty$ in (A.36), we obtain the integral eigenvalue problem

$$\lambda_k f(t) = \int_0^1 \min(1-s, 1-t) f(s) ds, \quad t \in [0,1], \qquad k = 1, 2, \cdots \tag{A.37}$$

and thus as $n \to \infty$

$$\prod_{k=1}^{n} \frac{1}{\sqrt{1 + 2s\lambda_k^n}} \to \prod_{k=1}^{\infty} \frac{1}{\sqrt{1 + 2s\lambda_k}} = \prod_{k=1}^{\infty} \Big(1 + \frac{2s}{(k - \frac{1}{2})^2 \pi^2}\Big)^{-\frac{1}{2}}. \tag{A.38}$$

Therefore, formally we have established that

$$\langle e^{-s\eta} \rangle_\eta = \int_0^\infty e^{-s\eta} P_\eta(\eta) d\eta = \prod_{k=1}^{\infty} \Big(1 + \frac{2s}{(k - \frac{1}{2})^2 \pi^2}\Big)^{-\frac{1}{2}} \tag{A.39}$$

for any $s > 0$. In other words, $P_\eta(\eta)$ can be represented as an inverse Laplace transform (3.16) assuming the convergence of the integral and the fact that the infinite product is defined to be analytic on the imaginary axis. Noticing that $\prod_{k=1}^{\infty}(1 + s^2(k - \frac{1}{2})^{-2}\pi^{-2})$ is the infinite product expansion for $\cosh s$, we seek to simplify the infinite product

in (3.16) utilizing the cosh function, for the purpose of numerically evaluation of this integral. Furthermore, this fact essentially leads to Eq.(3.13) since

$$\sigma_{uc}^2(t) = \langle T^2 \rangle_{W,\eta} = \Big\langle \langle T^2 \rangle_W \Big\rangle_\eta = \int_{-\infty}^{\infty} |k|^\alpha \hat{\phi}_0^2(k) e^{-\frac{8\pi^2 k^2 t}{\mathrm{Pe}}} \Big\langle e^{-\frac{8\pi^2 k^2 t^2 \eta}{\mathrm{Pe}}} \Big\rangle_\eta dk \tag{A.40}$$

and from Eq.(A.39) we have

$$\Big\langle e^{-\frac{8\pi^2 k^2 t^2 \eta}{\mathrm{Pe}}} \Big\rangle_\eta = \Big(\cosh \frac{4\pi k t}{\sqrt{\mathrm{Pe}}} \Big)^{-\frac{1}{2}} \tag{A.41}$$

To define the product in the complex $s-$plane, we will have to choose a branch cut for each square root in the product. However, if we uniformly choose $(-\infty, 0]$ for each of these square roots, the product is then analytic everywhere in the complex plane except at $\bigcup_{k=0}^{\infty}[-(2k+\frac{3}{2})^2\pi^2/2, -(2k+\frac{1}{2})^2\pi^2/2]$. This particular choice will, as we will see, guarantee the convergence of the integral for $\eta \neq 0$, and will allow us to transform the integration path from the imaginary axis, into an infinite sum of line segments on the negative real axis, on which the infinite product in (3.16) is simply $(-\cosh\sqrt{2s})^{-1/2} = (-\cos\sqrt{-2s})^{-1/2}$. Therefore, the Bromwich integral (3.16) reduces to a series of real integrals with terms that can be evaluated by numerical quadratures.

Nonetheless, for $\eta = 0$, we cannot transform the integration path since the resulting series of real integrals diverges. Therefore we have to perform the integration along the imaginary axis. To do this, we observe that although the function $(\cosh\sqrt{2s})^{-1/2}$ is not analytic on the imaginary axis by choosing $(-\infty, 0]$ as the branch cut for both of the square roots involved, it can be made analytic, and thus equal to the infinite product evaluated on the imaginary axis, by multiplying a simple sign function

$$\mathrm{sgn}\Big(\cos\sqrt{\Big|\frac{s}{4i}\Big|} \Big) \tag{A.42}$$

In fact, this result can be generalized for $\eta \neq 0$. Therefore, by making the change of variable $s = ir$, the Bromwich integral (3.16) for $\eta = 0$ can be simplified as

$$P_\eta(\eta) = \frac{1}{\pi} \int_{-\infty}^{\infty} \frac{\mathrm{sgn}(\cos\sqrt{|r|/4}) e^{ir\eta} dr}{\sqrt{\cosh\sqrt{2ir}}} \tag{A.43}$$

with $(-\infty, 0]$ as the branch cut for all the square roots. Then this integral can be further reduced to a real integral by isolating the real and imaginary parts, which can be numerically evaluated.

The Asymptotics of $P_\eta(\eta)$

Next we discuss the behavior of $P_\eta(\eta)$ when $\eta \to 0$ and $\eta \to \infty$ utilizing (A.39) and (3.16). When $s \to +\infty$, the integral in (A.39) is a Laplace integral and the dominant contribution is

$$\int_0^\varepsilon e^{-s\eta} P_\eta(\eta) d\eta \tag{A.44}$$

with $\varepsilon \ll 1$ and it should be asymptotically approximated by

$$(\cosh\sqrt{2s})^{-1/2} \sim \sqrt{2}\exp(-\sqrt{\frac{s}{2}}) \tag{A.45}$$

for s large. However, if $P_\eta(\eta)$ has an integrable power series expansion near 0, a contradiction occurs since Watson's Lemma suggests that the leading asymptotics for $\mathbf{E}(e^{-s\eta})$ would be $s^{-\gamma}$ with $\gamma > 0$ which is a constant determined by the expansion. Therefore, $P_\eta(\eta)$ has to be vanishing *super-exponentially* near 0, namely,

$$P_\eta(\eta) \sim A\eta^B \exp(-\frac{C}{\eta^D}), \quad \eta \to 0 \tag{A.46}$$

with $C, D > 0$. Substituting the ansatz (A.46) into (A.44) and matching the constants, we find $A = \frac{1}{2\sqrt{\pi}}$, $B = -\frac{3}{2}$, $C = \frac{1}{8}$, and $D = 1$. Therefore

$$P_\eta(\eta) \sim \frac{1}{2\sqrt{\pi\eta^3}} e^{-\frac{1}{8\eta}}, \quad \eta \to 0. \tag{A.47}$$

When η is large, we notice that by choosing the branch cuts as suggested above, the Bromwich Integral (3.16) can be evaluated by transforming the integration path into an infinite sum of closed contours each of which encloses one of the intervals $\Big[-\frac{(2k+\frac{3}{2})^2\pi^2}{2}, -\frac{(2k+\frac{1}{2})^2\pi^2}{2}\Big]$, $k = 0, 1, 2, \cdots$, namely, as the distance between the contour and the interval vanishes,

$$\begin{aligned} P_\eta(\eta) &= \frac{1}{\pi i}\sum_{k=0}^{\infty} \int_{-\frac{(2k+\frac{3}{2})^2\pi^2}{2}}^{-\frac{(2k+\frac{1}{2})^2\pi^2}{2}} \prod_{j=1}^{\infty} \Big(1 + \frac{2s}{(j-\frac{1}{2})^2\pi^2}\Big)^{-\frac{1}{2}} e^{s\eta} ds \\ &= \frac{1}{\pi}\sum_{k=0}^{\infty} \int_{-\frac{(2k+\frac{3}{2})^2\pi^2}{2}}^{-\frac{(2k+\frac{1}{2})^2\pi^2}{2}} \frac{e^{s\eta} dt}{\sqrt{-\cos\sqrt{-2s}}} \\ &\sim \frac{1}{\pi}\int_{\frac{\pi^2}{8}}^{\frac{9\pi^2}{8}} \frac{e^{-t\eta} dt}{\sqrt{-\cos\sqrt{2t}}}, \qquad \eta \to +\infty \end{aligned} \tag{A.48}$$

This is again a Laplace integral and a straightforward application of the Watson's Lemma reads

$$P_\eta(\eta) \sim \frac{1}{\sqrt{2\eta}} e^{-\frac{\pi^2}{8}\eta}\Big(1+\frac{1}{2\pi^2\eta}\Big), \quad \eta \to +\infty. \tag{A.49}$$

A.5 Spatial Ergodicity of the Majda Model

Without the loss of generality, here we only consider the initial Gaussian random field (3.2) since the scalar field remains conditionally Gaussian at all time with a similar Fourier representation.

The basic idea is that the N^{th} "spatial moment" of the tracer

$$\langle T_0^N \rangle_S = \lim_{L\to\infty} \frac{1}{2L}\int_{-L}^{L} dy \int_{\mathbb{R}^N} e^{2\pi i y \sum_{j=1}^N k_j} \prod_{j=1}^N |k_j|^{\frac{\alpha}{2}} \hat{\phi}_0(k_j) dW(k_j),\ N = 1, 2, \cdots \tag{A.50}$$

is a Gaussian random variable thanks to $dW(k), k \in (-\infty, \infty)$. However, we will see in the following that for any positive integer N, a) the mean of $\langle T_0^N \rangle_S$ is exactly the N^{th} moment of the single point scalar PDF and b) the variance of this random variable is 0. Since a Gaussian distribution is uniquely determined by its mean and variance, we claim that the spatial average of the scalar converges in probability to its ensemble average at a fixed point. a) is rather obvious since

$$\begin{aligned}
\Big\langle \langle T_0^N \rangle_S \Big\rangle_W &= \lim_{L\to\infty} \frac{1}{2L}\int_{-L}^{L} dy \int_{\mathbb{R}^N} e^{2\pi i y \sum_{j=1}^N k_j} \prod_{j=1}^N |k_j|^{\frac{\alpha}{2}} \hat{\phi}_0(k_j) \Big\langle \prod_{j=1}^N dW(k_j) \Big\rangle_W \\
&= \frac{N!}{2^{N/2}(N/2)!} \lim_{L\to\infty} \frac{1}{2L}\int_{-L}^{L} dy \Big(\int_{\mathbb{R}^N} |k|^\alpha \hat{\phi}_0^2(k) dk \Big)^{N/2} \\
&= \frac{N!}{2^{N/2}(N/2)!} \Big(\int_{\mathbb{R}^N} |k|^\alpha \hat{\phi}_0^2(k) dk \Big)^{N/2} \\
&= \Big\langle T_0^N(y) \Big\rangle_W
\end{aligned} \tag{A.51}$$

if N is even and the mean vanishes if N is odd. Essentially, the cluster expansion of which the details can be found in (Majda, 1993b) eliminates the spatial dependence in the integrand and the field remains homogeneous.

Next we prove b) in the case of $N = 1$. For arbitrary N, the calculations are very similar but tedious. For $N = 1$,

$$\begin{aligned}
\left\langle \langle T_0 \rangle_S^2 \right\rangle_W &= \lim_{L\to\infty} \frac{1}{4L^2} \int_{-L}^{L}\int_{-L}^{L} dy_1 dy_2 \int_{\mathbb{R}^2} \prod_{j=1}^{2} e^{2\pi i k_j y_j} |k_j|^{\frac{\alpha}{2}} \hat{\phi}_0(k_j) \left\langle dW(k_1) dW(k_2) \right\rangle_W \\
&= \lim_{L\to\infty} \frac{1}{4L^2} \int_{-L}^{L}\int_{-L}^{L} dy_1 dy_2 \int_{-\infty}^{\infty} e^{2\pi i k(y_1-y_2)} |k|^{\alpha} \hat{\phi}_0^2(k_j) dk \qquad \text{(A.52)} \\
&= \lim_{L\to\infty} \frac{1}{4L^2} \int_{-L}^{L}\int_{-L}^{L} g(y_1-y_2) dy_1 dy_2
\end{aligned}$$

where $g(r) = \int_{-\infty}^{\infty} e^{2\pi i k r} |k|^{\alpha} \hat{\phi}_0^2(k_j) dk$ is the two-point spatial correlation function of the scalar field, which is a bounded function that goes to zero pointwise as $r \to 0$. Then after successive changes of variables $\xi = y_1 + y_2, \eta = y_1 - y_2$ and $\eta = 2Lz$,

$$\left\langle \langle T_0 \rangle_S^2 \right\rangle_W = 2 \lim_{L\to\infty} \int_0^1 (1-z) g(2Lz) dz = 0 \qquad \text{(A.53)}$$

which can be shown by classical $\varepsilon - \delta$ statements.

Bibliography

Abramowitz, M. E. D. T. and Stegun, I. A. (1965). *Handbook of Mathematical Functions, With Formulas, Graphs, and Mathematical Tables*. Dover Publications, New York.

Akhiezer, N. I. (1965). *The classical moment problem and some related questions in analysis* . Oliver & Boyd, Edinburgh.

Antonia, R. A. and Sreenivasan, K. R. (1977). Log-normality of temperature dissipation in a turbulent boundary layer. *Phys. Fluids*, 20:1800–1804.

Avellaneda, M. and Majda, A. J. (1991). An integral representation and bounds on the effective diffusivity in passive advection by laminar and turbulent flows. *Commun. Math. Phys.*, 138(2):339–391.

Balkovsky, E., Falkovich, G., and Fouxon, A. (2001). Intermittent distribution of inertial particles in turbulent flows. *Phys. Rev. Lett.*, 86(13):2790–2793.

Balkovsky, E. and Fouxon, A. (1999). Universal long-time properties of Lagrangian statistics in the Batchelor regime and their application to the passive scalar problem. *Phys. Rev. E*, 60(4):4164–4174.

Batchelor, G. K. (1959). Small-scale variation of convected quantities like temperature in turbulent fluid Part 1. General discussion and the case of small conductivity. *J. Fluid Mech.*, 5(01):113–133.

Batchelor, G. K. (2002). *An Introduction to Fluid Dynamics*. Cambridge University Press, London.

Bender, C. M. and Orszag, S. A. (1999). *Advanced mathematical methods for scientists and engineers. 1, Asymptotic methods and perturbation theory*. Springer, New York.

Bonn, J. and McLaughlin, R. M. (2001). Sensitive enhanced diffusivities for flows with fluctuating mean winds: a two-parameter study. *J. Fluid Mech.*, 445:345–375.

Bourlioux, A. and Majda, A. (2002). Elementary models with probability distribution function intermittency for passive scalars with a mean gradient Phys. *Phys. Fluids*, 14(2):881–897.

Bronski, J. C. (2003). Asymptotics of Karhunen-Loeve eigenvalues and tight constants for probability distributions of passive scalar transport. *Commun. Math. Phys.*, 238(3):563–582.

Bronski, J. C., Camassa, R., Lin, Z., McLaughlin, R. M., and Scotti, A. (2007). An explicit family of probability measures for passive scalar diffusion in a random flow. *J. Stat. Phys.*, Accepted.

Bronski, J. C. and McLaughlin, R. M. White noise averaging and the time ordered calculus. *Unpublished*.

Bronski, J. C. and McLaughlin, R. M. (1997). Passive scalar intermittency and the ground state of Schrödinger operators. *Phys. Fluids*, 9:181–190.

Bronski, J. C. and McLaughlin, R. M. (2000a). Rigorous estimates of the tails of the probability distribution function for the random linear shear model. *J. Stat. Phys.*, 98(3):897–915.

Bronski, J. C. and McLaughlin, R. M. (2000b). The problem of moments and the Majda model for scalar intermittency. *Phys. Lett. A*, 265:257–263.

Camassa, R., Chung, B. J., Lee, L., Lin, Z., McLaughlin, R. M., and Salman, H. (2007). Geophysical shallow water simulations for a random passive tracer. In Preparation.

Camassa, R. and Levermore, C. D. (1997). Layer-mean quantities, local conservation laws, and vorticity. *Phys. Rev. Lett.*, 78(4):650–653.

Camassa, R., Lin, Z., and McLaughlin, R. M. (2006). Evolution of the probability measure for the Majda model: new invariant measures and breathing PDFs. *J. Stat. Phys.*, Submitted.

Camassa, R., Martinsen-Burrell, N., and McLaughlin, R. M. (2005). An algorithm for simulating stationary gaussian random fields. *Phys. Fluids*, Submitted.

Castaing, B., Gunaratne, G., Heslot, F., Kadanoff, L., Libchaber, A., Thomae, S., Wu, X. Z., Zaleski, S., and Zanetti, G. (1989). Scaling of hard thermal turbulence in Rayleigh-Bénard convection. *J. Fluid Mech.*, 204:1–30.

Chan, G. (1997). An algorithm for simulating stationary gaussian random fields. *Numer. Math.*, 7:355–361.

Chertkov, M., Falkovich, G., and Kolokolov, I. (1998). Intermittent dissipation of a passive scalar in turbulence. *Phys. Rev. Lett.*, 80(10):2121–2124.

Chertkov, M., Falkovich, G., Kolokolov, I., and Lebedev, V. (1995). Statistics of a passive scalar advected by a large-scale two-dimensional velocity field: Analytic solution. *Phys. Rev. E*, 51(6):5609–5627.

Chertkov, M., Kolokolov, I., and Vergassola, M. (1997). Inverse cascade and intermittency of passive scalar in one-dimensional smooth flow. *Phys. Rev. E*, 56(5):5483–5499.

Ching, E. S. C. (1991). Probabilities for temperature differences in Rayleigh-Bénard convection. *Phys. Rev. A*, 44(6):3622–3629.

Corless, R. M., Jeffrey, D. J., and Knuth, D. E. (1997). A sequence of series for the Lambert W function. *Proceedings of the 1997 international symposium on Symbolic and algebraic computation*, pages 197–204.

E, W., Khanin, K., Mazel, A., and Sinai, Y. (1997). Probability distribution functions for the randomly forced Burgers equation. *Physical review letters*, 78(10):1904–1907.

Elliott Jr., F. W., Horntrop, D. J., and Majda, A. J. (1997). Monte Carlo methods for turbulent tracers with long range and fractal random velocity fields. *Chaos*, 7(1):39–48.

Ermak, D. L. and McCammon, J. A. (1978). Brownian dynamics with hydrodynamic interactions. *J. Chem. Phys.*, 69:1352.

Falkovich, G. and Sreenivasan, K. R. (2006). Lessons from Hydrodynamic Turbulence. *Phys. Today*, 59(4):43.

Ferrari, R. and Rudnick, D. L. (2000). Thermohaline variability in the upper ocean. *J. Geophys. Res.*, 105(C7):16857–16884.

Frisch, U., Mazzino, A., and Vergassola, M. (1998). Intermittency in Passive Scalar Advection. *Phys. Rev. Lett.*, 80(25):5532–5535.

Gardiner, C. W. (1985). *Handbook of Stochastic Methods*. Springer, New York.

Gollub, J. P., Clarke, J., Gharib, M., Lane, B., and Mesquita, O. N. (1991). Fluctuations and transport in a stirred fluid with a mean gradient. *Phys. Rev. Lett.*, 67(25):3507–3510.

Grabowski, W. W. (2004). An improved framework for superparameterization. *J. Atmos. Sci.*, 61(15):1940–1952.

Gradshteyn, I. S. and Ryzhik, I. M. (1980). *Table of integrals, series, and products*. Academic Press, New York.

Gythiel, A. and Lemons, D. S. (2002). *An Introduction to Stochastic Processes in Physics*. Johns Hopkins University Press, Baltimore.

Holzer, M. and Siggia, E. D. (1994). Turbulent mixing of a passive scalar. *Phys. Fluids*, 6:1820–1837.

Hu, Y. and Pierrehumbert, R. T. (2001). The advection–diffusion problem for stratospheric flow. Part I: Concentration probability distribution function. *J. Atmos. Sci.*, 58(12):1493–1510.

Hu, Y. and Pierrehumbert, R. T. (2002). The advection–diffusion problem for stratospheric Flow. Part II: Probability distribution function of tracer gradients. *J. Atmos. Sci.*, 59(19):2830–2845.

Inverardi, P. N., Petri, A., Pontuale, G., and Tagliani, A. (2005). Stieltjes moment problem via fractional moments. *Appl. Math. Comp.*, 166(3):664–677.

John, F. (1971). *Partial differential equations*. Springer-Verlag, New York.

Jones, D. A., Poje, A. C., and Margolin, L. G. (1997). Resolution Effects and Enslaved Finite-Difference Schemes for a Double Gyre, Shallow-Water Model. *Theor. Comp. Fluid Dyn.*, 9(3):269–280.

Jung, S. and Swinney, H. (2005). Velocity difference statistics in turbulence. *Phys. Rev. E*, 72(2):26304.

Kac, M. (1949). On Distributions of Certain Wiener Functionals. *T. Am. Math. Soc.*, 65(1):1–13.

Kalman, R. E. (1960). A new approach to linear filtering and prediction problems. *J. Basic Eng.*, 82(1):35–45.

Keener, J. P. (2000). *Principles of Applied Mathematics: Transformation and Approximation (Advanced Book Program)*. Westview Press.

Keller, J. B. and McLaughlin, D. W. (1975). The Feynman integral. *The American Mathematical Monthly*, 82(5):451–465.

Kolmogorov, A. N. (1941). Local structure of turbulence in an incompressible fluid at very high Reynolds numbers. *Dokl. Akad. Nauk SSSR*, 30(4):299–303.

Kraichnan, R. (1968). Small-scale structure of a scalar field convected by turbulence. *Phys. Fluids*, 11:945–953.

Kraichnan, R. H. (1994). Anomalous scaling of a randomly advected passive scalar. *Phys. Rev. Lett.*, 72(7):1016–1019.

Kramer, P. R., Majda, A. J., and Vanden-Eijnden, E. (2003). Closure Approximations for Passive Scalar Turbulence: A Comparative Study on an Exactly Solvable Model with Complex Features. *J. Stat. Phys.*, 111(3):565–679.

Kuo, A. C. and Polvani, L. M. (1997). Time-dependent fully nonlinear geostrophic adjustment. *J. Phys. Oceanogr.*, 27(8):1614–1634.

Latini, M. and Bernoff, A. J. (2001). Transient anomalous diffusion in Poiseuille flow. *J. Fluid Mech.*, 441:399–411.

Leveque, R. J. (2002). *Finite Volume Methods for Hyperbolic Problems*. Cambridge University Press, Cambridge.

Lukić, B., Jeney, S., Tischer, C., Kulik, A. J., Forró, L., and Florin, E. L. (2005). Direct Observation of Nondiffusive Motion of a Brownian Particle. *Phys. Rev. Lett.*, 95(16):160601.

Majda, A. J. (1993a). Explicit inertial range renormalization theory in a model for turbulent diffusion. *J. Stat. Phys.*, 73(3):515–542.

Majda, A. J. (1993b). The random uniform shear layer: an explicit example of turbulent diffusion with broad tail probability distributions. *Phy. Fluids A*, 5:1963–1970.

Majda, A. J. (2003). *Introduction to PDEs and Waves for the Atmosphere and Ocean*. American Mathematical Society / CIMS, New York.

Majda, A. J. and Kramer, P. R. (1999). Simplified models for turbulent diffusion: Theory, numerical modelling, and physical phenomena-fractal interfaces, non-Gaussian statistics and the sweeping effect. *Physics Reports*, 314(4):237–574.

Mason, J. C. and Handscomb, D. C. (2003). *Chebyshev Polynomials*. CRC Press, Boca Raton.

Mason, T. G. and Weitz, D. A. (1995). Optical measurements of frequency-dependent linear viscoelastic moduli of complex fluids. *Phys. Rev. Lett.*, 74(7):1250–1253.

McLaughlin, R. M. (1994). *Turbulent transport. Ph.D. Thesis, Program in Applied Computational Mathematics*. Princeton University Press.

McLaughlin, R. M. and Majda, A. J. (1996). An explicit example with non-Gaussian probability distribution for nontrivial scalar mean and fluctuation. *Phys. Fluids*, 8(2):536–547.

Miller, A. J., Cayan, D. R., Barnett, T. P., Graham, N. E., and Oberhuber, J. M. (1994). Interdecadal variability of the pacific ocean: model response to observed heat flux and wind stress anomalies. *Clim. Dynam.*, 9(6):287–302.

Monin, A. S. and Yaglom, A. M. (1971). *Statistical fluid mechanics*. MIT Press, Cambridge.

Niemela, J. J., Skrbek, L., Sreenivasan, K. R., and Donnelly, R. J. (2000). Turbulent convection at very high Rayleigh numbers. *Nature*, 404(6780):837–840.

Pedlosky, J. (1998). *Geophysical Fluid Dynamics*. Springer, New York.

Pierrehumbert, R. T. (2000). Lattice models of advection-diffusion. *Chaos*, 10(1):61.

Plasting, S. C. and Young, W. R. (2006). A bound on scalar variance for the advection–diffusion equation. *J. Fluid Mech.*, 552:289–298.

Poje, A. C., Jones, D. A., and Margolin, L. G. (1996). Enslaved finite difference approximations for quasigeostrophic shallow flows. *Physica D*, 98(2):559–573.

Pumir, A., Shraiman, B. I., and Siggia, E. D. (1991). Exponential tails and random advection. *Phys. Rev. Lett.*, 66(23):2984–2987.

Reynolds, O. (1883). An experimental investigation of the circumstances which determine whether the motion of water shall be direct or sinuous, and of the law of resistance in parallel channels. *Philos. T. Roy. Soc. London A*, 174:935–982.

Rudin, W. (1987). *Real and complex analysis*. McGraw-Hill, New York.

She, Z. S. and Orszag, S. A. (1991). Physical model of intermittency in turbulence: Near-dissipation-range non-Gaussian statistics. *Phys. Rev. Lett.*, 66(13):1701–1704.

Shepherd, T. G., Koshyk, J. N., and Ngan, K. (2000). On the nature of large-scale mixing in the stratosphere and mesosphere. *J. Geophys. Res.*, 105(D10):12433–12446.

Shohat, J. A. and Tamarkin, J. D. (1943). The Problem of Moments. *American Mathematical Society Mathematical Surveys*, 2.

Shraiman, B. I. and Siggia, E. D. (1994). Lagrangian path integrals and fluctuations in random flow. *Phys. Rev. E*, 49(4):2912–2927.

Sinai, Y. G. and Yakhot, V. (1989). Limiting probability distributions of a passive scalar in a random velocity field. *Phys. Rev. Lett.*, 63(18):1962–1964.

Son, D. T. (1999). Turbulent decay of a passive scalar in the Batchelor limit: Exact results from a quantum-mechanical approach. *Phys. Rev. E*, 59(4):3811–3814.

Sparling, L. C. (2000). Statistical perspectives on stratospheric transport. *Rev. Geophys.*, 38(3):417–436.

Sreenivasan, K. R. and Antonia, R. A. (1997). The phenomenology of small-scale turbulence. *Annu. Rev. Fluid Mech.*, 29(1):435–472.

Sreenivasan, K. R., Antonia, R. A., and Britz, D. (2006). Local isotropy and large structures in a heated turbulent jet. *J. Fluid Mech.*, 94(04):745–775.

Sreenivasan, K. R., Danh, H. Q., and Antonia, R. A. (1977). Temperature dissipation fluctuations in a turbulent boundary layer. *Phys. Fluids*, 20:S288.

Sukhatme, J. (2004). Probability density functions of decaying passive scalars in periodic domains: An application of Sinai-Yakhot theory. *Phys. Rev. E*, 69(5):56302.

Thiffeault, J. L., Doering, C. R., and Gibbon, J. D. (2004). A bound on mixing efficiency for the advection–diffusion equation. *J. Fluid Mech.*, 521:105–114.

Thoroddsen, S. T. and van Atta, C. W. (2006). Exponential tails and skewness of density-gradient probability density functions in stably stratified turbulence. *J. Fluid Mech.*, 244:547–566.

Vanden-Eijnden, E. (2001). Non-Gaussian invariant measures for the Majda model of decaying turbulent transport. *Commun. Pure Appl. Math*, 54(9):1146–1167.

Warhaft, Z. (2000). Passive scalars in turbulent flows. *Annu. Rev. Fluid Mech.*, 32(1):203–240.